# Interactions between waves and new generations of brakewaters with small footprint

Paul Milesi

CENTRALE MARSEILLE

École Doctorale : Sciences pour l'Ingénieur : Mécanique, Physique, Micro et Nanoélectronique (ED353)

Laboratoire : IRPHE

**THÈSE DE DOCTORAT**

pour obtenir le grade de

DOCTEUR de l'ÉCOLE CENTRALE de MARSEILLE

Discipline : Mécanique des fluides

# INTERACTIONS BETWEEN WAVES AND NEW GENERATIONS OF BREAKWATERS WITH SMALL FOOTPRINT

# INTERACTION ENTRE LA HOULE ET LES NOUVELLES GENERATIONS D'OUVRAGES CÔTIERS DE FAIBLE EMPRISE AU SOL

par

**MILESI Paul**

**Directeur de thèse :** KIMMOUN Olivier

*Soutenue le 18 juillet 2019*

*devant le jury composé de :*

| | | |
|---|---|---|
| RIVOALEN Elie | Prof. - INSA Rouen | Rapporteur |
| REY Vincent | Prof. - Université du Sud Toulon | Rapporteur |
| GREAVES Deborah | Prof. - Université de Plymouth | Examinatrice |
| ABADIE Stéphane | Prof. - Université de Pau | Examinateur |
| BENOIT Michel | Prof. - Ecole Centrale Marseille & IRPHE | Examinateur |
| HAMM Luc | HdR - Artelia | Examinateur |
| KIMMOUN Olivier | HdR - Ecole Centrale Marseille & IRPHE | Directeur de thèse |
| LAJOIE David | Expert en hydrodynamique - Le Tignet | Coencadrant |

# ABSTRACT

Nowadays the respect of the environment is an obligation in maritime works. Vertical concrete caissons with porous plates are often the number one technical solution to enlarge existing ports and/or to improve the agitation of the basins. The footprint is reduced and the demand in quarry materials is less important compared to classical riprap breakwaters. Recently, alternative systems to vertical concrete caissons have been designed. Vertical riprap breakwaters are made of a metal framework enclosing blocks. This kind of structure offers environmental benefits, permeability for currents and a good hydrodynamic performance. This thesis work looks at developing a new 3D-BEM code that is easy to use and integrates porous media. Innovative geometries are tested like spaced gabions with damping chamber or a mix of porous plates and porous media.

Describing flows in porous media is an complex issue. Volume averaging method is the common mathematical process used to model porous media flows without drawing every grain of a porous medium. The well-known extended Forchheimer equation describes the volumetric forces applied to the flow by a porous medium through resistance and inertial coefficients. These researches were the occasion to look into this coefficients, especially the one of poorly understood inertia in the case of a porous medium. It plays a major role in very low-KC flows currently occurring in porous breakwaters apart from armour layer.

First, a literature review on porous media flows was undertaken. In parallel, the numerical code called *Diffra3D* was produced. It was then used to look for resistance coefficients of porous media through data coming from three experimental campaigns : one sloshing test on hexapode and two classical reflection-transmission studies in a wave tank. These campaigns were also the occasion to test and calibrate the code. New geometries of porous structures were then tested experimentally and numerically.

Two new values of resistance coefficients of a porous medium are proposed. Some interesting features concerning the inertia coefficient $C_M$ of a porous medium are also developed. In simulations, we observe that the hydrodynamic behaviour of porous structures in low-KC flows is very sensitive to the coefficient of inertia. This research topic would still deserve further studies in order to find empirical law(s) for the inertia coefficient of a porous medium. The code *Diffra3D* performs well to model porous media flows. However, it is limited to waves with low steepness. The challenge is to properly characterise the porous medium. This research has shown that innovative porous structures like spaced gabions have proven their place as environmentally-friendly damping breakwaters. They may be commonly used in the future.

# ABSTRACT

De nos jours, le respect de l'environnement est une obligation dans le cadre de travaux maritimes. Les caissons en béton verticaux à plaques poreuses sont souvent la solution technique privilégiée pour agrandir les ports existants et / ou améliorer l'agitation des bassins. L'empreinte au sol est réduite et la demande en matériaux de carrière est moins importante par rapport aux digues en enrochement classiques. Récemment, des systèmes alternatifs aux caissons en béton verticaux ont été conçus. Les structures amortisseuses de la houle à enrochements verticalisés sont constituées d'une structure métallique entourant des blocs. Ce type de structure offre des avantages environnementaux, une perméabilité aux courants et une bonne performance hydrodynamique. Ce travail de thèse visait à développer un nouveau code 3D-BEM facile à utiliser et intégrant les écoulements en milieux poreux. Des géométries innovantes sont testées comme des gabions espacés avec une chambre d'expansion ou un mélange de plaques poreuses et de milieux poreux.

La description des écoulements dans un milieu poreux est une question complexe. Navier-Stokes moyenné au sens de Reynolds (RANS) est le processus mathématique communément utilisé pour modéliser les écoulements en milieux poreux. Ce dernier est considéré comme un milieu continu homogène. L'équation bien connue de Forchheimer étendue décrit les forces volumiques appliquées à l'écoulement par un milieu poreux à travers des coefficients de résistance et d'inertie. Ces recherches ont été l'occasion d'examiner ces coefficients, notamment celui d'inertie mal connu dans le cas d'un milieu poreux. Il joue un rôle majeur pour les écoulements à très faible KC se produisant dans les couches internes des digues poreuses.

Une analyse de la littérature sur les écoulements de milieux poreux a été entreprise. Le code numérique appelé *Diffra3D* a été développé. Il a ensuite été utilisé pour rechercher des coefficients de résistance de milieux poreux à l'aide de données provenant de trois campagnes expérimentales : un test de sloshing sur hexapode et deux études classiques de transmission/réflexion en canal à houle. Celles-ci ont également été l'occasion de tester et de calibrer le code. De nouvelles géométries de structures poreuses ont ensuite été testées expérimentalement et numériquement.

Deux nouvelles valeurs de coefficients de résistance d'un milieu poreux sont proposées pour les écoulements à très faibles KC. Certaines caractéristiques intéressantes concernant le coefficient d'inertie $C_M$ d'un milieu poreux sont également développées. Ce sujet de recherche mériterait encore d'être approfondi pour tenter de trouver une ou plusieurs loi(s) empirique(s) décrivant l'évolution du coefficient d'inertie dans ce régime spécifique d'écoulement. Le code *Diffra3D* fonctionne de façon satisfaisante pour modéliser les écoulements en milieu poreux. Il est cependant limité aux vagues à faibles cambrures. Tout l'enjeu est de bien caractériser le milieu poreux étudié. L'utilisation de *Diffra3D* a permis de montrer que les structures poreuses verticales innovantes, telles que les gabions espacés, ont entièrement leur place en tant que digues amortisseuses de la houle respectueuses de l'environnement. Elles pourraient être couramment utilisées dans le futur.

# DEDICATION

I would like to dedicate this work to my grandparents Jeanne and René Ottari.

# DECLARATION

I declare that the thesis here submitted is original except for the source materials explicitly acknowledged.

# ACKNOWLEDGEMENTS

First of all I want to thank my mentor and my boss Dr. David Lajoie for trusting me 5 years ago when he chose to take me to a graduation internship in his compagny **HydroGC SAS**. After two years of collaboration, he trusted me again offering me the possibility to begin a thesis work in the framework of a **CIFRE** scholarship. David has supervised me all along the path of my researches. He guided me and he has always been available to explain to me the physics in coastal hydrodynamic phenomena and deeply think about problems I had. He certainly is an excellent pragmatic scientist, who is a good engineer, always looking for applying new theoretical law to concrete and complex situations. He taught me most of what I know on coastal engineering. I owe him a lot.

I also want to deeply thank my thesis supervisor Dr. Olivier Kimmoun from the engineering school **Centrale Marseille** and from the laboratory **IRPHE** for having accepted this thesis project and having made it possible. I am grateful for the time he past supervising me from start to end. I also want to warmly thank the other members of the hydrodynamic department of Centrale Marseille ; Dr. Fabien Remy, Dr. Guillaume Dupont, Dr. Bernard Molin and my PhD student friends for having always been disposed to help me further during my experimental researches.

I also want to thank the other co-workers of the engineering office I worked for ; Sandra Gronchi, Nelly Gilbert, Christelle Homar, Francis Biancheri, Gérard Pont, Pierre Louis and Jean-François Deste. Thank you to all of you for your presence and your watchful eye. Everything Jean-François touches with his hands turns to gold. He helped me a lot by designing and manufacturing small-scale model of prototypes I tested during the four experimental campaigns.

Finally, I also want to thank my friends and my love Léopoldine Lebouchard for having been present to my side all along these few years, supporting me in ups and downs and having always made me look further in the future. I also owe you a lot.

# Contents

# List of Figures

# List of Tables

# List of Symbols

The next list describes several symbols that will be later used within the body of the document :

**Mathematical operators**

| | |
|---|---|
| $\Delta$ | Laplacien |
| $\overrightarrow{\nabla}$ | Gradient |
| $\overrightarrow{rot}$ | Rotational |
| $\Re$ | Real part of |

**Non-dimensional numbers**

| | |
|---|---|
| $\beta_S$ | Stocks number |
| $A_c$ | Acceleration number |
| $F_o$ | Forchheimer number |
| $F_r$ | Froude number |
| $KC$ | Keulegan-Carpenter number |
| $R_e$ | Reynolds number |
| $U_r$ | Ursell number |

**Other Symbols**

| | | |
|---|---|---|
| $\alpha, \beta$ | Tortuosity coefficients, Coefficient for local condition on distant waves | |
| $\beta$ | Angle of incidence of the swell | $rad$ |
| $\chi$ | Source $\chi = \Phi$ | $m^2.s^{-1}$ |
| $\delta$ | Relation between maximal and average elliptic velocities | |
| $\epsilon$ | Small parameter, Shorter notation of $\epsilon = S + if$, Error value | |
| $\eta$ | Free surface | $m$ |
| $\gamma_p$ | Empirical coefficient | |
| $\hat{v_d}$ | Maximal filter velocity | $m.s^{-1}$ |
| $\hat{v_p}$ | Maximal pore velocity | $m.s^{-1}$ |
| $\lambda$ | Wavelength, Scale-factor | $m$ |
| $\mu$ | Surface porosity | |
| $\nu$ | Kinematic viscosity | $m^2.s^{-1}$ |
| $\omega$ | Pulsation | $rad.s^{-1}$ |
| $\Omega_m^{(n)}$ | Fourier transformation of $e_m$ at frequency $n\omega$ | |
| $\Phi$ | Real potential | $m^2.s^{-1}$ |
| $\phi$ | Complex potential | $m^2.s^{-1}$ |
| $\Psi$ | Scalar stream function | |
| $\rho$ | Density of the fluid | $kg.m^{-3}$ |

| | | |
|---|---|---|
| $\Sigma$ | Closed domain $\Sigma = F + P$, Structure boundary | |
| $\sigma$ | Source $\sigma = -\frac{\partial \Phi}{\partial n}$ | $m.s^{-1}$ |
| $\tau$ | Wall's porosity | |
| $\vec{f}_r$ | Volumetric forces | $N.m^{-3}$ |
| $\vec{n}$ | Normal vector | $m$ |
| $A$, $a$ | Amplitude | $m$ |
| $a$, $b$, $c$ | Resistance and inertial coefficients of the extended Forchheimer equation, | $s.m^{-1}$, $s^2.m^{-2}$, $s^2.m^{-1}$ |
| $a_l$ | Characteristic width of a porous wall | $m$ |
| $B$ | Subscript for bounds waves, Damping chamber width, Porous structure width | |
| $b$ | Dimension of the porous structure | $m$ |
| $C$ | Control boundary (inlet or outlet) | |
| $c$ | Subscript for computed value | |
| $C'_a$ | Added mass coefficient | |
| $C'_b$ | Damping coefficient | |
| $C_a$ | Added mass coefficient | |
| $C_f$ | Resistance coefficient | |
| $c_g$ | Group velocity | $m.s^{-1}$ |
| $C_M$ | Inertia coefficient $C_M = 1 + C_a$ | |
| $c_p$, $C_{PE}$ | Phase velocity | $m.s^{-1}$ |
| $d$ | Diameter, Subscript for filter physical value | $m$, - |
| $D_{ij}$ | Influence coefficient of normal dipole of panel i in relation to panel j | |
| $d_{n50}$ | Nominal medium diameter | $m$ |
| $e_0$ | Void ratio | |
| $E_c$ | Kinematic energy per unit surface | $kg.s^{-2}$ |
| $E_d$ | Dissipated energy | |
| $e_m$ | Noise | |
| $E_p$ | Potential energy per unit surface | $kg.s^{-2}$ |
| $F$ | Subscript for free waves | |
| $f$ | Dissipation coefficient (Sollit and Cross) | |
| $FS$ | Free surface boundary | |
| $G$ | Ground boundary | |
| $G_M$ | Green function | $m^{-1}$ |
| $H$ | Peak-to-trough height | $m$ |
| $h$ | Water depth | $m$ |
| $h_c$, $H_{caisson}$ | Water depth inside the damping chamber | $m$ |
| $H_s$ | Significant wave height | $m$ |
| $I$ | Subscript for incident waves, Interface boundary | |
| $i$ | Imaginary number ($i^2 = -1$), Subscript for panel i, Subscript for incident waves | |
| $j$ | Subscript for panel j | |
| $K$ | Intrinsic permeability | $m^2$ |
| $k$ | Wave number | |

| | | |
|---|---|---|
| $K(m), E(m)$ | Elliptic integrals of first and second kinds, respectively | |
| $k_c$ | Coefficient of flow restriction | |
| $k_o$ | Kozeny constant | |
| $K_p, K'_p$ | Coefficients of pressure loss | |
| $l_c$ | Length of the wave channel upstream and downstream the structure | $m$ |
| $ll$ | Mesh size | $m$ |
| $m$ | Subscript for measured value | |
| $M_i$ | Center of gravity of panel i | |
| $M_{50}$ | Medium mass | $kg$ |
| $n$ | Porosity | |
| $n_{RRd}, n_{RRM}$ | Coefficients of uniformity function of diameters, of masses | |
| $p$ | Pressure | $N.m^{-2}$ |
| $p$, $q$, $r$ | Normal vector components | $m$ |
| $R$ | Subscript for reflected waves, Subscript for radiation, Reflected coefficient, Subscript for relative coordinate system, Radius of the control cylinder ($m$) | |
| $r$ | Subscript for resistance, Subscript for real-scale model | |
| $RAO$ | Response amplitude operator | |
| $S$ | Inertia coefficient of momentum equation $S = 1 + C_M \frac{1-n}{n}$ (Sollit and Cross) | |
| $s$ | Subscript for scale-model | |
| $S_c$ | Specific surface area | $m^2.m^{-3} = m^{-1}$ |
| $S_{ij}$ | Influence coefficient of source dipole of panel i in relation to panel j | $m$ |
| $T$ | Period | $s$ |
| $T$ | Transmitted coefficient | |
| $T_p$ | Peak period | $s$ |
| $u$, $v$, $w$ | Fluid velocity components | $m.s^{-1}$ |
| $U_c$ | Eulerian stream velocity | $m.s^{-1}$ |
| $v_d, V_d$ | Darcy or filter velocity | $m.s^{-1}$ |
| $v_E$ | Velocity of the hexapod | $m.s^{-1}$ |
| $V_F$ | Volume of the fluid domain $F$ | $m^3$ |
| $V_P$ | Volume of the rock domain $P$ | $m^3$ |
| $v_p$ | Pore velocity | $m.s^{-1}$ |
| $V_\Sigma$ | Volume of the closed domain $\Sigma = F + P$ | $m^3$ |
| $v_{dE}$ | Filter velocity of the hexapod $v_{dE} = n v_E$ | $m.s^{-1}$ |
| $v_{dn}$ | Normal filter velocity | $m.s^{-1}$ |
| $v_{dR}$ | Filter relative velocity $v_{dR} = n v_{pR}$ | $m.s^{-1}$ |
| $v_{pR}$ | Relative pore velocity | $m.s^{-1}$ |
| $X$ | Displacement of the hexapod | $m$ |

**Physics Constants**

| | | |
|---|---|---|
| $g$ | Gravitational constant | $m.s^{-2}$ |

# INTRODUCTION

Design studies for new maritime structures in the french coastal zone are generally carried out within the framework of existing port developments. Surface extension of basins in terms of parking space and reduction of the agitation form the major axis of economical development for harbour and marina. This often justifies the need for new infrastructures. For instance, the redevelopment of the port of Banyuls-sur-Mer on the south french coast was the occasion to significantly improve the quality of the harbour basin with, amongst others, the lengthening of the principal seawall. Large commercial ports also continue to invest in new maritime infrastructures to adapt to new markets. Recently, the Grand Port Maritime of Marseille reconfigured all its north pass to accommodate the new giant cruise ships.

The renovation and the extension of breakwaters has involved for a long time the duty of respect of the environment. The classical wide breakwaters built in the beginning of the 20th century to delimit the basins in deep water have progressively been replaced by vertical concrete caisson which are more economical and less demanding in quarry materials. The footprint on the seabed is drastically reduced. Swell damping through porous plate of *Jarlan chamber* type were rapidly incorporated into vertical caissons, offering many advantages : low reflection of the swell energy around navigation zones and into harbour basins, low hydrodynamic impact on marine life and reduction of over-topping efforts. The port of Marseille chose this technical solution to modify its north pass. The ports of Cannes and Cap d'Ail recently built vertical damping caissons into their basins. They are easily incorporated below quays or existing pontoons.

Alternative systems to vertical concrete caissons have been recently designed : vertical riprap structures. This kind of structure is innovative and offers many advantages beside being often cost attractive compared to concrete caissons. The blocks are enclosed by a metal framework or bored piles occupying a reduced ground footprint. A little groyne was designed following this method in order to protect the port of La Ciotat in the middle of the protected sea grass. The concept was approved by the french environmental authorities, then built. We observe now a reduction of the agitation conform to the numerical studies conducted beforehand. This is a kind of prototype reconciling the needs for heavy breakwaters and environmental obligations in terms of sea grass protection. As Mediterranean ports are surrounded by protected areas, the concept of environmentally-friendly vertical structures deserves further study, which is the aim of the presented work.

## Environmental benefits

Vertical structures allow engineers to implant breakwater near areas of marine life without significant impact while offering a better damping protection to swell. In Banyuls-sur-Mer, the construction of a 20m large vertical riprap head breakwater is a solution to stop the significant agitation problems met with south-east storm swells. The metallic framework of the structure keep the blocks at least 5m away from the protected aquatic plant habitat (see figure 1). The main dyke could then be extended to the maximum allowed.

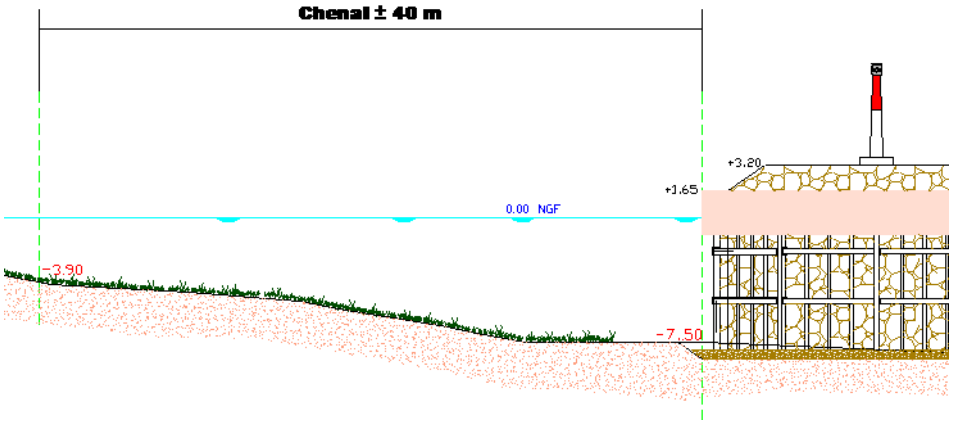


Figure 1: Vertical riprap head breakwater in the future port of Banyuls-sur-Mer

The use of coarse granular material to fill the structure's framework generate lower construction impact by preventing a too high turbidity.

The porous structure of such breakwaters makes up for the occupied sea bed by offering new environments favourable to young fishes. Porous media and concrete caissons can also be mixed in order to create this kind of environment. The future counter jetty and the two damping caissons of the port of Banyuls-sur-mer (see figure 2) is an example where vertical gabions are installed at the back of a damping chamber. In this case, gabions also act as ballast and bring some sea damping.

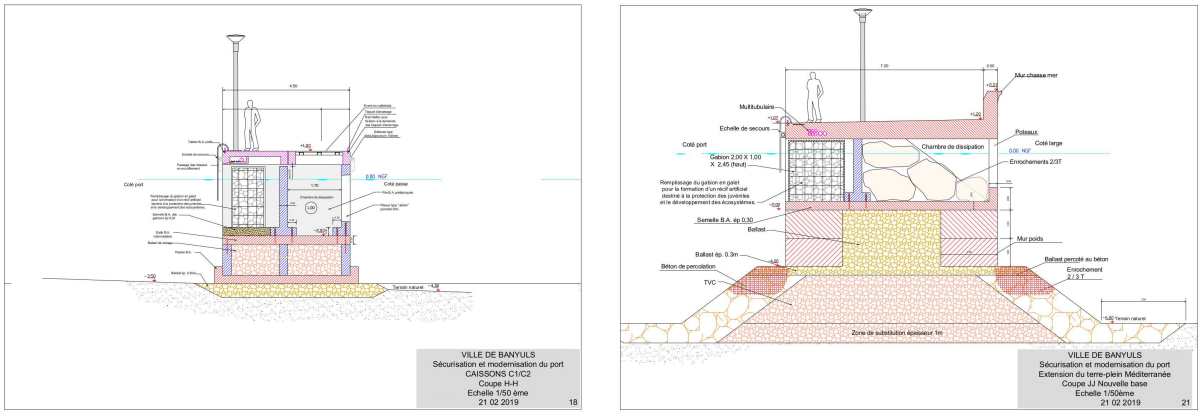


Figure 2: Vertical gabions incorporated inside a concrete caisson.
From left to right : a damping caisson installed inside the harbour and the future counter jetty of the port of Banyuls-sur-Mer

## Permeability for currents

Maintaining a good quality of water is a relevant issue for ports to avoid toxic bacteria to proliferate in their basins with the consequence of bad odours bothering clients. That is why the design of a harbour basin has to take into account the natural and artificial current flow. Vertical riprap breakwaters have the advantage to be porous structures. They offer a positive permeability which enables a better current flow than concrete caissons. The extension project of *Heures Claires* harbour in Istres was the occasion to integrate a damping vertical porous structure (Fig. 3) all along a new pontoon in order to reduce lapping. This choice of structure instead of concrete caisson was guided by the quality of water necessity and the construction cost.

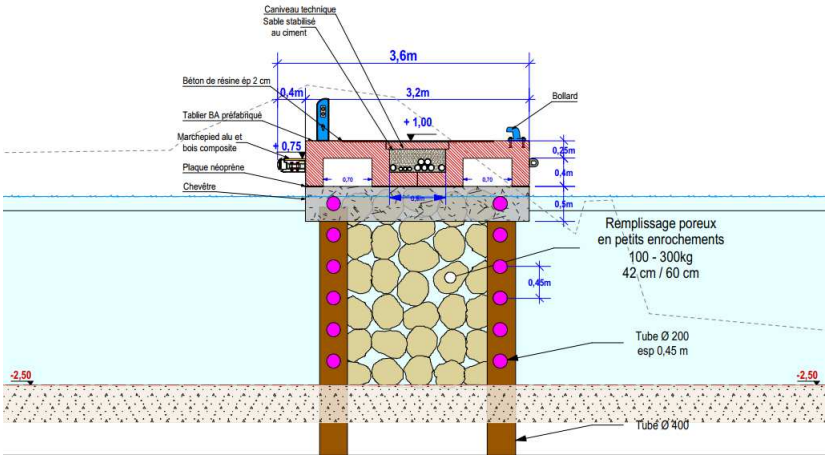


Figure 3: Damping riprap pontoon on bored piles in the future port of Istres

## An easier navigation

Vertical breakwaters are in the interest of sailors because they mark a clear waterways delimitation. The groyne installed in La Ciotat and in Banyuls-sur-Mer make the port entry easier, especially when wind and swell are unfavourable.

Figure 4: Vertical riprap breakwater in the entry of the port of La Ciotat.
Left : Installation of the riprap. Middle : the breakwater finished. Right : The bored piles holding the rocks

## Hydrodynamic performance

The hydrodynamic performance of damping breakwaters is a important studied field in order to best protect harbours and coastal zones. While a classical wide breakwater reflects about 50% of incident wave height, the design of a *Jarlan* type caisson, with a porous plate and an adapted chamber size, can dissipate until 70% to 80% of the incident wave height.

Vertical riprap breakwaters are innovative damping structures. Until now, only quite simple geometries have been the subject of academic research. Today, most of the last numerical developments to understand the hydrodynamic comportment of porous breakwaters are based on two different technologies :

- the Volume Of Fluid (VOF) method which solves the eulerian Navier-Stockes equations;
- the Smoothed Particle Hydrodynamics (SPH) technique which resolve the lagrangian Navier-Stockes equations.

These two models are very advanced because they take into account a lot of non-linear phenomena and best describe the flow. The first 3D two-phase flows VOF models were developed in 2014 by Higuera (2014) & al. [23] and B. Jensen & al. (2014) [25]. The other side of the coin is their complexity and their high computational requirement for real cases especially in the context of studies in engineering offices where the computational resources and time are limited. For example, engineering offices can consider using a 1D propagation wave channel with a VOF method but even in that case, they are rapidly limited in the number and duration of simulations and cases that can be run.

On the other hand, little effort has been made to develop more flexible and user-friendly numerical tools such as those based on integral methods used to solve potential flow problems. This numerical method can be easily associated with porous media flows through averaging techniques. The development of a 3D numerical tool *Diffra3D* headed to coastal engineering office was one of the two main issues of this thesis work. The second issue was to investigate dissipation coefficients of a porous medium to better understand the role they respectively play on a low-KC flow that we frequently retrieve in porous media apart from the armour layers of breakwaters. Several innovative and practical applications to coastal protection with porous media were also investigated and presented in this thesis.

The work consisted of five successive main parts :

- A state-of-art review to establish and understand theory of flow through porous media.
- The development of a 3D diffraction numerical tool based on Rankine integrals method implementing porous breakwaters.
- Sloshing tests with porous media placed in a tank with water to astutely analyse dissipation coefficients.
- Three scale-model campaigns to acquiring data in order to test and calibrate the numerical model.
- A comparison of the results with those obtained through two others models, a numerical one based on the VOF method and a simple analytical one.

PART 1

# STATE-OF-THE-ART

# 1 BREAKWATER MODELLING

The interaction of water waves with porous coastal structures is a long-standing issue and a richly studied field. Coastal engineers need tools to predict physical processes in order to ensure the stability of infrastructures at sea in the long term and optimise their hydrodynamic performances. Both the transmission and the reflection characteristics of a porous structure are important. Thus, the severity of the wave motion resulting from the partial reflection on the standing breakwater will determine the accessibility of the harbor during storm conditions and will also determine the sediment transport patterns near the structure.

In 1972, Sollitt & Cross [50] linearised the problem of porous media flow in a classical breakwater. One of the objectives of the research was to quickly and reliably evaluate the reflection and transmission coefficients of the structures. Numerous publications have attempted to assess analytically, experimentally and later numerically the coefficients of inertia and friction of a porous medium as well as the hydrodynamic characteristics of the studied structures. The development of numerical techniques to model porous media flows in breakwaters has progressed in term of complexity and computational needs. It started with linearised solutions based on potential theory to very sophisticated eulerian or lagrangian solvers of the Navier-Stokes equations ; the VOF and the SPH methods. The latest developments include turbulence within porous media and 3D simulations. Dentale et al. (2014) [17] model the outer layer of a rubble-mound breakwater by describing every individual 3D blocks. This approach remains a laboratory test and it is unlikely to be easily exported to industry in the very near future. Readers can refereed to the review of Losada & al. (2016) [38] for more details.

A multitude of configurations of rockfill structures were studied in order to find better effectiveness through innovative geometries or compositions. For example, studies with breakwaters using arbitrary sections, Sulisz (1985)[52], vertically stratified, Twu (2002)[56] and Azhar (2008)[2] and with non-uniform porosity Tao (2009)[54] were found. The repetition of porous structures has also been explored by Twu (2004)[55]. Wave damping structures designed from porous vertical screens (slotted or with holes) have been the subject of research following their development in petroleum, coastal and port engineering, Crowley (2011) [47], Suh (2011) [51], Molin (2014)[43] and (2015)[44]. The research deepened with the arrival of the Jarlan caisson with double porous plates, Lajoie (2008)[33] & (2014)[34]. The porous thick wall is a recently explored track, Tamrin (2014)[53] and presents the advantages cited in the context of this subject.

Nevertheless, performing a scale-model tests for the interaction of waves with a porous structure is still today an essential phase of validating a numerical model or an innovative design and it is not a simple matter.

# 2 WAVE: GENERAL EQUATIONS

Commonly, gravity waves, triggered by wind offshore, propagate. The diversity of the external strains lead to a very large range of wave heights and periods. Swell periods count in seconds.

Wave action is the major factor in coastal engineering design. The hydrodynamic efforts received by coastal structures are estimated thanks to mathematical descriptions of swell. In the literature, many of them exist, each one suitable in a particular context. This thesis work mainly uses linear wave theory, which is the basic theory of ocean surface waves applied in ocean, coastal engineering and naval architecture. The integral methods, cited in the introduction and implemented in *Diffra3D* to quickly resolve porous media flow problems, can only handle linear equations. The linear waves are modelled by pure sine (or cosine) functions.

In shallow water, the properties of waves, height and period, change. The shape of waves also transforms as water depth decreases. The waves are less and less sinusoidal. We also observe this in deep water when the size of the waves increases significantly. Linear wave theory leads then to more and more important approximations which an engineer must know how to estimate. Stokes wave theory and cnoidal wave theory are two other wave theories which take into account non-linearities. They describe better the waves in these cases. Le Méhauté (1976) worked on the applicability of wave theories depending on three parameters : the wave height $H$, the wavelength $\lambda$ and the water depth $h$ (see section 1.2.2.1.5).

First of all, linear wave theory is described. Secondly, Stokes and cnoidal wave theories are briefly mentioned. Finally, hydrostatic shallow water equations are introduced because they are used in a simple analytical model.

## 2.1 Potential theories

The interaction between molecules on the free surface can be discarded because they play a very minor role at the scale of this study. The fluid compressibility, which is essential to acoustic waves, can be ignored, just like the Coriolis force because common swell wavelengths are short enough. Finally, the effect of swell on water molecules all along the water depth decrease quickly enough to ignore density stratification of oceans.

In addition to previous assumptions, an ideal flow is considered. The fluid viscosity is discarded. Only constant gravity and constant atmospheric pressure are applied on swell.

An orthonormal coordinate system *Oxyz* such as *Oxy* coincide with the mean free surface and *Oz* is upward (Fig. 2.1).

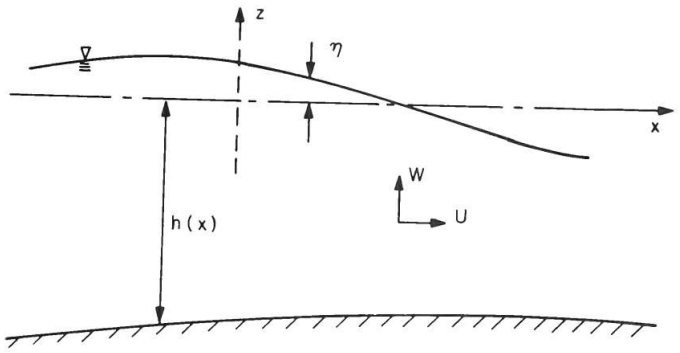


Figure 2.1: Definition sketch, General equations of wave theory

### 2.1.1 Description of the problem

**Continuity equation**

The mass conservation or continuity equation, with the hypothesis of incompressible flow, can be expressed as :

$$\vec{\nabla} . \vec{v}(x,y,z,t) = 0 \tag{2.1}$$

For an ideal flow with constant density, an irrotational flow indefinitely stays irrotational. Far enough from a perturbation, it is usual to consider an irrotational flow (Eq. (2.2)). A velocity potential $\Phi(x,y,z,t)$ can then be introduced (Eq. (2.3)).

$$\overrightarrow{rot}\, \vec{v}(x,y,z,t) = \vec{0} \tag{2.2}$$

$$\text{then } \exists \Phi(x,y,z,t), \text{ such as } \vec{v}(x,y,z,t) = \vec{\nabla}\, \Phi(x,y,z,t) \tag{2.3}$$

With these hypothesis, the continuity equation yields the Laplace equation :

$$\Delta \Phi(x,y,z,t) = 0 \tag{2.4}$$

The Laplace equation is associated with boundary conditions. Two are expressions for the free surface. The free surface is denoted by $z = \eta(x,y,z,t)$ (Fig. 2.1).

**Kinematic condition**

The first one express that a fluid particle at the free surface stays at the free surface. This leads to :

$$\frac{D\eta}{Dt} = \frac{\partial \eta}{\partial t} + \frac{\partial \Phi}{\partial x}\frac{\partial \eta}{\partial x} + \frac{\partial \Phi}{\partial y}\frac{\partial \eta}{\partial y} = \left.\frac{\partial \Phi}{\partial z}\right|_{z=\eta} \tag{2.5}$$

**Dynamic condition**

The second one comes from the Bernouilli equation expressed at the free surface where the pressure $p = p_{atm}$.

$$p = -\rho g \eta - \rho \frac{\partial \Phi}{\partial t} - \frac{1}{2}\rho (\vec{\nabla}\, \Phi)^2 \text{ at } z = \eta \tag{2.6}$$

**Bottom condition**

The last boundary condition is written at the bottom $z = -h(x,y)$ and expressed that the bottom is a solid boundary :

$$\left.\frac{\partial \Phi}{\partial n}\right|_{z=-h} = \frac{\partial \Phi}{\partial z} + \frac{\partial h}{\partial x}\frac{\partial \Phi}{\partial x} + \left.\frac{\partial h}{\partial y}\frac{\partial \Phi}{\partial y}\right|_{z=-h} = 0 \tag{2.7}$$

### 2.1.2 Linear theory

The previous system of equations ((2.4), (2.5), (2.6) & (2.7)) is non linear. It can be linearised by the use of the following assumptions.

The dispersion effects are large compared to non-linear effects. The relative weight of these two effects is given by the Ursell number defined in shallow water as :

$$U_r = \frac{A}{h}\frac{1}{(kh)^2} = \frac{\epsilon}{\mu^2} \quad \text{(shallow water)} \tag{2.8}$$

where $\epsilon = A/h$ is characteristic of non-linearities in shallow water (relative wave amplitude compared to water depth) and $\mu = kh$ is the dispersion parameter. $k$ is the wave number. In deep water, the characteristic parameter of non-linearities is the wave steepness $kA$. The Ursell number is then differently defined :

$$U_r = \frac{kA}{(kh)^3} = \frac{\epsilon'}{\mu^3} \quad \text{(deep water)} \tag{2.9}$$

If $U_r << 1$, a solution to the problem can be searched by developing the potential $\Phi$ with the small parameter $\epsilon$. It is called the perturbation method :

$$\Phi = \epsilon\phi^{(1)} + \epsilon^2\phi^{(2)} + \epsilon\phi^{(3)} + ... \tag{2.10}$$

On the contrary, Ursell number much bigger than 1 comes to non-linear wave theories.

The linear theory or Airy wave theory is the truncation to the first order of equation (2.10). The parameter $\epsilon$ is small enough to discard higher orders. The dynamic and kinematic conditions can be linearised and the kinematic equation is written at $z = 0$ instead of $z = \eta$. The combination of these two equations (Eq. 2.5 & 2.6) leads to the linear free surface condition on a flat bottom :

$$\left.\frac{\partial^2\phi^{(1)}}{\partial t^2} + g\,\frac{\partial\phi^{(1)}}{\partial z}\right|_{z=0} = 0 \iff \begin{cases} \frac{\partial\eta}{\partial t} - \frac{\partial\phi}{\partial z} = 0 \\ \frac{\partial\phi}{\partial t} + g\eta = 0 \end{cases} \tag{2.11}$$

This theory will be used further in the diffraction-refraction numerical model at chapter 2.1.

**Formulation of the progressive monochromatic wave**

An analytic solution of the harmonic problem can be found with the method of separation of variables. $\phi^{(1)}$ is replaced by the simplified notation $\phi$. It can be now written as :

$$\phi(x,y,z,t) = A(x)B(y)C(z)D(t) \tag{2.12}$$

The elementary solution is a progressive monochromatic wave which heads towards the direction making an angle $\beta$ with the $Ox$ axis and is given by :

$$\phi(x,y,z,t) = \Re\left[-\frac{iAg}{\omega}\frac{\cosh(k(z+h))}{\cosh(kh)}\,\mathrm{e}^{i(k(x\cos(\beta)+y\sin(\beta))-\omega t)}\right] \tag{2.13}$$

The verification of the free surface condition leads to the so-called linear dispersion relation, which links the wave-number $k$ to the pulsation $\omega$ :

$$k\tanh(kh) = \frac{\omega^2}{g} \tag{2.14}$$

**Profile of the free surface**

The profile of the free surface is sinusoidal with :

$$\eta = \Re\left[\frac{i\omega}{g}\phi\right]_{z=0} = A\cos(k(x\cos(\beta) + y\sin(\beta)) - \omega t) \tag{2.15}$$

**Orbital velocity**

The elements of the orbital velocity are deduced from the expression of the potential :

$$\begin{aligned} u(x,y,z,t) &= \frac{Agk\cos(\beta)}{\omega}\frac{\cosh(k(z+h))}{\cosh(kh)}\cos(k(x\cos(\beta) + y\sin(\beta)) - \omega t) \\ &= A\omega\cos(\beta)\frac{\cosh(k(z+h))}{\sinh(kh)}\cos(k(x\cos(\beta) + y\sin(\beta)) - \omega t) \end{aligned} \tag{2.16}$$

$$\begin{aligned} v(x,y,z,t) &= \frac{Agk\sin(\beta)}{\omega}\frac{\cosh(k(z+h))}{\cosh(kh)}\cos(k(x\cos(\beta) + y\sin(\beta)) - \omega t) \\ &= A\omega\sin(\beta)\frac{\cosh(k(z+h))}{\sinh(kh)}\cos(k(x\cos(\beta) + y\sin(\beta)) - \omega t) \end{aligned} \tag{2.17}$$

$$\begin{aligned} w(x,y,z,t) &= \frac{Agk}{\omega}\frac{\sinh(k(z+h))}{\cosh(kh)}\sin(k(x\cos(\beta) + y\sin(\beta)) - \omega t) \\ &= A\omega\frac{\sinh(k(z+h))}{\sinh(kh)}\sin(k(x\cos(\beta) + y\sin(\beta)) - \omega t) \end{aligned} \tag{2.18}$$

**Trajectory of particles**

The trajectory of particles is obtained by integrating the velocity field in time in the Langrange system :

$$\frac{dx}{dt} = u(x,y,z,t) \tag{2.19}$$

$$\frac{dy}{dt} = v(x,y,z,t) \tag{2.20}$$

$$\frac{dz}{dt} = w(x,y,z,t) \tag{2.21}$$

The linear theory is valid for "very small" displacements of the fluid. We can thus integrate $u$, $v$ and $w$ at the point $(x_0, y_0, z_0)$ :

$$x(t) = x_0 - A\cos(\beta)\frac{\cosh(k(z_0+h))}{\sinh(kh)}\sin(k(x_0\cos(\beta) + y_0\sin(\beta)) - \omega t) \tag{2.22}$$

$$y(t) = y_0 - A\sin(\beta)\frac{\cosh(k(z_0+h))}{\sinh(kh)}\sin(k(x_0\cos(\beta) + y_0\sin(\beta)) - \omega t) \tag{2.23}$$

$$z(t) = z_0 + A\cos(\beta)\frac{\sinh(k(z_0+h))}{\sinh(kh)}\cos(k(x_0\cos(\beta) + y_0\sin(\beta)) - \omega t) \tag{2.24}$$

The trajectories of particles, under the assumptions of the linear theory, are ellipses. For a very large depth, they form circles for which the radius exponentially decrease with $kz$. In practice, we assume that the bottom has no influence if $kh > 3$. In other words : if the depth is larger than half of the wavelength. On the contrary, the ellipsis flatten as depth decreases. For waves with a long wavelength compared to depth, the trajectories are almost rectilinear.

**Phase velocity and group velocity**

The phase velocity is the velocity of displacement of the crests and troughs. It is defined as :

$$c_p = \frac{\omega}{k} = \sqrt{\frac{g}{k}\tanh(kh)} \tag{2.25}$$

The sea is a dispersive medium. The velocity of waves depends on their wavelength. This assertion is well checked when water depth is deep enough in regards to wavelength. In that case, $kh \gg 1$, then $\omega^2 \approx gk$. The phase velocity $c_p$, velocity of the fluid particles, is then $c_p = \frac{\omega}{k} \approx \sqrt{\frac{g}{k}}$. When $kh \ll 1$, when the wavelength is large in comparison to the water depth, then $\omega^2 \approx ghk^2$. We obtain $c_p \approx \sqrt{gh}$. The sea is not a dispersive medium any more.

The concept of group velocity is the velocity of propagation of the wave energy. At sea, the waves are not strictly monochromatic ones. They form a random field, which can be modelled, inside the linear theory, by a superposition of monochromatic waves with different pulsations $\omega$. If we suppose that every wave has a pulsation close to a pulsation $\omega_0$, we can write :

$$c_g = \frac{\omega - \omega_0}{k - k_0} \tag{2.26}$$

And if $\omega - \omega_0 \to 0$ :

$$c_g = \frac{d\omega}{dk} = \frac{g}{2\omega}\left(\tanh(kh) + \frac{kh}{\cosh^2(kh)}\right) \tag{2.27}$$

The group velocity is thus the velocity of the envelope of a group of waves with close frequencies. The relation between the phase velocity and the group velocity is given by :

$$\frac{c_g}{c_p} = \frac{1}{2} + \frac{kh}{\sinh(2kh)} \tag{2.28}$$

$$\begin{aligned} \text{If} \quad kh \to +\infty : & \qquad c_g = \frac{c_p}{2} \\ \text{If} \quad kh \to 0 : & \qquad c_g = c_p \end{aligned}$$

**Energy of waves**

The total amount of energy of the waves is the sum of the potential energy $E_p$ and of the kinetic energy $E_c$. They are computed for a surface unit of one period. The potential energy is expressed by :

$$E_p = \frac{1}{T}\int_0^T \int_{-h}^{\eta} \rho g z \, \mathrm{d}t \, \mathrm{d}z = \frac{1}{4}\rho g A^2 - \frac{1}{4}\rho g h^2 \tag{2.29}$$

The term $-\frac{1}{4}\rho g h^2$ is the static contribution, the energy of the fluid at rest. It does not have any interest here. The kinematic energy is expressed in deep water by :

$$E_c = \frac{1}{T}\int_0^T \int_{-h}^{\eta} \rho \frac{v^2}{2} \, \mathrm{d}z = \frac{1}{4}\rho g A^2 \tag{2.30}$$

The upper bound of the spacial integral is taken to 0 instead of $\eta$ because we assume the assumptions of the linear theory. The value of energy is thus valid to the first order of steepness.

The mean of the total energy of a wave for one surface unit is equally shared between its potential energy and its kinetic energy. Its expression is given by :

$$E = \frac{1}{2}\rho g A^2 \tag{2.31}$$

The energy flow through an oriented surface of one width unit and for all the water depth is obtained by writing the variation of energy in time. Its definition is given by :

$$F(t) = \int_{-h}^{0} \frac{\partial \phi}{\partial t} \overrightarrow{\nabla} \phi . \vec{n} \, \mathrm{d}z = \int_{-h}^{0} -\rho \frac{\partial \phi}{\partial t} \left[ \frac{\partial \phi}{\partial x} + \frac{\partial \phi}{\partial y} \right] \mathrm{d}z \tag{2.32}$$

The mean value for one period is :

$$\bar{F} = \frac{1}{2} \rho g A^2 c_p \left[ \frac{1}{2} + \frac{kh}{\sinh(2kh)} \right] = E c_g \tag{2.33}$$

The relation $\bar{F}/E$ is thus the mean velocity of the energy. The velocity of the energy is equal to the group velocity.

### 2.1.3 Stokes wave theory

If the amplitude rises or the depth reduces, the little parameter $\epsilon = A/h$ or $\epsilon' = kA$ rises. The crests become progressively sharper and the troughs flatter. The linear theory is then less and less accurate in defining regular waves and the development of the equation (2.10) to higher orders is required (Fig. 2.2). The dispersion relation then becomes dependent on the wave amplitude.

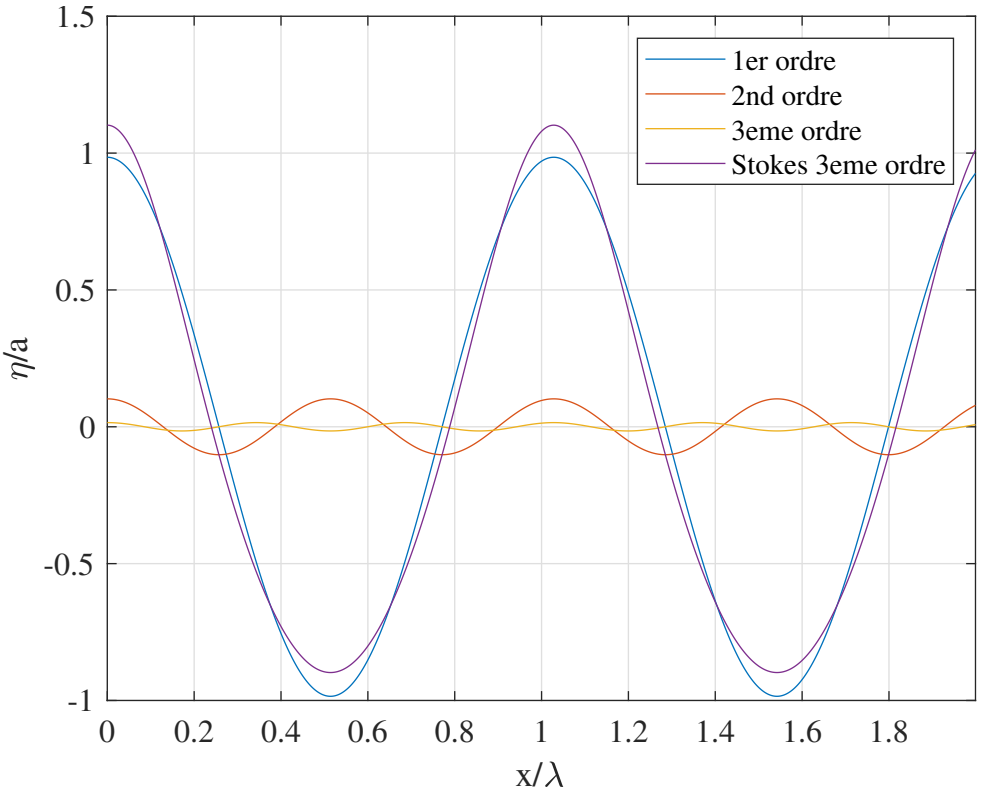


Figure 2.2: Third order Stocks wave and harmonics

The expansion to higher orders can be numerically done following the stream function method. The flow velocity components are expressed as the derivatives of a scalar stream function $\Psi(x,z)$ such as $u = -\frac{\partial \Psi}{\partial x}$ and $w = \frac{\partial \Psi}{\partial z}$. In our case, the free surface elevation $\eta(x)$ is assumed to be periodic and symmetric in relation to the crest. The stream function can then be solved as (following Molin (2002) [42]) :

$$\frac{k\Psi(x,z)}{C_{PE}} = -k(z+h) + \sum_{j=1}^{N} a_j \frac{\sinh\left(jk(z+h)\right)}{\cosh(jkh)} \cos(jkx) \tag{2.34}$$

where N is the truncation order, $C_{PE}$ is the phase velocity and $a_j$ some coefficients.

The slip condition on the bottom ($\Psi(x,-h)=0$) and the continuity condition ($\Delta\Psi=0$) are automatically verified. Then, the kinematic and dynamic conditions can respectively be expressed as :

$$\Psi(x,\eta(x)) = -Q \tag{2.35}$$

$$\frac{1}{2}(\Psi_x^2+\Psi_z^2)+g\eta = R \tag{2.36}$$

Q and R are two unknowns constants.

The interval $[0,L/2]$ is discretisated in $M+1$ points of abscissa $iL/(2M)$ of unknown elevations $\eta_i$. We obtain $2M+2$ equations for $M+N+4$ unknowns. The mean value of the free surface, the height of the wave $H$ and the period $T$ give 3 more equations to add to the previous linear system :

$$\eta_0+\eta_M+2\sum_{i=1}^{M-1}\eta_i = 0 \tag{2.37}$$

$$\eta_0-\eta_M = H \tag{2.38}$$

$$T = \frac{L}{C_{PE}+U_C} \tag{2.39}$$

with $U_C$ the eulerian stream velocity.

Examples of solution are shown in figure 2.2.

The development to high orders shows that there is a maximum wave steepness. The limit is reached when the wave orbital velocity at the crest is equal to the phase velocity. At this moment, the shape of the wave at the crest corresponds to a dihedral with an angle of strictly 120°.

The wave of Stokes is subject to a breaking criterion which applies when the velocity of the fluid particles exceeds the wave phase velocity. It is determined by (Miche 1944) :

$$\frac{H}{\lambda} = 0.14\tanh(kh) \tag{2.40}$$

The stream function method described above makes the link between the Stokes wave theory and the Cnoidal wave theory, which is used to model waves in shallow water.

### 2.1.4 Cnoidal wave theory

The Cnoidal wave theory is developed under the assumption of shallow water, always in regards to the wavelength. It may occur when the waves are ready to end up on the beach. In that case, kh is small ($kh<0.3$) and the Ursell number becomes high ($U_r \gg 1$).

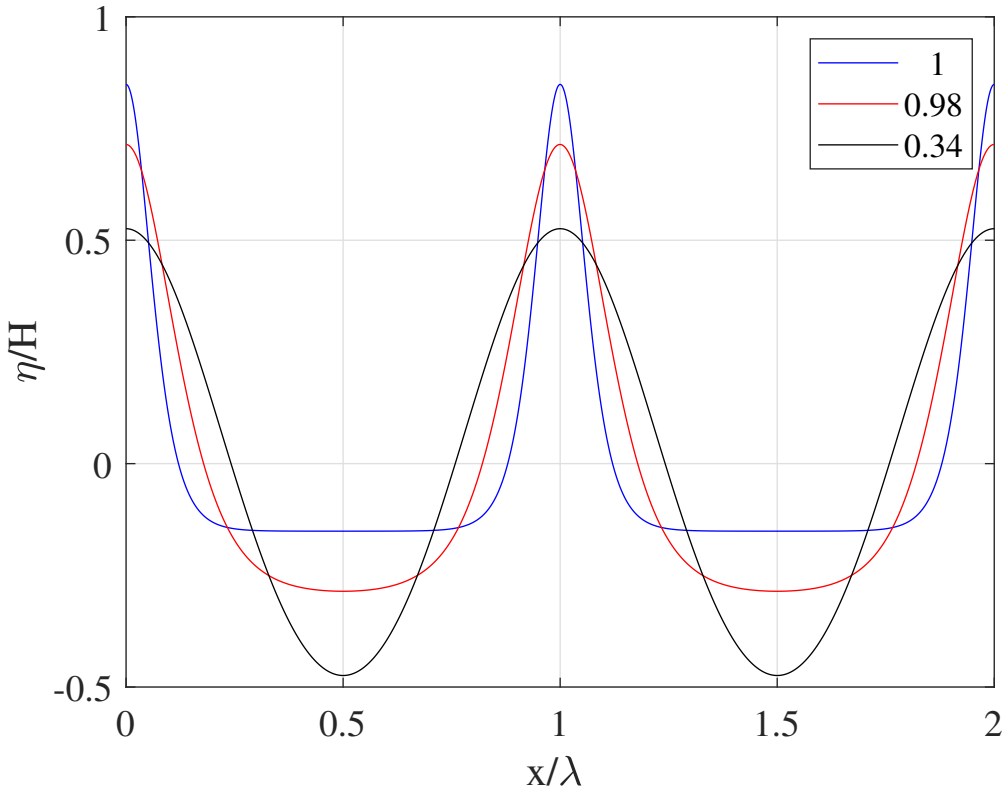


Figure 2.3: Cnoidal waves (m=0.34 : black, m=0.98 : red, m=1 : blue)

By adopting the origin of the vertical coordinate at the bottom ($Z = z - h$), we can assume that the potential can be developed as a power series of the vertical coordinate (Boussinesq) :

$$\Phi(x,Z,t) = \sum_{n=0}^{+\inf} \frac{Z^n}{n!} \left.\frac{\partial \Phi}{\partial Z^n}\right|_{Z=0} \tag{2.41}$$

This form of potential is introduced in the Laplace equation, associated to the boundary conditions. The truncation of series after the first order in $\epsilon'$ and $\mu^2$ leads to the well-known non-linear equation of Korteweg-de Vries (1985) [29] (Whitam (1974) [63]) :

$$\frac{\partial \eta}{\partial t} + \sqrt{gh}\frac{\partial \eta}{\partial x} + \frac{\partial \eta}{\partial x} + \frac{3}{2}\sqrt{\frac{g}{h}}\eta\frac{\partial \eta}{\partial x} + \frac{h^2}{6}\sqrt{gh}\frac{\partial^3 \eta}{\partial x^3} = 0 \tag{2.42}$$

The analytical solution, under the form of a progressive wave of velocity $c$, exists. A rigorous demonstration can be found in Lajoie (1996) [32]. It is expressed through a Jacobi elliptic function of the first kind with a $m$ parameter as :

$$\eta = \eta_2 + H\,cn^2\left[\frac{K(m)}{\pi}k(x-ct), m\right] \tag{2.43}$$

with :

- $\eta_2$ the trough elevation defined as :

$$\eta_2 = \frac{H}{m}\left(1 - m - \frac{E(m)}{K(m)}\right) \tag{2.44}$$

- $E$ is the complete elliptic integral of second kind of parameter $m$.
- $K$ is the complete elliptic integral of first kind of parameter $m$.
- $cn$ is the cosine function of Jacobi of parameters $u$, $m$.
- $c$ the phase velocity is defined by $c = \sqrt{gh}\left(1 + \frac{H}{h} - \frac{2}{3}K^2(m)k^2h^2\right)$.
- $k = 2\pi/\lambda$ the wave number.

The shape of the wave depends on the wave height $H$ and on the wavelength $\lambda$. It depends also on the parameter $0 \leq m \leq 1$. This parameter is directly linked to $H$, $\lambda$ and $h$ as :

$$K(m) = \frac{\sqrt{3}}{2}\sqrt{\frac{H}{h}}\frac{1}{\sqrt{m}}\frac{\lambda}{2h}, \text{ from where } U_r = \frac{16}{3}mK^2(m) \tag{2.45}$$

As the other non-linear wave theories, the wave amplitude is included in the dispersion relation. If the parameter $m$ decreases towards 0, the Cnoidal wave theory meets the linear theory for long waves and the limit for the celerity is $c = \sqrt{gh}$ (Fig. 2.3). The other limit corresponds to the solitary wave theory (Fig. 2.4) and is obtained for $m = 1$. The elevation of the wave becomes :

$$\eta = \frac{H}{\cosh^2\left[\frac{3a}{4h^2}(x - ct)\right]} \text{ with } c = \sqrt{gh(1 + \frac{H}{2h})} \approx \sqrt{g(h + H)} \tag{2.46}$$

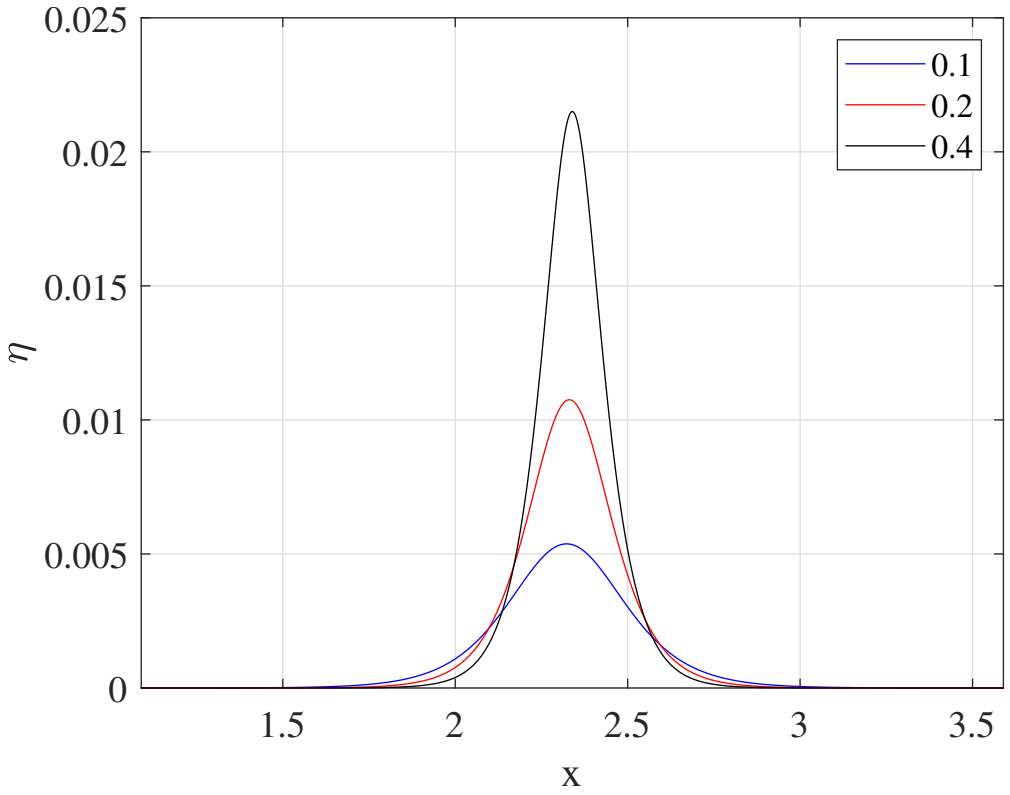


Figure 2.4: Solitary wave ($a/h = 0.4$ : black, $a/h = 0.2$ : red, $a/h = 0.1$ : blue)

### 2.1.5 Validity of different waves theories

Every wave theory has its own scope to best describe the different effects involved. Le Mehauté (1976) worked on the applicability of the different theories function of the wave steepness and of the relative depth. For example, the diagram 2.5 below has a direct application in the analysing method of reflection-transmission experimental tests described and used further in this work, see chapter 1.5. The characteristics of the waves performed in the experimental campaigns of Vintimille (Chap. 3.3) and Banyuls & Istres (Chap. 3.4) are showed on the figure.

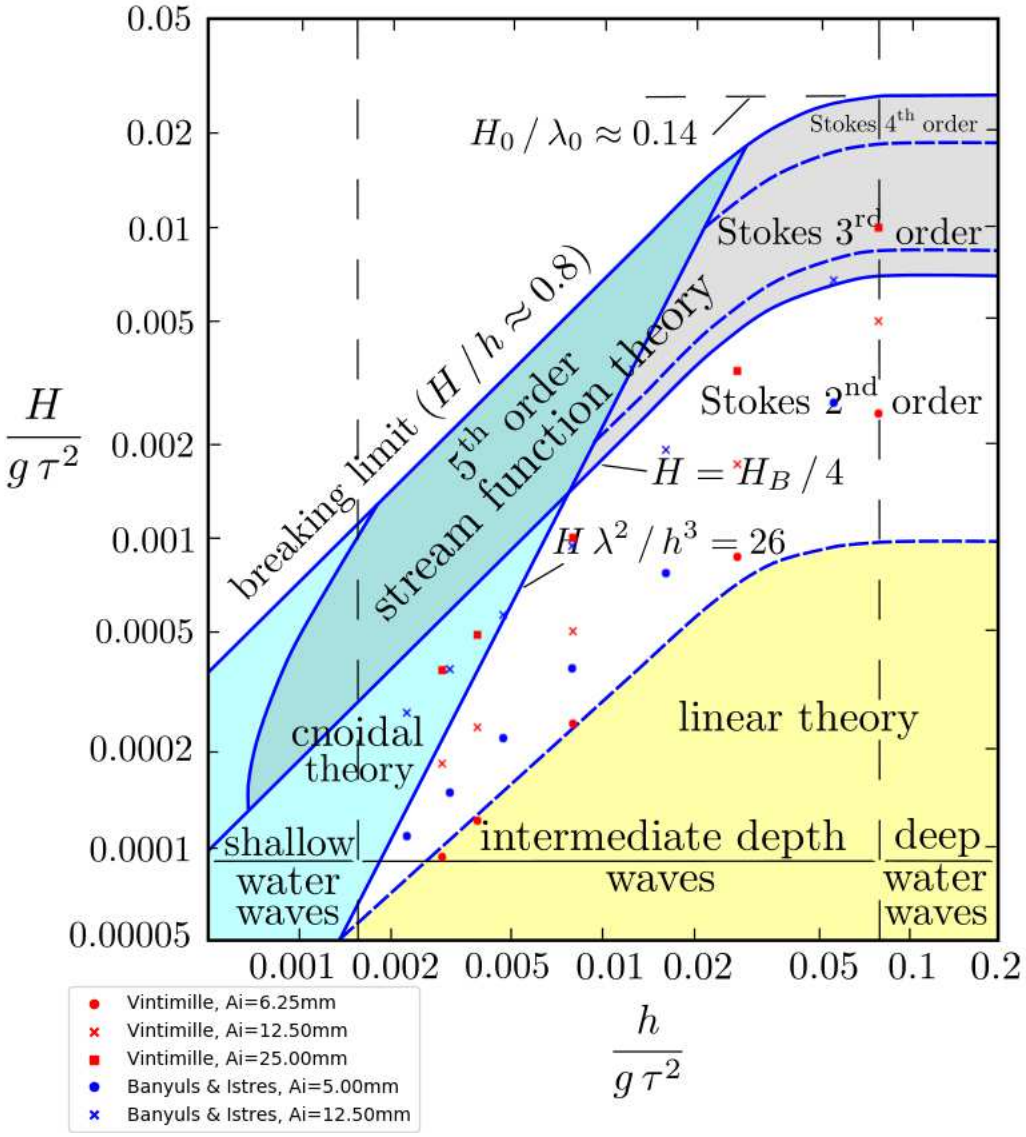


Figure 2.5: Applicability of wave theories, Le Mehauté (1976)

## 2.2 Hydrostatic Shallow water equations

The hydrostatic shallow water equations or also known as the 2D Saint-Venant equations are a set of equations derived from depth-integrating the general equations of fluid mechanics. A simple form of these equations are used in the analytical model presented in the chapter 2.4.

We start again with the continuity equation (2.47), the Euler equation Eq. (2.48) and the three boundary conditions Eq. (2.49), (2.50) and (2.51)

Continuity
$$\overrightarrow{\nabla}.\vec{v} = 0 \tag{2.47}$$

Conservation of momentum
$$\frac{\partial \vec{v}}{\partial t} + (\vec{v}.\overrightarrow{\nabla})\vec{v} = -\frac{1}{\rho}\overrightarrow{\nabla} p - \vec{g} \tag{2.48}$$

No-slip bottom condition
$$\vec{v}|_{z=-h} = \vec{0} \tag{2.49}$$

Kinematic condition
$$\frac{\partial \eta}{\partial t} + \vec{v}.\overrightarrow{\nabla}\eta\Big|_{z=\eta} = v_z \tag{2.50}$$

Dynamic condition
$$p\big|_{z=\eta} = p_{atm} \tag{2.51}$$

where the bottom is defined by a function $h(x,y)$. The water depth is thus defined as $h' = h + \eta$.

Now, we deal with the main assumption of the shallow water equations : the horizontal length scale is much greater than the vertical length scale. We introduce $\lambda$, the wavelength for the horizontal direction and $h'$, the water depth for the vertical direction. The continuity equation shows that the order of magnitude of the vertical velocity component is given by $v_z = \mathrm{O}(\frac{h'}{\lambda} v_x)$. The vertical velocity scale is thus small compared to the horizontal velocity scale. This assumption suggests that $\frac{Dv_z}{Dt}$ can be neglected in equation (2.48) as the term in $v_z \frac{\partial}{\partial z}$.

Now, it is rational to assume a hydrostatic pressure distribution. It follows that :

$$\frac{\partial p}{\partial x} = \rho g \frac{\partial \eta}{\partial x} \tag{2.52}$$

$$\frac{\partial p}{\partial y} = \rho g \frac{\partial \eta}{\partial y} \tag{2.53}$$

$$\frac{\partial p}{\partial z} = -\rho g \tag{2.54}$$

Substituting these equations into equation (2.48) leads to :

$$\frac{\partial v_x}{\partial t} + v_x \frac{\partial v_x}{\partial x} + v_y \frac{\partial v_x}{\partial y} = -g \frac{\partial \eta}{\partial x} \tag{2.55}$$

$$\frac{\partial v_y}{\partial t} + v_x \frac{\partial v_y}{\partial x} + v_y \frac{\partial v_y}{\partial y} = -g \frac{\partial \eta}{\partial y} \tag{2.56}$$

We introduce the depth-average speeds $\bar{v_x}$ and $\bar{v_y}$ such as :

$$\bar{v_x} = \frac{1}{h'} \int_{-h}^{\eta} v_x \, \mathrm{d}z \tag{2.57}$$

$$\bar{v_y} = \frac{1}{h'} \int_{-h}^{\eta} v_y \, \mathrm{d}z \tag{2.58}$$

The equations (2.55) and (2.56) can be integrated over the depth using the Leibniz's rule and the boundary conditions. It becomes :

$$\frac{\partial \bar{v_x}}{\partial t} + \bar{v_x} \frac{\partial \bar{v_x}}{\partial x} + \bar{v_y} \frac{\partial \bar{v_x}}{\partial y} = -g \frac{\partial \eta}{\partial x} \tag{2.59}$$

$$\frac{\partial \bar{v}_y}{\partial t} + \bar{v}_x \frac{\partial \bar{v}_y}{\partial x} + \bar{v}_y \frac{\partial \bar{v}_y}{\partial y} = -g \frac{\partial \eta}{\partial y} \tag{2.60}$$

Integrating the continuity equation over the depth, we obtain :

$$0 = \int_{-h}^{\eta} \overrightarrow{\nabla} . \vec{v} \, \mathrm{d}z$$

$$= \frac{\partial}{\partial x} \int_{-h}^{\eta} v_x \, \mathrm{d}z + \frac{\partial}{\partial y} \int_{-h}^{\eta} v_y \, \mathrm{d}z - \left[ v_x|_{z=\eta} \frac{\partial \eta}{\partial x} + v_y\big|_{z=\eta} \frac{\partial \eta}{\partial z} - v_z|_{z=\eta} \right] + \left[ v_x|_{z=-h} \frac{\partial \eta}{\partial x} + v_y\big|_{z=-h} \frac{\partial \eta}{\partial z} - v_z|_{z=-h} \right]$$

$$= \frac{\partial (h' \bar{v}_x)}{\partial x} + \frac{\partial (h' \bar{v}_y)}{\partial y} + \frac{\partial h'}{\partial t}$$

Here, the three dimensional shallow water equations :

$$\frac{\partial (h' \bar{v}_x)}{\partial x} + \frac{\partial (h' \bar{v}_y)}{\partial y} + \frac{\partial h'}{\partial t} = 0 \tag{2.61}$$

$$\frac{\partial \bar{v}_x}{\partial t} + \bar{v}_x \frac{\partial \bar{v}_x}{\partial x} + \bar{v}_y \frac{\partial \bar{v}_x}{\partial y} = -g \frac{\partial \eta}{\partial x} \tag{2.62}$$

$$\frac{\partial \bar{v}_y}{\partial t} + \bar{v}_x \frac{\partial \bar{v}_y}{\partial x} + \bar{v}_y \frac{\partial \bar{v}_y}{\partial y} = -g \frac{\partial \eta}{\partial y} \tag{2.63}$$

The analytical model presented in chapter 2.4 uses a linear form of these equations for a 1D linear reflection-transmission problem. Assuming very small amplitudes of waves to depth, we can discard the advection terms and take $h' \approx h$. The linearised 1D shallow water equations becomes :

$$\frac{\partial \eta}{\partial t} + h \frac{\bar{v}_x}{\partial x} = 0 \tag{2.64}$$

$$\frac{\partial \bar{v}_x}{\partial t} + g \frac{\partial \eta}{\partial x} = 0 \tag{2.65}$$

# 3 DESCRIPTION OF A SIZE DISTRIBUTION

## 3.1 Rock description

The simplest measurement of a block is its mass, which is determined by weighing. Thus, the geometric parameter of a granular material varies between different references, $d$, $d_E$, $d_{15}$, $d_{50}$ and $d_{n50}$ defined as follows :

- $d$ can refer to two definitions :
  - The diameter of spheres or cylinders authors work with to model idealised porous medium in numerical or experimental researches.
  - The dimension of square sieve fitting with the block.
- $d_E$ is the diameter of a sphere that has a volume equal to the average volume of the grains.
- $d_{50}$ corresponds to median diameter of rocks. $d_{15}$ is the diameter bound for which 85% of grains are bigger.
- $d_{n50}$ is the nominal median diameter which is the diameter of the cube that has a volume equal to $d_{50}$.

The nominal diameters $d_{n50}$, $d_{n15}$ and $d_{n85}$ are today the most used parameters to define a specific size distribution (set of rocks).

The diameter $d$ and the diameter $d_n$ are proportional for a given type of rocks. The usual ratio is :

$$d_n = 0.84d \tag{3.1}$$

## 3.2 Gradation of a size distribution

The overall slope of the grading curve is an indicator of the uniformity of the size distribution and is generally referred to a gradation or granular extent. A quantitative estimate of this uniformity can be made using the ratio $M_{85}/M_{15}$ or $d_{85}/d_{15}$. As for $d_{15}$ concerning the stones diameters, $M_{15}$ is the weight bound for which 85% of the stones are heavier. The table 3.1 describes the different gradations, expressed as mass and diameter ratios.

| **Type of size distribution** | $d_{n85}/d_{n15}$ | $M_{85}/M_{15}$ |
|---|---|---|
| **Low gradation or narrow size distribution** | <1.5 | 1.7–2.7 |
| **High gradation or spread size distribution** | 1.5–2.5 | 2.7–16 |
| **Very high gradation or very spread size distribution** | 2.5–5.0 | 16–125+ |

Table 3.1: Gradation of rocks in terms of uniformity, Rock manual [9]

According to the Rock manual [9], the size distribution plays a major role :

- on the filtration characteristics,
- in the final porosity $n$ of a layer of bulk blocks.

The porosity of a porous layer in a classical breakwaters (under layer or core) depends on the uniformity of the size distribution and on the shape of the rocks. The porosity $n$ of bulk materials can be estimated by (Tsirel (1997) [9]) :

$$e = \frac{1}{90} e_0 \arctan(0.645 n_{RRD}) \tag{3.2}$$

$$n = \frac{e}{1+e} \tag{3.3}$$

where $e$ is the void ratio of the size distribution and $e_0$ is the void ratio if all blocks were one size. $e_o$ for different shapes of rocks is given in the table below.

| **Type of materials** | **Cubic** | **Elongated** | **Flat** | **Crushed** | **Shingles** |
|---|---|---|---|---|---|
| **Void ratio $e_0$** | 0.88–0.92 | 0.93–0.96 | 1.00–1.03 | 0.92–0.96 | 0.65–0.80 |

Table 3.2: Coefficient $e_0$, Rock manual [9]

$n_{RRd}$ is another indicator for measuring the gradation of a size distribution. $n_{RRd}$ is called coefficient of uniformity and it is defined by :

$$n_{RRd} = \log\left(\frac{\log(1-y_{NUL})}{\log(1-y_{NNL})}\right) \Big/ \log(NUL/NLL) \tag{3.4}$$

with $y_{NUL} = 0.9$ the upper nominal limit and $y_{NLL} = 0.06$ the lower nominal limit. $NUL$ and $NLL$ are the nominal diameters associated with the limits $y_{NUL}$ and $y_{NLL}$.

The figure 3.1 is an example of a size distribution. This one is used for the experimental tests of chapter 3.3. The coefficient of uniformity represents the slope of the grading curve. The coefficient of consistency can also be expressed as the function of the weight of the stones. $n_{RRd}$ becomes $n_{RRM}$ with $n_{RRd} \approx 3 n_{RRM}$.

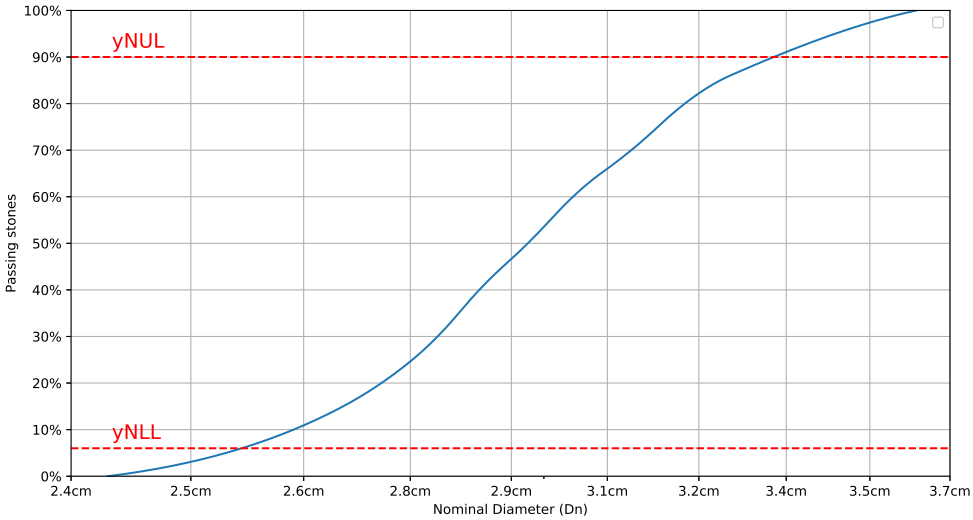


Figure 3.1: Size distribution, Vintimille

In practise, the equation (3.3) has be to used with caution. The mode of discharge of the blocks also plays a role in the final porosity of a layer. In addition, the empirical law of Tsirel was not developed for discharge in water [9].

For the innovative vertical riprap structures which are mentioned in this thesis work, the operators laying method depends on the size of the blocks. Little stones (shingles) will be just discharged in the cage. Bigger stones must be placed one by one. The constraint of the walls of the cage compared to a free stack of stones also changes the porosity of the final porous medium.

# 4 FLOW THROUGH POROUS MEDIA

Flow inside porous medium has been studied since the latter half of the 19th century. The first theoretical formulation is the well-known Darcy law (1856) [13]. The Darcy equation is an empirical relation based on experimental observations of 1D flow through a porous medium that is assumed to be homogeneous. It introduces the intrinsic permeability constant $K$ of the medium to the steady laminar flow. The Darcy equation expresses the hydraulic gradient $-\frac{1}{\rho g}\frac{\partial p}{\partial x}$ as :

$$-\frac{1}{\rho g}\frac{\partial p}{\partial x} = \frac{\nu}{gK} v_d \tag{4.1}$$

with :

- $v_d$ is the Darcy velocity, or filter velocity ($m.s^{-1}$).
- $K$ is the intrinsic permeability of the porous medium ($m^2$).
- $\nu$ is the kinematic viscosity ($m^2.s^{-1}$).

Kozeny-Carman law details the parameter $K$ in order to describe filtration phenomenon through a packed bed of solids. The equation was derived by Kozeny (1927) [30] and Carman (1937, 1956) [6] & [7]. The equation is still only valid for laminar flow. The notion of specific surface area $S$ is used in their formulation. expressed as :

$$-\frac{1}{\rho g}\frac{\partial p}{\partial x} = k_o \frac{(1-n)^2}{n^3}\frac{\nu S_c^2}{g} v_d \tag{4.2}$$

with :

- $k_o$ is the Kozeny constant (commonly between 3 and 6).
- $n$ is the porosity.
- $S_c$ is the specific surface area of the grains ($m^{-1}$).

The intrinsic permeability can be now expressed by :

$$K = \frac{1}{k_o}\frac{n^3}{(1-n)^2}\frac{1}{S_c^2} \tag{4.3}$$

If we consider $d = 6/S_c$ the mean diameter for the spherical solid particles forms an idealised porous medium with the same specific surface area $S$. The equation (4.2) can be further expressed as :

$$K = \frac{1}{36k_o}\frac{n^3}{(1-n)^2} d^2 \tag{4.4}$$

The Kozeny-Carman equation is widely used to evaluate soil permeability. Nowadays, in order to improve this equation, a lot of publications try to better estimate the permeability-porosity relationship of porous media by means of fractal geometry : Costa (2006) [11], Xu & Yu (2008) [65], Valdes-Parada et al. (2009) [57], Henderson et al. (2010) [22], Latief & Fauzi (2012) [35], Kun-Can et al. (2017) [31] and Chen & al. (2018) [8].

Forchheimer (1901), following Dupuit's work (1863), expressed the hydraulic gradient through a porous medium for a non-Darcy flow (non-laminar flow) by adding a quadratic term $bv_d$. The Forchheimer equation is then extended by Polubarinova-Kochina (1962) [46] with an inertial term $c\frac{\partial v_d}{\partial t}$ in order to describe non-steady flow. The extended equation of Forchheimer expressed the hydraulic gradient as :

$$-\frac{1}{\rho g}\frac{\partial p}{\partial x} = av_d + bv_d|v_d| + c\frac{\partial v_d}{\partial t} \tag{4.5}$$

where a, b and c are coefficients that correspond to the considered porous medium.

This empirical expression of resistance terms is still frequently used to model the hydraulic gradient through porous media. The scientific emulation about this field has been important in order to give a theoretical background to the formulation by averaging the Navier-Stokes equation (Van Gent (1991) [58]) and to give a physical meaning to the coefficients a, b and c (Hassanizadeh & Gray (1987) [21]). The porous medium is considered as a continuous medium. This technique avoids modelling the complex network of pores and rocks (Fig. 4.1).

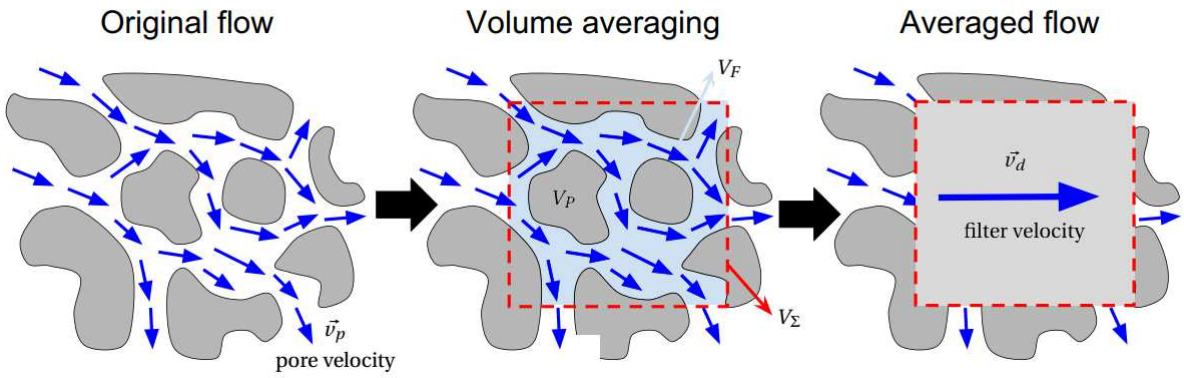


Figure 4.1: Sketch of the volume-averaging process for resolution of the porous flow, Losada & al. (2016) [38]

As observed by Van Gent (1991) [58], the equation (4.5) does not include a possible resistance force due to the presence of a convective term (H1). A resistance term may be important when considering flow through a porous medium that has considerable large-scale convective transport. Such a resistance term could be incorporated in the b term, because it would be quadratic in velocity.

We have also to note that the viscous and turbulence shear stress are also neglected (H2). Considering the viscous shearing effect between the fluid and the pore walls, Brinkman (1947) added the second-order derivatives of the velocity to the Darcy equation, resulting in the Brinkman equation (Civan & Tiab (1991) [10]) :

$$-\frac{1}{\rho g}\frac{\partial p}{\partial x} = \frac{\nu}{gK}v_d - \frac{\nu}{g}\left(\frac{\partial^2 v_d}{\partial y^2} + \frac{\partial^2 v_d}{\partial z^2}\right) \tag{4.6}$$

For flow with a high Reynolds number, a new dominating term mest be added. It corresponds to the turbulent shear stress or Reynolds stress. As Van Gent (1991-1995) and Burcharth & Andersen (1995), we assume the hypothesis (H1) and (H2) for our porous flow model.

The model presented in equation (4.5) was recently updated by Lin & Karunarathna (2007) [37] by including a new drag term. This experimental new porous flow model is an extension of the extended Forchheimer equation to consider the drag component that appears in the transition from laminar to turbulent flow. Equation Eq. (4.5) can then be transformed into :

$$-\frac{1}{\rho g}\frac{\partial p}{\partial x} = av_d + bv_d|v_d| + dv_d\sqrt{v_d} + c\frac{\partial v_d}{\partial t} \tag{4.7}$$

where d is the new coefficient.

To determine the magnitude of the frictional forces, porous flow parameters a, b, c and d need to be defined. Most of the works existing in the literature are focused on the analysis of a, b, and c. The porous flow model presented by Lin & Karunarathna (2007) is not yet broadly used, mainly because it requires the determination of a new parameter, d, as suggested by Losada & al. (2016) [38].

## 4.1 Forces of inertia

By considering only the inertia loads that apply to the fluid in a small closed porous domain $\Sigma$ of volume $V_\Sigma$ (Fig. 4.1), we can write the momentum equation. With a simplified notation for the small volume $V_F$ and $V_P$, it yields :

$$V_F \frac{\partial \vec{v}_p}{\partial t} = -\frac{1}{\rho}(V_P + V_F)\,\overrightarrow{\nabla}\, p_I - (1 + C_a) V_P \frac{\partial \vec{v}_p}{\partial t} \tag{4.8}$$

where :

- F is the fluid domain of volume $V_F$ (Fig. 4.1).
- P the rock domain of volume $V_P$.
- $\vec{v}_p$ the **pore** velocity. The relation with the filter velocity is given by $\vec{v}_p = n\vec{v}_d$.
- $\overrightarrow{\nabla}\, p_I$ the pressure gradient corresponding to the inertial part, applying thus on the global exterior surface $\partial\Sigma$.

Following Burcharth & Andersen (1995) [4] : "*for a fixed body exposed to a flow, $C_M = 1 + C_a$. $C_M$ is the inertia coefficient, 1 relates to the Froude-Krylov force and $C_a$ is the added mass coefficient. For a single smooth cylinder $C_a = 1$ and $C_M = 2$. $C_a$ and $C_M$ correspond to the conventional definition of the Morison equation and depend on $R_e$, $KC$, and the relative surface roughness $\frac{k}{d}$. However, for an array of cylinders, the drag coefficient, $C_m$* ***depends also on n***".

Dividing equation (4.8) by $V_\Sigma = V_F + V_P$, it yields :

$$n\frac{\partial \vec{v}_p}{\partial t} = -\frac{1}{\rho}\,\overrightarrow{\nabla}\, p_I - (1 + C_a)(1 - n)\frac{\partial \vec{v}_p}{\partial t} \tag{4.9}$$

With the introduction of the filter velocity $\vec{v}_d$, we obtain :

$$\frac{1}{n}(1 + C_a(1 - n))\frac{\partial \vec{v}_d}{\partial t} = -\frac{1}{\rho}\,\overrightarrow{\nabla}\, p_I \tag{4.10}$$

Here, two different formulations are proposed in the literature. The first is derived by Sollit & Cross (1972) [50] and re-expressed by Van Gent (1993) [59] :

$$\frac{(1 + \gamma_p \frac{1-n}{n})}{n}\frac{\partial \vec{v}_d}{\partial t} = -\frac{1}{\rho}\,\overrightarrow{\nabla}\, p_I \tag{4.11}$$

with $\gamma_p$ an empirical coefficient (Van Gent 1993 [59]). $\gamma_p$ is often taken equal to 0.34 but it has also its own expression :

$$\gamma_p = 0.85 - \frac{0.015}{A_c} \quad \text{for} \quad A_c > \frac{0.015}{\frac{n}{1-n} + 0.85} \quad \text{with} \quad A_c = \frac{\hat{v_d}}{Tng} \tag{4.12}$$

However authors like Burcharth & Andersen (1995) [4] declared this formulation incorrect because it is divided by $n$. In his development Van Gent (1993) [59] exclusively expressed the pressure gradient on the fluid domain $F$ when it applies on the global domain $\Sigma$.

If we rewrite the equation (4.10) by replacing the added mass coefficient $C_a$ with the inertia coefficient $C_M = 1 + C_a$, we obtain the expression of Burcharth & Anderson (1995) [4] :

$$(1 + C_M \frac{1 - n}{n})\frac{\partial \vec{v}_d}{\partial t} = -\frac{1}{\rho}\,\overrightarrow{\nabla}\, p_I \tag{4.13}$$

## 4.2 Formulation of drag coefficients

A lot of scientists have suggested their own developments of drag coefficients based on empirical, semi-empirical and theoretical formulations. The table Tab. 4.1 is a sum-up of the different and most important formulations which have been used in coastal engineering.

| Author(s) | a | b | d |
|---|---|---|---|
| Carman (1937) | $\alpha\frac{(1-n)^2}{n^3}\frac{\nu}{gd^2}$ $\alpha = 180$ | 0 | 0 |
| Ergün (1952) | $\alpha\frac{(1-n)^2}{n^3}\frac{\nu}{gd^2}$ $\alpha = 150$ | $\beta\frac{(1-n)}{n^3}\frac{1}{gd}$ $\beta = 1.75$ | 0 |
| Engelund (1953) [58] | $\alpha\frac{(1-n)^3}{n^2}\frac{\nu}{gd_E^2}$ $\alpha = 780-1500$ | $\beta\frac{(1-n)}{n^3}\frac{1}{gd_E}$ $\beta = 1.8-3.6$ | 0 |
| Le Méhauté (1957) | $\alpha\frac{1}{n^5}\frac{\nu}{gd^2}$ $\alpha = 14$ | $\beta\frac{1}{n^5}\frac{1}{gd}$ $\beta = 0.1$ | 0 |
| Ward (1964) [62] | $\frac{\nu}{gK}$ | $\frac{C_f}{g\sqrt{(K)}}$ $C_f = 0.55$ | 0 |
| Keulegan (1973) [27] | 0 | $\frac{C_f}{gd}$ $C_f = C\left(\frac{v_d d}{\nu}\right)^{n(R_{ed})}$ | 0 |
| Koenders (1985) [28] | $\alpha\frac{(1-n)^2}{n^3}\frac{\nu}{gd_{15}^2}$ | $\beta\frac{1}{n^5}\frac{1}{gd_{15}}$ | 0 |
| Den Adel (1987) [16] | $\alpha\frac{(1-n)^2}{n^3}\frac{\nu}{gd_{15}^2}$ | $\beta\frac{1}{n^2}\frac{1}{gd_{15}}$ | 0 |
| Shih (1990) [48] | $\alpha\frac{(1-n)^2}{n^3}\frac{\nu}{gd^2}$ $\alpha = 1684+3.12\cdot 10^{-3}\left(\frac{g}{\nu^2}\right)^{\frac{2}{3}}d_{15}^2$ | $\beta\frac{(1-n)}{n^3}\frac{1}{gd}$ $\beta = 1.72+1.57\exp\left(-5.1\cdot 10^{-3}\left(\frac{g}{\nu^2}\right)^{\frac{1}{3}}d_{15}\right)$ | 0 |
| Van Gent (1993) [59] | $\alpha\frac{(1-n)^2}{n^3}\frac{\nu}{gd_{n50}^2}$ | $\beta\left(1+\frac{7.5}{KC}\right)\frac{(1-n)}{n^3}\frac{1}{gd_{n50}}$ | 0 |
| Burcharth & Andersen (1995) [4] | $\alpha\frac{(1-n)^2}{n^3}\frac{\nu}{gd^2}$ | $\beta\frac{(1-n)}{n^3}\frac{1}{gd}$ | 0 |
| Lin & Karunarathna (2007) [37] | $\alpha\frac{(1-n)^2}{n^3}\frac{\nu}{gd_{n50}^2}$ | $\beta\left(1+\frac{7.5}{KC}\right)\frac{(1-n)}{n^3}\frac{1}{gd_{n50}}$ | $4.5\frac{(1-n)}{n^3}\frac{\nu^{\frac{1}{2}}}{gd_{n50}^{\frac{3}{2}}}$ |

Table 4.1: Parameter formulations, Literature review.
$\alpha$ and $\beta$ are tortuosity coefficients. $C_f$ is a resistance coefficient.

The relation between friction coefficients presented by Burcharth & Andersen (1995) [4] and those used by Ward (1964) [62] are :

$$K = \frac{n^3 d_{n50}^2}{\alpha(1-n)^2} \tag{4.14}$$

$$C_f = \frac{\beta}{\sqrt{\alpha}} n^{-\frac{3}{2}} \tag{4.15}$$

The expression of the intrinsic permeability $K$ is almost the same as the one in Kozeny-Carman equation (4.3).

Nowadays, the widely admitted and applied form of resistance model for steady and non-steady flow through granular porous media is the one proposed by Ergün (1952) and re-express by Van Gent (1993) [59] and Burcharth & Andersen (1995) [4]. As mentioned before, Van Gent derived the equations from averaging the Navier-Stokes equation by applying a cylinder analogy to model the pores of the porous medium. As it is previously noted, the formulation is incorrect as the pressure applied on the fluid domain gives a wrong apparent dependence in the porosity for the coefficient c, and also necessarily for a and b. However, Burcharth & Andersen (1995) [4], pointed this error out but use the derived formulation anyway. They justify it by stating that a "*dimensionless factor, like n, can be applied to the parameters without violating the dimensional analysis. It will still give combined parameters which in a mathematical sense are correct, but not necessarily physically the most relevant or meaningful. It is difficult from theory to verify which is the best formulation of the factor b with respect to the dependency on the porosity*". That is why they kept the experimental formulation done by Ergün (1952) where the variation with the porosity conforms to the coefficients re-expressed by Van Gent (1993).

$\alpha$ and $\beta$ are empirical coefficients which can be called tortuosity coefficients. They still depend on many different types of parameters (Van Gent 1993 [59] and Burcharth & Andersen 1995 [4]) such as :

- Flow parameters : Reynolds number $R_e$ (defined in equation (4.18)), Keulegan Carpenter number $KC$ (defined in equation (4.16)), and steady or non-steady flow.
- Stone parameters : grading, aspect ratio, shape and orientation

Hannoura & McCorquodale (1978) [20], Smith (1991) [49], Burcharth & Christensen (1991) [5], and Van Gent (1993, 1995) [59] & [60] performed a limited set of experiments using U-tube water tunnels for different stone and sphere sizes. The flow is oscillating, which is closer to a flow generated by waves, except that there are only horizontal velocities. One of the most important aspects from the Van Gent parametrisation for the a, b, and c parameters is the dependence to the Keulegan-Carpentar number (KC) in the non-linear drag term. $KC$ is defined as :

$$KC = \frac{\hat{v_p} T}{d_{n50}} \tag{4.16}$$

with $\hat{v_p} = n\hat{v_d}$ the maximal pore oscillating velocity and $T$ the period of the oscillating flow. We can rewrite the expression of the pressure gradient due to friction $av_d + bv_d^2$ as :

$$\begin{aligned} av_d + bv_d^2 &= \alpha \frac{(1-n)^2}{n^3} \frac{\nu}{g d_{n50}^2} v_d + \beta \left(1 + \frac{7.5}{KC}\right) \frac{1-n}{n} \frac{1}{g d_{n50}} v_d^2 \\ &= \alpha \frac{(1-n)^2}{n^3} \frac{\nu}{g d_{n50}^2} v_d + \beta \frac{7.5 n d_{n50}}{\hat{v_d} T} \frac{1-n}{n^3} \frac{1}{g d_{n50}} v_d^2 + \beta \frac{1-n}{n} \frac{1}{g d_{n50}} v_d^2 \\ &= \left(\alpha + \frac{7.5\delta n}{1-n} \beta_S\right) \frac{(1-n)^2}{n^3} \frac{\nu}{g d_{n50}^2} v_d + \beta \frac{1-n}{n} \frac{1}{g d_{n50}} v_d^2 \\ &= a' v_d + b' v_d^2 \end{aligned} \tag{4.17}$$

where :

- $\beta_S$ is the Stokes parameter defined in equation (4.22).
- $\delta = \frac{v_d}{\hat{v_d}}$. $\delta$ can be considered constant as it is the relation between the maximal and the average elliptic velocities.

The expression of $b$ proposed by Van Gent (1995) results in an increase in the $\alpha$ coefficient with the parameter $\beta_S$.

It is found that the non-linear drag term has relatively small variations in b coefficient values. A numerical study is performed by B. Jensen et al. (2014) [25] to analyse the variation of coefficients $\alpha$ and $\beta$ in cases where an initial volume of water is released to a porous damn. The formulation of Van Gent (1993) [59] is used. They conclude that $\alpha = 500$ and $\beta = 2$ would be the best pair of values for the different turbulent flow regimes described by Burcharth & Andersen (1995) [4], see section 1.4.4.3 *Criterion for non-Darcy flow*.

It should be noted that the tests with U-tube water tunnels are conducted with no free surface and the numerical study previously mentioned does not integrate oscillatory flows. These results have thus to be used with caution. As Losada et al. (2016) [38] said, the problem remains open and work is required in modelling flow inside porous media using averaging methods.

## 4.3 Criterion for non-Darcy flow

Flow can be categorized into several specific regimes within a physical phenomenon dominates the others. The parameters a and b will differ in importance depending on the flow regime. The appreciation of a flow regime is especially important given that we often work with scaled models. Two criteria have been developed in the literature, the Reynolds number criterion and the Forchheimer number criterion (Zeng & Grigg (2006) [67]).

### 4.3.1 Reynolds number criterion

The Reynolds number inside a porous medium is derived from the Reynolds number for identifying turbulent flow. The pores of a porous medium are modelled as cylinders like in the averaging of the Navier-Stokes equation. The Reynolds number is defined as :

$$R_e = \frac{vd}{\nu} \tag{4.18}$$

where $d$ is a characteristic length of the porous media and $v$ a characteristic velocity. In this work, we consider $d = d_{n50}$ and $v = \hat{v_p}$ the maximum pore velocity.

According to Zeng & Grigg review (2006) [67], critical values for non-Darcy flow vary from 1 to 100 for the Reynolds number criterion. This is mainly applied for columns of packed particles when the characteristics length, usually the representative particle diameter, is available.

We find similar values amongst the specific studies in the coastal engineering field. Van Gent (1995) [60], taking the results of Gu & Wang (1991) [19] use a characteristic particle size of the porous material $d$ and the maximum pore velocity $\hat{v_p}$ to defined the Reynolds number. Gu & Wang (1991) respectively find the values 10 and 1000 to delimit laminar flow regime ($R_e < 10$), transitional flow regime ($10 < R_e < 1000$) and turbulence flow regime ($R_e > 1000$).

Burcharth & Andersen (1995) [4] follow the conclusion of Burcharth & Cristensen (1991). They mention 5 different flow regimes which are depicted in the figure 4.2. The laminar (Darcy) flow regime is defined for $R_e < 1$. There is a transition zone for $1 < R_e < 10$ where a boundary layer appears around the grains. For $10 < R_e < 150$, the flow resistance becomes partly non-linear. This regime is referred as the Forchheimer flow regime. There is a new transition zone from $R_e = 150$ to 300 where the flow becomes turbulent. For $R_e > 300$, the resistance drag term is exclusively quadratic.

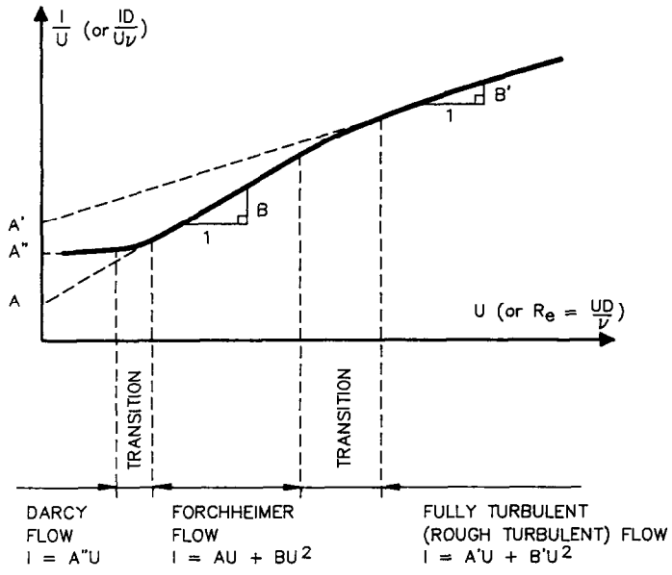


Figure 4.2: Conventional representation of flow regimes for porous flow based on a Forchheimer equation analysis, Burcharth & Cristensen (1991) [5]

### 4.3.2 Forchheimer number criterion

For its part, the Forchheimer number is defined as the relation between the turbulence drag term and the laminar drag term. It was firstly defined with the intrinsic permeability $K$ and a new non-Darcy flow coefficient $\beta_o$ as :

$$F_o = \frac{\text{turbulent resistance}}{\text{laminar resistance}} = \frac{K\beta_o v}{\nu} \tag{4.19}$$

If we rewrite the Forchheimer number with the coefficients expressed by Burcharth & Andersen (1995) [4], we obtain :

$$F_o = \frac{b\hat{v_p}^2}{a\hat{v_p}} = \frac{\beta d\hat{v_p}}{\alpha(1-n)\nu} = \frac{\beta R_e}{\alpha(1-n)} \sim 10^{-4}R_e \text{ to } 10^{-2}R_e \tag{4.20}$$

where $\alpha$ = O(1000) and $\beta$ = O(1) inside porous breakwaters.

Zeng & Grigg (2006) [67] give values from the literature where non-Darcy flow regime vary from $F_o = 0.005$ to $F_o = 0.2$. For Burcharth & Andersen (1995) [4], the fully turbulent regime starts from $F_o = 5$ for $R_e = 300$. With the coefficients $\alpha = 500$ and $\beta = 2$ proposed by B. Jensen et al. (2014) [25] and with a mean porosity $n = 0.4$, we obtain $F_o = 2$. The quadratic resistance is twice as important than the laminar resistance. Now, if we take the coefficients $\alpha = 2950$ and $\beta = 0.3$ found from sloshing experimental tests presented in chapter 3.2, they lead to $F_o = 0.05$. This time, the laminar resistance is much bigger than the quadratic resistance. Numerically, the nature of the flow at a given Reynolds number depends a lot on the tortuosity coefficients.

The Forchheimer number criterion has been used mainly in numerical models. Nevertheless, in the laboratory, the Reynolds number is more easily computable. The limit of the different flow regimes defined by Burcharth & Andersen (1995) [4] depends thus on the tortuosity coefficients of the porous medium used for the tests.

## 4.4 Relative importance of the inertia term

Another non-dimensional number was designed in order to appreciate the relative importance of the inertia term, the Keulegan-Carpenter number $KC$, which estimates the magnitude of the resistance term due to turbulence in regards to the inertial resistance. It is defined as :

$$KC = \frac{\text{turbulent resistance}}{\text{inertial resistance}} = \frac{\hat{v_p}T}{d_{n50}} \tag{4.21}$$

The relative importance of the inertial resistance compared to the laminar resistance can thus be estimated by the Stokes parameter $\beta_S$ :

$$\beta_S = \frac{\text{inertial resistance}}{\text{laminar resistance}} = \frac{R_e}{KC} = \frac{d_{n50}^2}{\nu T} \tag{4.22}$$

Gu & Wang (1991) [19] estimated the importance of the different resistance terms for different coarse materials, in different flows cases, see figure 4.3.

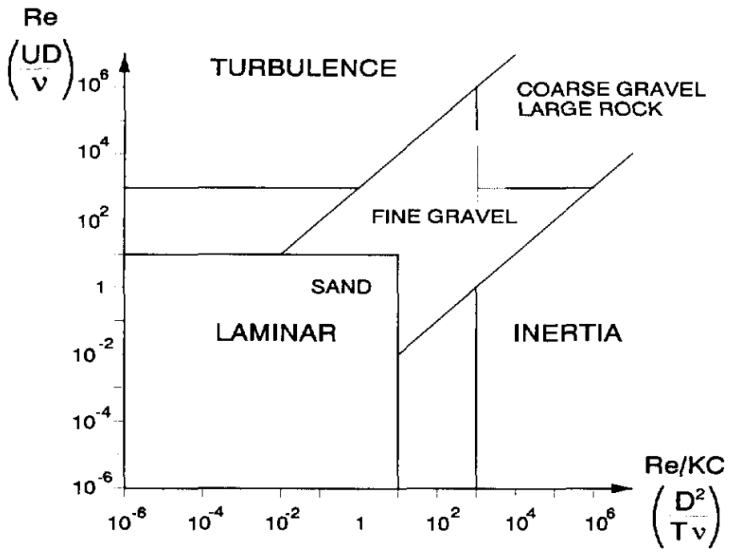


Figure 4.3: Flow regions with predominant resistance terms, Gu & Wang (1991) [19]

The tests with U-tube water tunnels performed by Smith (1991) [49] and Van Gent (1993, 1995) [59] & [60] were located in regions *Fine gravel* and *Large rock* where the effects of both turbulence and inertial resistances play an important role.

# 5 ANALYSING METHOD

Usually, new configurations of damping structures are tested numerically or experimentally. For a 2D case, the typical setup is given in figure 5.1. To characterise the hydrodynamic performance, the reflected and the transmitted wave fields need to be measured.

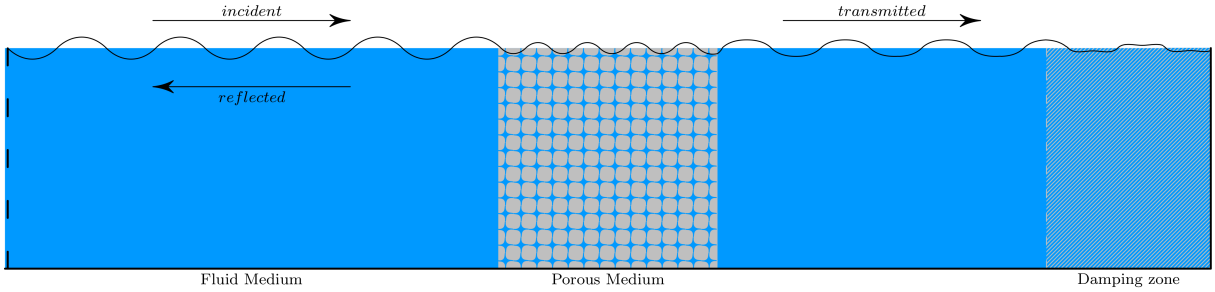


Figure 5.1: Reflected-Transmitted waves, Analysing Method

The signal of the free surface is acquired by several conductive or capacitive probes upstream and downstream from the scale-model. The incident and the reflective waves with their higher harmonics are then decomposed by data processing methods. The technique used later in this work is the one from Andersen & al. (2017) [39] which is an extension of the Lin & Huang method (2004) [36]. The incident and reflective waves may be highly non-linear regular waves due to shallow water or interaction between waves and structures.

Lin & Huang (2004) method was already an extension of the method by Mansard & Funke (1980) [41]. The latter separate the complex waves into individual frequency components using the Fourier transform, as already done by Goda & Suzuki (1976) [18]. They then use a least square method in order to reduce the error caused by the noise signal. That's why four or more spatially spaced probes are required. The probes have to respect some spacing conditions to prevent singularities. Contrary to the method of Mansard & Funke (1980), the one of Lin & Huang (2004) enables it to catch the full modes on a regular wave field, including free and bound waves in the higher harmonics. The separation in bound and free harmonics is very relevant when analysing model tests.

**Lin-Huang method**

The mathematical model of the surface for $N^{th}$ order waves as function of time (t) and coordinate of gauge number m ($x_m$) measured positive in the incident wave direction is taken as :

$$\begin{aligned}\eta(x_m,t) = {} & a_I^{(1)}\cos\left(kx_m-\omega t+\phi_I^{(1)}\right)+a_R^{(1)}\cos\left(kx_m+\omega t+\phi_R^{(1)}\right)\\ & +\sum_{n\geq 2}a_{I,B}^{(n)}\cos\left[n(kx_m-\omega t)+\phi_{I,B}^{(n)}\right]+\sum_{n\geq 2}a_{R,B}^{(n)}\cos\left[n(kx_m+\omega t)+\phi_{R,B}^{(n)}\right]\\ & +\sum_{n\geq 2}a_{I,F}^{(n)}\cos\left[n(k^{(n)}x_m-n\omega t)+\phi_{I,F}^{(n)}\right]+\sum_{n\geq 2}a_{R,F}^{(n)}\cos\left[n(k^{(n)}x_m+n\omega t)+\phi_{R,F}^{(n)}\right]\\ & +e_m(t)\end{aligned} \tag{5.1}$$

where $e_m(t)$ is the noise. Subscripts $I$ and $R$ represent incident and reflected components, receptively. Subscripts $B$ and $F$ denote bound and free components. $a$ is the amplitude, $k$ the wave number, $\omega$ the pulsation and $\phi$ the phase, of the primary component. Exponent $n$ denotes the $n^{th}$ order component. These are determined by linear dispersion :

$$(n\omega)^2 = g\,k^{(n)} \tanh(k^{(n)} h) \tag{5.2}$$

with $g$ the gravity acceleration and h the water depth.

As Andersen et al. (2017) [39] explain, "*the primary component k appears to be based on linear dispersion too, equation* (5.2) *with* $n = 1$. *The linear dispersion is only valid to* $2^{nd}$ *order so Lin & Huang [36] indirectly have assumed mildly non-linear waves (*$2^{nd}$ *order theory valid)*".

The complete procedure of this method is exposed in Lin & Huang (2004) [36]. The Andersen et al. [39] method is more deeply developed. Finally, the reflection coefficient is defined by :

$$K_r = \sqrt{\frac{(a_R^{(1)})^2 + \sum_{n\geq 2}\left[(a_{R,B}^{(n)})^2 + (a_{R,F}^{(n)})^2\right]}{(a_I^{(1)})^2 + \sum_{n\geq 2}\left[(a_{I,B}^{(n)})^2 + (a_{I,F}^{(n)})^2\right]}} \tag{5.3}$$

The transmission coefficient is expressed in the same way as the ratio of the transmitted and incident wave amplitude.

**Andersen & al. method**

The most advanced separation method proposed by Andersen et al. (2017) [39] overcomes the limitation of Lin & Huang (2004) method [36] to treat highly non-linear waves by replacing the linear dispersion formulation by a non-linear one in order to take into account the amplitude dispersive effect of non-linear waves ($3^{rd}$ and higher order). Moreover, a problematic region where bound and free components have identical celerity is identified and a correction is suggested.

Following Andersen et al., the wave numbers of the primary component (and bound components) depends additionally on the wave height ($H$) and will be different for incident and reflected waves. The wave period to be applied in the dispersion relation is usually known beforehand. It can also be estimated based on the signals for example by zero down crossing analysis or from the frequency of the first Fourier coefficient with significant energy. However, the incident and reflected wave height needed for the non-linear dispersion relation is part of the solution and is thus unknown to begin with. Therefore, an iterative procedure (fully described in [39]) is used for the wave length estimation.

The applied mathematical model is thus :

$$\begin{aligned}\eta(x_m,t) = {} & a_I^{(1)}\cos\left(k_I x_m - \omega t + \phi_I^{(1)}\right) + a_R^{(1)}\cos\left(k_R x_m + \omega t + \phi_R^{(1)}\right) \\ & + \sum_{n\geq 2} a_{I,B}^{(n)}\cos\left[n(k_I x_m - \omega t) + \phi_{I,B}^{(n)}\right] + \sum_{n\geq 2} a_{R,B}^{(n)}\cos\left[n(k_R x_m + \omega t) + \phi_{R,B}^{(n)}\right] \\ & + \sum_{n\geq 2} a_{I,F}^{(n)}\cos\left[n(k^{(n)} x_m - n\omega t) + \phi_{I,F}^{(n)}\right] + \sum_{n\geq 2} a_{R,F}^{(n)}\cos\left[n(k^{(n)} x_m + n\omega t) + \phi_{R,F}^{(n)}\right] \\ & + e_m(t)\end{aligned} \tag{5.4}$$

The only difference with equation (5.1) is the wave numbers used for the incident and reflected bound waves ($k_I$ and $k_R$). Non-linear dispersion applied is Stokes V order theory when it is valid (deep water). If Stokes V is not valid, the wave number is calculated by stream function theory.

Equation (5.4) can then be written up in the frequency domain. For primary component ($n = 1$), the following is obtained :

$$
\begin{aligned}
\hat{\eta}^{(1)}(x_m) &= C_I^{(1)} X_I^{(1)} + C_R^{(1)} X_R^{(1)} + \Omega_m^{(1)} \\
X_I^{(1)} &= a_I^{(1)} \exp\left[-i(k_I x_1 + \phi_I^{(1)})\right] \\
X_R^{(1)} &= a_R^{(1)} \exp\left[i(k_R x_1 + \phi_R^{(1)})\right] \\
C_I^{(1)} &= \exp(-i k_I \Delta x_m) \\
C_R^{(1)} &= \exp(i k_R \Delta x_m)
\end{aligned}
\tag{5.5}
$$

where $\Delta x_m = x_m - x - 1$ and $\Omega_m^{(1)}$ is the Fourier transformation of $e_m(t)$ at frequency $\omega$. For higher harmonics ($n > 1$) the Fourier transformation at frequency $n\omega$ gives :

$$
\begin{aligned}
\hat{\eta}^{(n)}(x_m) &= C_{I,B}^{(n)} X_{I,B}^{(n)} + C_{R,B}^{(n)} X_{R,B}^{(n)} + C_{I,F}^{(n)} X_{I,F}(n) + C_{R,F}^{(n)} X_R^{(n)} + \Omega_m^{(n)} \\
X_{I,B}^{(n)} &= a_{I,B}^{(n)} \exp\left[-i(n k_I x_1 + \phi_{I,B}^{(n)})\right] \\
X_{R,B}^{(n)} &= a_{R,B}^{(n)} \exp\left[i(n k_R x_1 + \phi_{R,B}^{(n)})\right] \\
X_{I,F}^{(n)} &= a_{I,F}^{(n)} \exp\left[-i(k^{(n)} x_1 + \phi_{I,F}^{(n)})\right] \\
X_{R,F}^{(n)} &= a_{R,F}^{(n)} \exp\left[i(k^{(n)} x_1 + \phi_{R,F}^{(n)})\right] \\
C_{I,B}^{(n)} &= \exp(-i n k_I \Delta x_m) \\
C_{R,B}^{(n)} &= \exp(i n k_R \Delta x_m) \\
C_{I,F}^{(n)} &= \exp(-i k^{(n)} \Delta x_m) \\
C_{R,F}^{(n)} &= \exp(i k^{(n)} \Delta x_m)
\end{aligned}
\tag{5.6}
$$

where $\Omega_m^{(n)}$ is the Fourier transformation of $e_m(t)$ at frequency $n\omega$.

The values of the complex parameters $X_I^{(1)}$, $X_R^{(1)}$, $X_{I,B}^{(n)}$, $X_{R,B}^{(n)}$, $X_{I,F}^{(n)}$ and $X_{R,F}^{(n)}$ are determined by fitting the equation to the measurement by minimising of the noise term $\Omega_m^{(n)}$.

The correction applied when bound and free super-harmonics have almost identical celerity is not developed here. It can be found in Andersen et al. (2017) [39]. The coefficients of reflection and transmission are defined in the same way as for Lin & Huang (2004) method [36] in equation (5.3).

PART 2

# ANALYTICAL AND NUMERICAL MODELS

In this part, we present the three different models used in this work to simulate the interaction of waves with porous breakwaters. First, the equations of a flow through a porous medium based on linear wave theory are presented. These equations are the ones coded in the developed diffraction code *Diffra3D* described in the second part. Another numerical code based on the VOF method will be used to compare the results and catch sight of non-linear effects that the first code can not reproduce. Finally, a simple analytical model based on long wave theory will be presented and used. The models are based on *different wave theories* but with the *same theory* to model porous media.

# 1 SOLUTION BASED ON LINEAR WAVE THEORY

The solution based on linear wave theory to solve flow inside porous structures using the extended Forchheimer equation were historically first derived in literature by Sollitt & Cross (1972) [50]. The solution was applied to the analysis of wave motion through a rectangular mound in 2D wave tank. This theory was then used by other authors. Sulisz (1985) [52] studied the Wave reflection and transmission at permeable breakwaters of arbitrary cross-section. Dalrymphe & al. (1991) [12] studied the behaviour of porous structures under oblique waves and Yu and Chwang (1994) [66] studied the phenomena of wave-induced oscillations in harbours with porous breakwaters.

The numerical tool developed in this work implements this theory. The model is also designed, amongst other factors, to integrate a new concept in the boundary conditions between two continuous media : the surface porosity concept which is different from the traditional volume porosity concept.

The pressure drop through a porous wall is also derived following Lajoie & Bougis (2008-2014) [33] & [34] and from experimental tests performed by Molin & Remy (2015) [44].

## 1.1 Equation of flow through a porous medium

Consider a closed volume strictly including a homogenised porous medium. For this volume, the conservation of momentum is applied :

$$\iiint_{\Sigma}\left(\frac{\partial \vec{v}_d}{\partial t}+\frac{1}{n}(\vec{v}_d.\overrightarrow{\nabla})\vec{v}_d\right)\mathrm{d}V=-\frac{1}{\rho}\iint_{\partial\Sigma}p\,\overrightarrow{\mathrm{d}S}+\iiint_{\Sigma}\left(\vec{g}+\vec{f}_r\right)\mathrm{d}V \tag{1.1}$$

where $\Sigma$ is the closed volume, $\partial\Sigma$ the exterior surface, $\vec{v}_d$ the filter velocity and $\vec{f}_r$ are volumetric resistant forces. As noticed in chapter 1.4, for a non-steady flow in a porous medium, volumetric resistant forces may be modelled by the extended Forchheimer equation :

$$\frac{1}{\rho g}\vec{f}_r=-\left[a\vec{v}_d+b\|\vec{v}_d\|\vec{v}_d+c\frac{\partial \vec{v}_d}{\partial t}\right] \tag{1.2}$$

The equation (1.1), averaged at the macroscopic scale, becomes :

$$S\frac{\partial \vec{v}_d}{\partial t}+\frac{1}{2n}\overrightarrow{\nabla}\,\vec{v}_d{}^2=-\frac{1}{\rho}\overrightarrow{\nabla}\,p-g\vec{z}-\frac{\nu}{K}\vec{v}_d-\frac{C_f}{\sqrt{K}}|\vec{v}_d|\vec{v}_d \tag{1.3}$$

with $S=1+C_M\frac{1}{1-n}$, and to remind that $K=\frac{n^3d_{n50}^2}{\alpha(1-n)^2}$ and $C_f=\frac{\beta}{\sqrt{\alpha}}n^{-\frac{3}{2}}$.

Equation (1.3) is linearised. The convective term $\frac{1}{2n}\overrightarrow{\nabla}\,\vec{v}_d{}^2$ is small compared to $\frac{\partial \vec{v}_d}{\partial t}$ and can be discarded. Then, using the Lorentz procedure and by introducing a dimensionless dissipation coefficient f such that it yields :

$$f\omega = \frac{\nu}{K} + \frac{C_f}{\sqrt{K}}\overline{f} \tag{1.4}$$

with :

$$\overline{f} = \frac{\int_0^T |\vec{v}_d|^3 \,\mathrm{d}t}{\int_0^T |\vec{v}_d|^2 \,\mathrm{d}t} = \frac{8}{3\pi}\sqrt{a+b}\left[E(m) - \frac{1}{4}\left(1-\frac{a}{b}\right)K(m)\right] \tag{1.5}$$

where $a = \frac{1}{T}\int_0^T |\vec{v}_d|^2 \,\mathrm{d}t$, $b = max_{t\in[0,T]}\,[|\vec{v}_d| - a]$ and $m = \frac{2b}{a+b}$. $K(m)$ and $E(m)$ represent respectively the elliptic integrals of first and second kinds.

The equation (1.3) becomes :

$$S\frac{\partial \vec{v}_d}{\partial t} = -\frac{1}{\rho}\vec{\nabla}\, p - g\vec{z} - f\omega\vec{v}_d \tag{1.6}$$

In a pure fluid domain, we would have $S = 1$ and $f = 0$.

The flow in the fluid medium external to the porous medium is assumed to be irrotational with a velocity potential $\Phi_{d1}$. The flow inside the porous medium, which is assumed a continuous domain, is also considered irrotational and a velocity potential $\Phi_{d2}$ is also introduced (see figure 1.1).

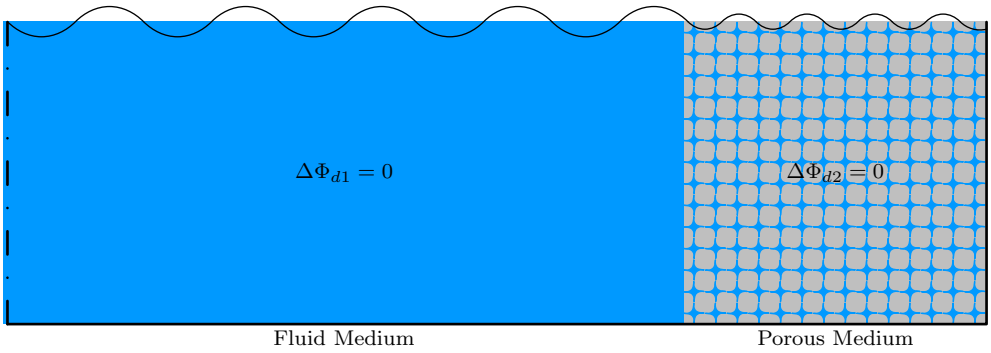


Figure 1.1: Geometry, Flow inside porous medium

By introducing the potential of velocity $\Phi_d$, it yields :

$$S\frac{\partial \Phi_d}{\partial t} + \frac{p}{\rho} + gz + f\omega\Phi_d = 0 \tag{1.7}$$

with $\Phi_d$ equal to $\Phi_{d1}$ or $\Phi_{d2}$.

We suppose $\Phi_d = \phi_d e^{-i\omega t}$ according to the hypothesis of monochromatic waves. Using this expression for the potential, the previous equation becomes :

$$(f - iS)\omega\phi_d + \frac{p}{\rho} + gz = 0 \tag{1.8}$$

### 1.1.1 The free surface condition

The free surface condition of a continuous medium must respect the dynamic and kinematic conditions.

The dynamic free surface condition reflects the equal pressure at the free surface. It is obtained from equation (1.8) by putting $p = 0$ in $z = \eta$ :

$$(f - iS)\omega\phi_d + g\eta = 0\big|_{z=\eta} \tag{1.9}$$

The kinematic condition of free surface reflects the mass conservation :

$$n\frac{d\eta}{dt} = \left.\frac{dz_{particle}}{dt}\right|_{z=\eta} \tag{1.10}$$

where $n$ is the volume porosity.

The concept of **surface porosity** in porous media as opposed to volume porosity is introduced and defined by $\mu = 1-(1-n)^{\frac{2}{3}}$. Equation (1.10) in projection on the cartesian axes yields :

$$n\frac{\partial\eta}{\partial t} + (\vec{\nabla}\,\phi_d.\,\vec{\nabla})\eta = \left.\frac{\mu}{n}\frac{\partial\phi_d}{\partial z}\right|_{z=\eta} \tag{1.11}$$

After linearisation around $z = 0$ and with the hypothesis of harmonic response, the kinematic condition is given by :

$$-i\omega\eta = \left.\frac{\mu}{n^2}\frac{\partial\phi_d}{\partial z}\right|_{z=0} \tag{1.12}$$

By combining the two boundary conditions, we find the linear free surface condition in a porous medium :

$$\left.\frac{\partial\phi_d}{\partial z} - (S+if)\frac{\omega^2}{g}\frac{n^2}{\mu}\phi_d = 0\right|_{z=0} \tag{1.13}$$

**The interface between two continuous media**

The interface between two continuous media must respect the conservation of flow and the continuity of pressures, namely :

Conservation of the flow
$$\left.\frac{\mu_1}{n_1}\frac{\partial\phi_{d1}}{\partial n} = -\frac{\mu_2}{n_2}\frac{\partial\phi_{d2}}{\partial n}\right|_{at\ the\ interface} \tag{1.14}$$

Pressure conservation
$$(S_1+if_1)\phi_{d1} = (S2+if_2)\phi_{d2}\big|_{at\ the\ interface} \tag{1.15}$$

**The elevation of the free surface**

The elevation of the free surface is expressed by :

$$\eta = \frac{\omega}{g}(iS-f)\phi_d \tag{1.16}$$

## 1.2 Porous Wall

The penetration of flow through a porous wall is treated in a different manner than for a porous medium. The linear potential theory is considered, except for the dissipation zones caused by the holes of the porous wall.

The pressure gradient on both sides of the wall can thus be expressed after integrating the Bernoulli-Lagrange equation all along a stream line passing through a hole, see Lajoie & Bougis (2014) [34]. The terms of the equation (1.17) correspond respectively to singular and linear pressure losses. The added mass effects mentioned by Molin (2014) [43] when the number of slots becomes smaller with constant porosity can also be included in the second term.

$$\Delta p = \frac{1}{2}\rho K_p|v_{dn}|v_{dn} + \int_{a_l}\frac{\rho(1-\tau)}{\tau k_c}\frac{\partial\vec{v_{dn}}}{\partial t}\,\mathrm{d}\vec{l} \tag{1.17}$$

where :

- $v_{dn}$ is the normal filter velocity upstream or downstream from the wall. The crossing velocity can thus be written as $v_{cdn} = \frac{v_{dn}}{\tau k_c}$.
- $\tau$ is the wall's porosity.
- $k_c$ is a coefficient of flow restriction due to the passage of the flow through a hole. Usually, $k_c$ value is taken to 0.8 for a slot and 0.65 for a circular hole. In fact, $k_c$ also depends on the nature of the flow, hence on $R_e$.
- $K_p$ is a coefficient of pressure loss. An expression can be given by $K_p = \frac{1-\tau}{\tau^2 k_c^2}$.
- $a_l = l + l_m$. $l$ is the wall's width and $l_m$ is a small term corresponding to the added mass effects[1].

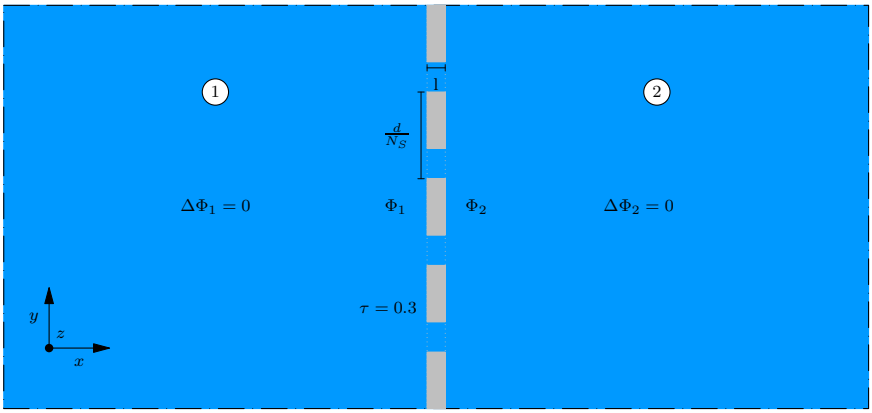


Figure 1.2: Geometry, normals are outwards facing for each domain

The porous wall (Fig. 1.2) is idealised as a continuous porous boundary. With the velocity potential written as :

$$\Phi_d(x,y,z,t) = \Re\{\phi_d(x,y,z)\,\mathrm{e}^{-i\omega t}\} \tag{1.18}$$

The pressure gradient relation at the porous wall, with the shorter notation $\epsilon = S + if$ can be expressed, as :

$$i\omega\rho(\epsilon_1\phi_{d1} - \epsilon_2\phi_2) = \frac{1}{2}\rho K\frac{8}{3\pi}\left|\frac{\mu_1}{n_1}\frac{\partial\phi_{d1}}{\partial n}\right|\frac{\mu_1}{n_1}\frac{\partial\phi_{d1}}{\partial n} - i\omega\frac{\rho a_l(1-\tau)}{\tau k_c}\frac{\mu_1}{n_1}\frac{\partial\phi_{d1}}{\partial n} \tag{1.19}$$

It yields :

$$\frac{\partial\phi_{d1}}{\partial n} = \frac{\epsilon_1\phi_{d1} - \epsilon_2\phi_{d2}}{-i\frac{4K}{3\pi\omega}\frac{\mu_1^2}{n_1^2}|\frac{\partial\phi_{d1}}{\partial n}| - \frac{a_l(1-\tau)}{\tau k_c}\frac{\mu_1}{n_1}} \tag{1.20}$$

By taking the absolute value and taking the square, we get a second degree equation with $\left|\frac{\partial\phi_{d1}}{\partial n}\right|^2$ as unknown :

$$\left(\frac{4K}{3\pi\omega}\frac{\mu_1^2}{n_1^2}\right)^2\left|\frac{\partial\phi_1}{\partial n}\right|^4 + \frac{a_l^2(1-\tau)^2}{\tau^2 k_c^2}\frac{\mu_1^2}{n_1^2}\left|\frac{\partial\phi_{d1}}{\partial n}\right|^2 - |\epsilon_1\phi_{d1} - \epsilon_2\phi_{d2}|^2 = 0 \tag{1.21}$$

The solution is given by :

[1] According to Molin & Remy (2015) [44], the added mass coefficients depending on the type of holes are :
- Slot openings : $l_m = \tau k_c(1-\tau)\pi C_a(\tau)\frac{d}{4N_S}$ with $N_S$ the number of slots over the width $d$ of the wall.
- Circular openings : $l_m = \frac{k_c\sqrt{\tau}C_a(\tau)a}{\pi(1-\tau)}$ with $a$ the radius of a hole.
- $C_a(\tau) = -\frac{8}{(1-\tau)^2\pi^2}\ln\left(\sin(\frac{\pi\tau}{2})\right)$

$$\left|\frac{\partial \phi_{d1}}{\partial n}\right|^2 = \frac{-(\frac{a_l(1-\tau)}{\tau k_c}\frac{\mu_1}{n_1})^2 + \sqrt{(\frac{a_l(1-\tau)}{\tau k_c}\frac{\mu_1}{n_1})^4 + 4(\frac{4K}{3\pi\omega}\frac{\mu_1^2}{n_1^2})^2|\epsilon_1\phi_{d1} - \epsilon_2\phi_{d2}|^2}}{2(\frac{4K}{3\pi\omega}\frac{\mu_1^2}{n_1^2})^2} \tag{1.22}$$

This equation first proposed by Lajoie (2008) [33] gives a relation between $\frac{\partial \phi_{d1}}{\partial n}$ and $\phi_{d1}$ :

$$\frac{\partial \phi_{d1}}{\partial n} = \frac{\epsilon_2 \phi_{d2} - \epsilon_1 \phi_{d1}}{\frac{a_l(1-\tau)}{\tau k_c}\frac{\mu_1}{n_1} + \frac{i}{\sqrt{2}}\sqrt{-(\frac{a_l(1-\tau)}{\tau k_c}\frac{\mu_1}{n_1})^2 + \sqrt{(\frac{a_l(1-\tau)}{\tau k_c}\frac{\mu_1}{n_1})^4 + 4(\frac{4K}{3\pi\omega}\frac{\mu_1^2}{n_1^2})^2|\epsilon_2\phi_{d2} - \epsilon_1\phi_{d1}|^2}}} \tag{1.23}$$

# 2 DIFFRACTION NUMERICAL MODEL

A 3D diffraction numerical tool, integrating porous media and porous plates, was developed from scratch in the object-oriented programming language Python. Even if Python is an interpreted language that makes it slower than compiled languages such as C++ or Fortran, the language has the advantage to use pre-compiled C functions that allow fast computations. Furthermore, Python is a very user-friendly code and python-code is easy to maintain. A lot of optimisations can still be made to support bigger meshes and to make the code faster, mainly for the computation of the influence coefficients and for the creation of the main matrix to inverse.

The implemented equations for every modelled media are linear but an iteration on the filter velocities $v_{di}$ for every medium is necessary to solve the global problem. The following paragraphs present the main equations of a diffraction numerical model with Rankine integrals. The basic equations of the BEM method for diffraction problems are derived in G. Delhommeau (1987) [15].

## 2.1 Theoretical background

The geometry of a 3D diffraction problem is sketched in the figure 2.1 with the following boundaries :

- FS is the free surface.
- Σ represents a structure boundary.
- I represents an interface with another domain fluid or porous, and can modelled a porous plate.
- G is the ground.
- C is the control boundary with conditions of inlet and outlet boundaries.

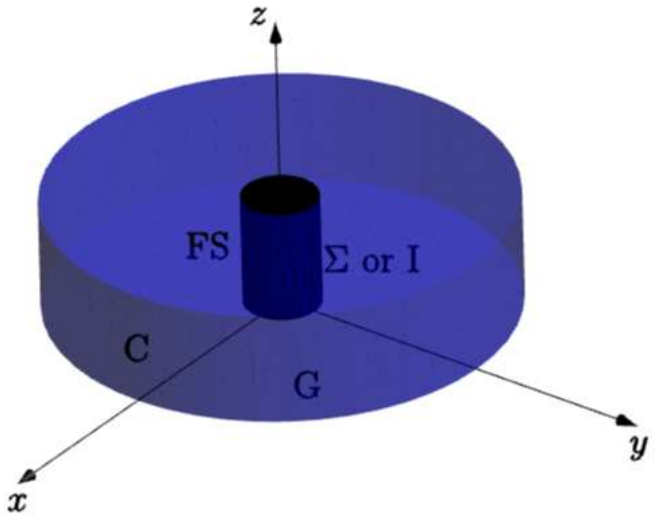


Figure 2.1: Geometry, Diffraction model

The third Green Formula is expressed as :

$$\left.\begin{array}{lcl} \forall M \in D \backslash \partial D & : & 1 \\ \forall M \in \partial D & : & \frac{1}{2} \\ \forall M \notin D & : & 0 \end{array}\right\} \Phi(M) = \oiint_{\partial D} \Phi(M') \frac{\partial G_M(M')}{\partial n(M')} \mathrm{d}S(M') - \oiint_{\partial D} \frac{\partial \Phi(M')}{\partial n(M')} G_M(M') \mathrm{d}S(M') \tag{2.1}$$

with $G_M(M') = -\frac{1}{4\pi} \frac{1}{|MM'|}$ and $\vec{n}$ : normal pointing outside of domain D.

Every potential can be expressed by a distribution of sources $\sigma = -\frac{\partial \Phi}{\partial n}$ and normal dipoles $\chi = \Phi$ on $\partial D$.

The structure is assumed fixed. Potential $\Phi$ on the border meet the following characteristics :

- $\Delta \Phi = 0$
- $\left.\frac{\partial \Phi}{\partial n}\right|_F = 0$
- $\left.\frac{\partial \Phi}{\partial n} - (S + if) \frac{\omega^2}{g} \frac{\mu}{n^2} \Phi\right|_{FS} = 0$
- $\left.\frac{\partial \Phi}{\partial n}\right|_\Sigma = 0$

On the control cylinder, the potential $\Phi$ is decomposed in the form of :

$$\forall M \in \partial D, \Phi(M) = \Phi_I(M) + \Phi_D(M) \tag{2.2}$$

with :

- $\Phi_I$ the incident potential, known on the control cylinder.
- $\Phi_D$ the diffraction potential, checking the condition of equation (2.3).

In our case, the control cylinder is placed far enough from the structure (at a distance of $R$) to neglect the the near field. We keep the first order of local conditions on the far field (Lajoie (1996) [32]) :

$$\left.\frac{\partial \Phi_D}{\partial n}\right|_C = \alpha \Phi_D \quad \text{with } \alpha = \left(-\frac{1}{2R} + ik\right) \tag{2.3}$$

Now, the diffraction problem can be expressed in this way :

$$\begin{aligned} -\frac{1}{2}\Phi(M) &+ \iint_{FS} \Phi(M') \left[\frac{\partial G_M(M')}{\partial n(M')} - (S + if)\frac{\omega^2}{g}\frac{\mu}{n^2} G_M(M')\right] \mathrm{d}S(M') \\ &+ \iint_{C} \Phi(M') \left[\frac{\partial G_M(M')}{\partial n(M')} - \alpha(M') G_M(M')\right] \mathrm{d}S(M') \\ &+ \iint_{G+I+\Sigma} \Phi(M') \frac{\partial G_M(M')}{\partial n(M')} \mathrm{d}S(M') - \iint_{I} \frac{\partial \Phi(M')}{\partial n(M')} G_M(M') \mathrm{d}S(M') \\ &= \iint_{G+\Sigma} \frac{\partial \Phi(M')}{\partial n(M')} G_M(M') \mathrm{d}S(M') \\ &+ \iint_{C} \left[\frac{\partial \Phi_I(M')}{\partial n(M')} - \alpha(M') \Phi_I(M')\right] G_M(M') \mathrm{d}S(M') \end{aligned} \tag{2.4}$$

The previous equation 2.4 is discretisated, $S_{ij}$ and $D_{ij}$ are the influence coefficients of sources and normal dipoles of panel i in relation to panel j. They are computed in every point $M_i$, center of gravity of every panel $i$.

$$S_{ij} = \sum_j G_{M_i}(M_j) S(M_j) \tag{2.5}$$

$$D_{ij} = \sum_j \frac{\partial G_{M_i}(M_j)}{\partial n(M_j)} S(M_j) \tag{2.6}$$

By introducing the source $\sigma_i$ and the normal dipole $\chi_i$ on every panel $i$, the discretisated diffraction problem can be written as follows :

$$-\frac{1}{2}\chi_i + \sum_{j\in FS} \chi_j \left( D_{if} - (S+if)\frac{\omega^2}{g}\frac{\mu}{n^2} S_{ij} \right) + \sum_{j\in C} \chi_i \left( D_{ij} - \alpha_j S_{ij} \right) + \sum_{j\in F+I+\Sigma} \chi_j D_{ij} + \sum_I \sigma_j S_{ij} = -\sum_{j\in F+I+\Sigma} \sigma_j S_{ij} \tag{2.7}$$

with $\forall j \in C, \quad \sigma_j = -\left[ \frac{\partial \Phi_I(M_j)}{\partial n(M_j)} - \alpha(M_j)\Phi(M_j) \right]$. $M_j = \begin{cases} x_j \\ y_j \\ z_j \end{cases}$ the gravity center of panel $j$.

On the control cylinder, by assuming it far enough from structures, the complex potential corresponds to the linear solution on every panel $j$ :

$$\Phi_I(M_j) = -i\frac{Ag}{\omega}\frac{\cosh(k(z_j+h))}{\cosh(kh)} e^{ik(x_j\cos(\beta)+y_j\sin(\beta))} \tag{2.8}$$

with $\beta$ the incident angle in relation to (Ox) axis.

By derivation of the previous expression, we obtain the expression of $\frac{\partial \Phi_I}{\partial n(M_j)}(M_j) = n(\vec{M}_j) \cdot \vec{\nabla}\, \Phi_I(M_j)$ on every panel $j$ :

$$\frac{\partial \Phi_I}{\partial n(M_j)}(M_j) = \frac{agk}{\omega\cosh(kh)} [p_j\cos(\beta) + q_j\sin(\beta) - ir_j\sinh(k(z_j+h))] e^{ik(x_j\cos(\beta)+y_j\sin(\beta))} \tag{2.9}$$

with $\forall j \in C, \quad \vec{n}(M_j) = \begin{cases} p_j \\ q_j \\ r_j \end{cases}$ . $\vec{n}(M_j)$ is the normal vector of panel $j$.

In the cases where several domains are connected, with porous plates or porous domains, some equations are added to the linear system in order to keep $n$ independent equations with $n$ unknowns.

The conservation of the flow and the continuity of pressure have to be verified through 2 porous named domains 1 and 2. With the source and normal dipole notation, it comes :

$$\begin{aligned} &\frac{\mu_1}{n_1}\sigma_{C_1,i} = -\frac{\mu_2}{n_2}\sigma_{C_2,j} && \text{Flow conservation} \\ &(S_1+if_1)\chi_{C_1,i} = (S_2+if_2)\chi_{C_2,j} && \text{Continuity of pressure} \end{aligned} \tag{2.10}$$

where panel i of domain 1 is blended into panel j of domain 2.

Through a porous plate, the interface respects flow conservation and pressure gradient caused by hole crossing :

$$\begin{aligned} &\frac{\mu_1}{n_1}\sigma_{C_1,i} = -\frac{\mu_2}{n_2}\sigma_{C_2,j} && \text{Flow conservation} \\ &\sigma_{C_1,i} = \frac{(S_1+if_1)\chi_{C_1,i} - (S_2+if_2)\chi_{C_2,i}}{\frac{a_J(1-\tau)}{\tau k_c}\frac{\mu_1}{n_1} + \frac{i}{\sqrt{2}}\sqrt{-(\frac{a_J(1-\tau)}{\tau k_c}\frac{\mu_1}{n_1})^2 + \sqrt{(\frac{a_J(1-\tau)}{\tau k_c}\frac{\mu_1}{n_1})^4 + 4(\frac{4K}{3\pi\omega}\frac{\mu_1^2}{n_1^2})^2 |(S_1+if_1)\chi_1 - (S_2+if_2)\chi_2|^2}}} && \text{Pressure gradient} \end{aligned} \tag{2.11}$$

## 2.2 Sensitivity on parameters

In this section, we test the sensitivity of our model to four main parameters in a basic configuration described in figure 2.2. The tested parameters are :

- The mesh size $ll$.
- The length of the wave channel $lc$ upstream and downstream the structure.
- The porosity $n$ of the porous medium.
- The stones size $d_{n50}$ of the porous medium.

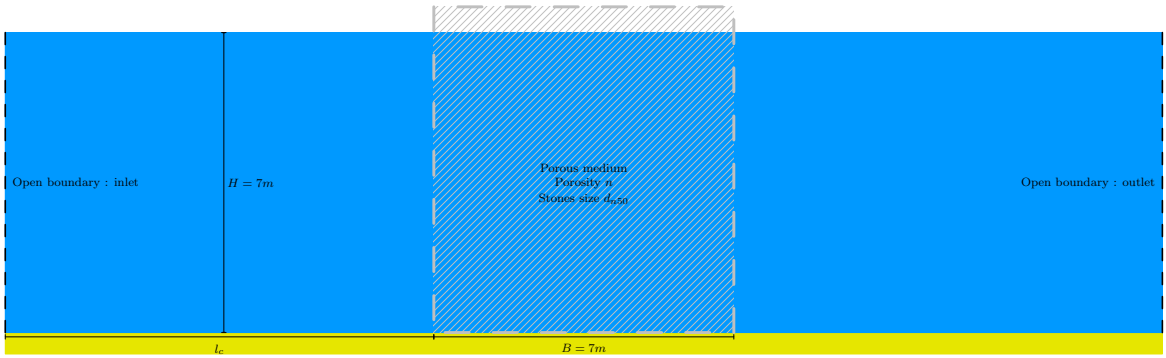


Figure 2.2: Basic configuration, Sensitivity of *Diffra3D* model to $ll$, $l_c$, $n$ and $d_{n50}$

### 2.2.1 Mesh size

The mesh elements are triangles or quadrangles. We vary the size of the elements from $ll \approx 2m$ to $ll \approx 0.1m$ (Fig. 2.3 and 2.4). The influence on the reflection and the transmission coefficients for waves with an incident amplitude of $A_i = 250mm$ are checked for these two configurations. The interior meshes of pure fluid domains on either side of the porous medium are not use. The problem is defined on the boundaries using the boundaries using the boundary element method (BEM). Inside the porous structure, the nodes of the mesh are used only to compute velocities in order to define the characteristic flow velocity $v_d$.

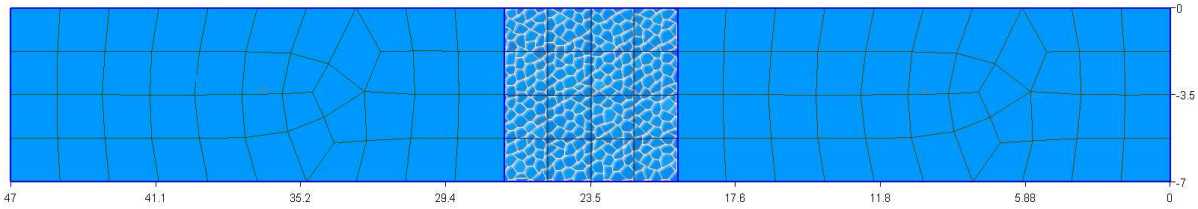


Figure 2.3: Mesh size $ll \approx 2m$, $l_c = 20m$, $n = 40\%$, $d_{n50} = 60cm$, Basic configuration

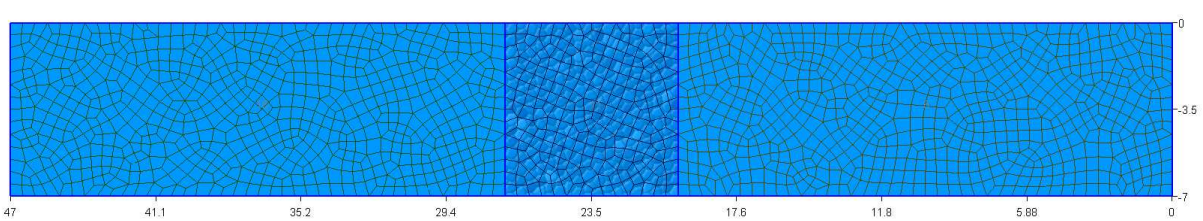


Figure 2.4: Mesh size $ll \approx 0.5m$, $l_c = 20m$, $n = 40\%$, $d_{n50} = 60cm$, Basic configuration

The yellow, green, red and blue curves (Fig. 2.5 and 2.6) correspond respectively to results obtained with meshes more and more refined : $ll \approx 2m$, $ll \approx 1m$, $ll \approx 0.5m$ and $ll \approx 0.1m$. The yellow curve stands completely out from the others curves for periods $T \leq 3.5s$, which corresponds to $\lambda/ll = 9.4$. The green curve also

starts to diverge below $T \leq 2.5s$ ($\lambda/ll = 9.7$). A minimum of *10 meshes per wavelength* is a criterion to respect. For the next sensitivity cases, we adopt a refined mesh with $ll \approx 0.5m$. The BEM method enables the use of big meshes.

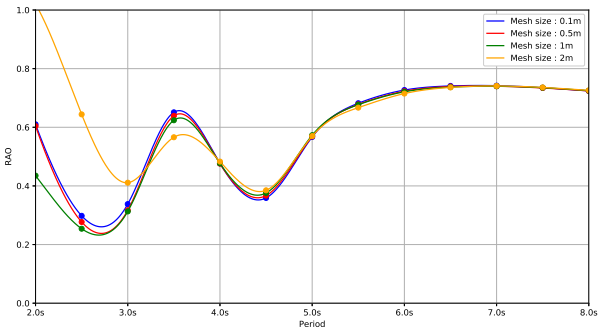


Figure 2.5: Reflection coefficient, $A_i = 250mm$
Sensitivity to mesh size

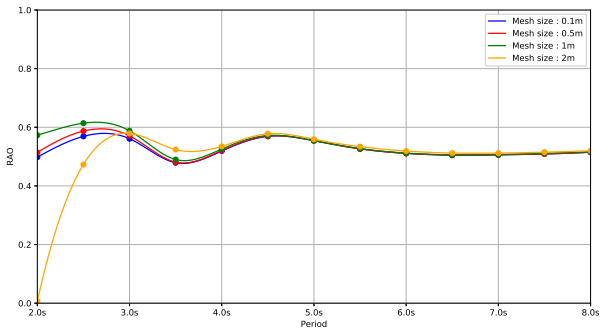


Figure 2.6: Transmission coefficient, $A_i = 250mm$
Sensitivity to mesh size

## 2.2.2 Length of the wave tank

Now, we vary the length of the wave channel upstream and downstream from the structure to see if the near field has major influence. The reflection and transmission are presented on figures 2.7 and 2.8. The wave tank is varied between $l_c = 5m$ (blue curve) to $l_c = 50m$ (yellow curve). In a common case like this, the near field is quickly negligible. It does not greatly perturb the results. The length of the wave channel on either side of the structure is not a critical parameter.

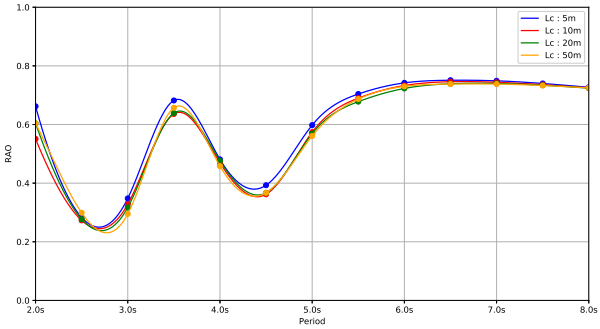


Figure 2.7: Reflection coefficient, $A_i = 250mm$
Sensitivity to channel's length

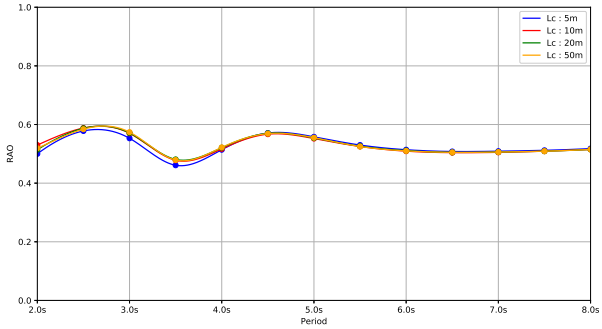


Figure 2.8: Transmission coefficient, $A_i = 250mm$
Sensitivity to channel's length

## 2.2.3 Porosity

For a specific geometry, we want to know how much the porosity of a porous medium plays a role on its hydrodynamic performance. The results for three porosities are displayed in figures 2.9 and 2.10 : $n = 36\%$ (blue curve), $n = 40\%$ (red curve) and $n = 44\%$ (green curve). We observe that a variation of $\pm 4\%$ of porosity leads to consequential changes ($\gg 10\%$) on reflection and transmission coefficients. This is a crucial parameter. The porosity of a porous medium depends greatly on the operators laying method. A reliable control of the porosity during the laying is necessary to get close to the hydrodynamic behaviour of a designed porous structure.

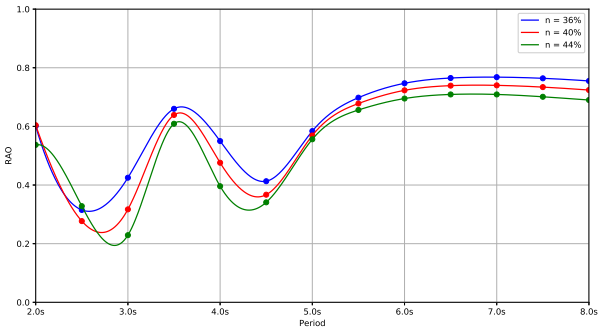


Figure 2.9: Reflection coefficient, $A_i = 250mm$
Sensitivity to porosity

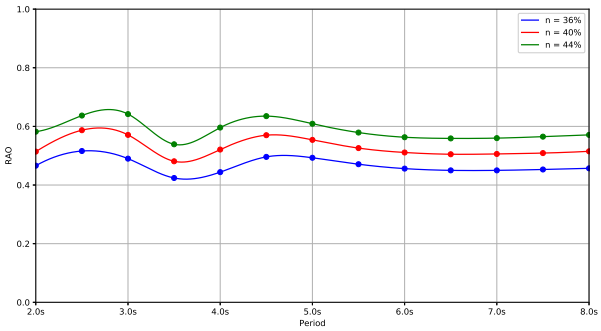


Figure 2.10: Transmission coefficient, $A_i = 250mm$
Sensitivity to porosity

### 2.2.4 Porosity surface

The concept of porosity surface defined as $\mu = 1-(1-n)^{2/3}$ was introduced in :

- The free surface equation (1.13).
- The equation of conservation of the flow between two continuous media (1.14).

The basic configuration of figure 2.2 is tested with two cases. The results are displayed in figure 2.11 and 2.12 : $\mu = n = 40\%$ (red curve) and $\mu = 1-(1-n)^{2/3} = 29\%$ (blue curve). The porosity surface $\mu$ is smaller than the volumetric porosity $n$. Its implementation modifies the dispersion relation inside the porous medium. The blue curve is shifted towards the larger periods. The reflection is increased and the transmission decreased.

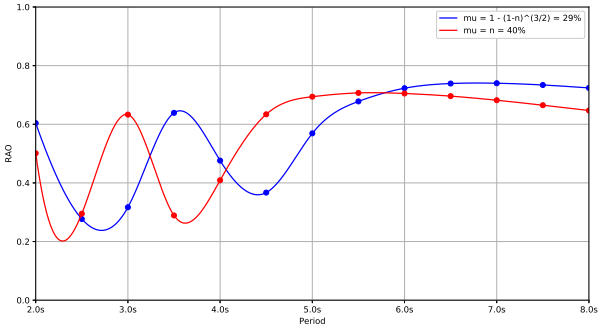


Figure 2.11: Reflection coefficient, $A_i = 250mm$
Sensitivity to porosity surface

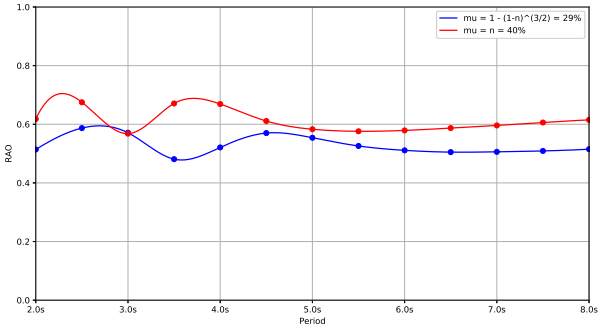


Figure 2.12: Transmission coefficient, $A_i = 250mm$
Sensitivity to porosity surface

### 2.2.5 Size of the stones

The size of the rocks is the second parameter defining a porous medium. The figures 2.13 and 2.14 show the results of this sensitivity. We start with $d_{n50} = 60cm$ (green curve) and we vary it by $\pm 10\%$ (orange and red curves) and $\pm 50\%$ (yellow and blue curves). The porosity is fixed to $n = 40\%$. The variation by $\pm 10\%$ of the size of the stones does not greatly change the hydrodynamic coefficients (a few percent). Nevertheless, a variation in stone size by $-50\%$ leads to a more significant change than a variation of $+50\%$. At some point, the flow becomes less turbulent and the viscous dissipation is dominating. We have to note that the viscous part of Forchheimer law is $a = f(d_{n50}^2)$ when the turbulent part is $b = g(d_{n50})$.

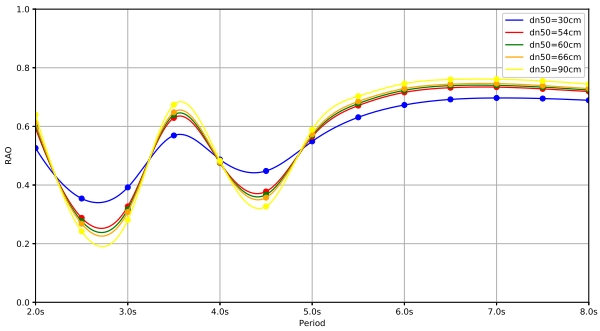


Figure 2.13: Reflection coefficient, $A_i = 250mm$
Sensitivity to rocks' size

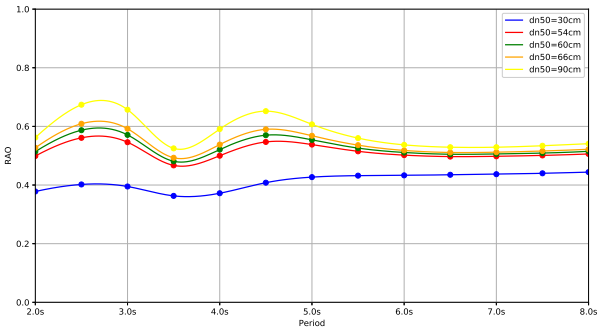


Figure 2.14: Transmission coefficient, $A_i = 250mm$
Sensitivity to rocks' size

# 3 EULERIAN NAVIER-STOKES MODEL

As stated in chapter 1.1, one of the most broadly used approaches in simulating flow in porous medium is the VOF method which solve the global equation of the fluid mechanics with all the non-linearities. The procedure to derive the Navier-Stokes equation for a fluid with a free surface is called the volume-averaging Reynolds-averaged (VARANS) equations. A detailed mathematical derivation of the VARANS equations can be found in del Jesus et al. (2012) [14]. Jensen et al. (2014) [25] and Higuera et al. (2014) [23] & [24] implemented the set of equations in the open-source software *OPENFOAM*. Jensen added his developments to the wave module called *Wave2Foam*. Higuera's developments are available in the latest *OPENFOAM*'s versions under the name of *IHFOAM*.

In this body of work, we only use *Wave2Foam* with the developments of Jensen et al. (2014) as a tool in order to compare the results of our diffraction code *Diffra3D* with those obtained with a VOF code. The comparisons have only been done for the reflection-transmission experimental tests (Chap. 3.3).

**Porous media resistance forces**

The resistance forces inside a porous medium are also modelled by the extended Forchheimer equation (4.5). The extended Forchheimer equation is introduced to the Navier-Stokes equations as a closure model for handling the porous media resistance force. They can not be computed directly. This is similar to the concept of a closure model for turbulence modelling.

The resistance coefficients of Burcharth & Andersen (1995) [4] implemented in *Diffra3D* were also integrated in *Wave2Foam*. They are as follows :

$$\begin{aligned} a &= \alpha \frac{(1-n)^2}{n^3} \frac{\nu}{g d_{n50}^2} \\ b &= \beta \frac{1-n}{n^3} \frac{1}{g d_{n50}} \\ c &= C_M \frac{1-n}{n} \frac{1}{g} \end{aligned} \tag{3.1}$$

where $\alpha$, $\beta$ and $C_M$ are some empirical coefficients depending on flow parameters and stone parameters, see section 1.4.2.

The concept of surface porosity $\mu$ was not implemented.

**Turbulence**

The implementation of Jensen et al. (2014) [25] uses no turbulence closure. The eddy viscosity is not taken into account. No wave breaking occurred in the test cases. A turbulence closure model would give negligible effects. Higuera et al. (2014-1) [23] where validation tests were performed applying a $k-\epsilon$ turbulence closure model and Higuera et al. (2014-2) [24] where a $k-\omega-SST$ closure model was applied, have confirmed the validity of this approximation.

The above hypotheses concern the flow outside the porous media. Inside a porous medium, the actual turbulence levels are not small enough to be neglected. However, they are directly included through the extended Forchheimer equation. If the resistance coefficients $\alpha$ and $\beta$ are found from measurements, they already include the effects of turbulence. Coefficients found from a numerical calibration including a turbulence model may not be comparable with coefficients found from experiments.

# 4 ANALYTICAL MODEL

One of the first analytical models to describe reflection-transmission problem through an idealised vertical porous structure was developed by Madsen and White (1976) [40]. The solution of the simple test case (Fig. 4.1) is based on a harmonic method under long wave theory presented at chapter Chap 2.2. The procedure was tested against experimental reflection and transmission coefficients (Wilson (1971) [64], Keulegan (1973) [27]).

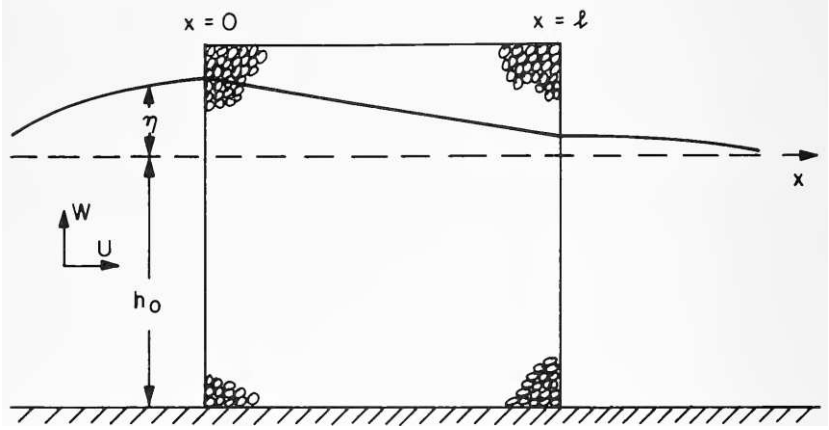


Figure 4.1: Definition sketch, Analytical model

Outside of the structure and inside it, the flow respects the following linearised governing equations, with the notation used previously :

$$\text{Continuity} \qquad n\frac{\partial \eta}{\partial t} + h\frac{\partial V_d}{\partial x} = 0 \tag{4.1}$$

$$\text{Conservation of momentum} \qquad S\frac{\partial V_d}{\partial t} + g\frac{\partial \eta}{\partial x} + f\omega V_d = 0 \tag{4.2}$$

where $h$ is the water depth before and after the structure, $V_d$ the horizontal filter velocity. We have $n = 0$, $S = 1$ and $f = 0$ in the pure fluid domain.

The governing equation are linear. Thus, we can look for a harmonic solution with the variables $\eta(x,t)$ and $V_d(x,t)$ :

$$\eta(x,t) = \Re\left(\zeta(x)\,\mathrm{e}^{i\omega t}\right) \tag{4.3}$$

$$V_d(x,t) = \Re\left(v_d(x)\,\mathrm{e}^{i\omega t}\right) \tag{4.4}$$

The general solution for the free surface and the motion outside the structure is given by :

$$For\ x \le 0 \begin{cases} \zeta(x) & = A_i\, e^{-ikx} + A_r\, e^{ikx} \\ v_d(x) & = \sqrt{\frac{g}{h}}\left(A_i\, e^{-ikx} - A_r\, e^{ikx}\right) \end{cases} \tag{4.5}$$

$$For\ x \ge l \begin{cases} \zeta(x) & = A_t\, e^{-ik(x-l)} \\ v_d(x) & = \sqrt{\frac{g}{h}} A_t\, e^{-ik(x-l)} \end{cases} \tag{4.6}$$

where $A_i$, $A_r$ and $A_t$ are respectively the amplitudes of the incident, reflected and transmitted waves. $A_i$ is taken as a real number. $A_r$ and $A_t$ are complex. $k$ is the complex wave number given by :

$$k = \frac{\omega}{\sqrt{gh}} \sqrt{n} \sqrt{S - if} \tag{4.7}$$

The general solution for the flow in the porous structure is found as :

$$For\ 0 \le x \le l \begin{cases} \zeta(x) & = A_+\, e^{-ikx} + A_-\, e^{ik(x-l)} \\ v_d(x) & = \sqrt{\frac{g}{h}} \frac{\sqrt{n}}{\sqrt{S-if}} \left(A_+\, e^{-ikx} + A_-\, e^{ik(x-l)}\right) \end{cases} \tag{4.8}$$

where $A_+$ and $A_-$ are respectively the amplitudes of the waves propagating in the positive and negative x-direction inside the porous structure.

The problem involve four unknowns that are the complex wave amplitudes $A_r$, $A_t$, $A_+$ and $A_-$. They are determined by matching surface elevations and velocities at the common boundaries :

$$For\ x = 0 \begin{cases} A_i + A_r & = A_+ + A_-\, e^{-ikl} \\ A_i - A_r & = \frac{\sqrt{n}}{\sqrt{S-if}} \left(A_+ + A_-\, e^{-ikl}\right) \end{cases} \tag{4.9}$$

$$For\ x = l \begin{cases} A_t & = A_+\, e^{-ikl} + A_- \\ A_t & = \frac{\sqrt{n}}{\sqrt{S-if}} \left(A_+\, e^{-ikl} + A_-\right) \end{cases} \tag{4.10}$$

Madsen and White solve this system to obtain the complex amplitudes $A_r$, $A_t$ and the velocity inside the structure :

$$\frac{A_t}{A_i} = \frac{4\epsilon}{(1+\epsilon)^2\, e^{ikl} - (1-\epsilon)^2\, e^{-ikl}} \tag{4.11}$$

$$\frac{A_r}{A_i} = \frac{(1-\epsilon^2)\left(e^{ikl} - e^{-ikl}\right)}{(1+\epsilon)^2\, e^{ikl} - (1-\epsilon)^2\, e^{-ikl}} \tag{4.12}$$

$$For\ 0 \le x \le l, \quad v_d(x) = \sqrt{\frac{g}{h}} \frac{A_t}{2} \left[(1+\epsilon)\, e^{-ik(x-l)} + (1-\epsilon)\, e^{ik(x-l)}\right] \tag{4.13}$$

where $\epsilon$ is the shorthand notation for $\frac{\sqrt{n}}{\sqrt{S-if}}$.

The transmission coefficient T and a reflection coefficient R are given by :

$$T = \frac{|A_t|}{A_i} \tag{4.14}$$

$$R = \frac{|A_r|}{A_i} \tag{4.15}$$

The dissipated energy by the breakwater is such as :

$$E_d = 1 - T^2 - R^2 \tag{4.16}$$

The higher dissipation of energy, the more effective the breakwater is.

PART 3

# EXPERIMENTS AND COMPARISONS

# 1 SIMILARITY AND SCALE FACTORS

Small-scale test campaigns involve the respect of physical quantities in order to be representative of reality. The numerical modelling of a porous structure exposed to an incident swell theoretically involves a formulation which distinguishes different flow regimes. It is necessary to verify that the scaling of the model keeps the characteristics of the real-scale flow.

The Reynolds-number defined in section 1.4.4.3.1 estimates the relative importance of a turbulent resistance over a laminar one. The flow is considered fully turbulent when $R_e > 300$. Nevertheless, out of the armour layer of a breakwater where very high KC numbers are found during violent wave conditions, the flow in a porous media inside breakwaters are mainly part of the low-KC flows.

Downscaling also requires attention to be paid to a second parameter, namely the conservation of Froude number, which is characteristic of free-surface flows. Froude number specifies the relative importance of the inertial forces (kinetic energy of the particles) relative to the gravitational force applied to the fluid (potential energy of the particles). It is defined as follows :

$$F_r = \frac{u}{\sqrt{gh}} \tag{1.1}$$

with :

- $u$ a characteristic fluid velocity ($m.s^{-1}$).
- $h$ the water depth ($m$).
- $g$ the gravitational acceleration ($m.s^{-2}$).

We define the scale-factor $\lambda$ between the scale-model dimensions $L_s$ and the real-scale model $L_r$. The respect of Froude number implements a scale-factors for :

- Length : $\frac{L_r}{L_s} = \lambda$.
- Time : $\frac{t_r}{t_s} = \sqrt{\lambda}$.
- Velocity : $\frac{v_r}{v_s} = \sqrt{\lambda}$.
- Force : $\frac{F_r}{F_s} = \lambda^3$.

Now, we apply the scale transformation to the Forchheimer equation. The kinematic viscosity of water and the gravitational acceleration are fixed. We assume the porosity and the tortuosity coefficients $\alpha$ and $\beta$ are preserved while downscaling, so we get the following scale factors corresponding to the :

- Laminar term $a\vec{v}$ : $\frac{\sqrt{\lambda}}{\lambda^2} = \lambda^{\frac{-3}{2}}$.
- Turbulent term $b|\vec{v}|\vec{v}$ : $\frac{\sqrt{\lambda}^2}{\lambda} = 1$.
- Inertial term $c\frac{\partial \vec{v}}{\partial t}$ : $\frac{\sqrt{\lambda}}{\sqrt{\lambda}} = 1$.

The Froude scale procedure tends to overestimate the dissipation due to the laminar term but maintains the good ratio for turbulence and inertia dissipations.

## 1.1 Steady laminar flow

Consider, at the real scale, a steady pure laminar flow through a porous medium. The turbulent and the inertia terms are negligible. It is then possible to choose a specific scale to apply to the stone diameters to keep the laminar hydraulic gradient constant :

$$\frac{\sqrt{\lambda}}{\lambda_{stones}^2} = 1 \rightarrow \frac{d_r}{d_s} = \lambda_{stones} = \lambda^{\frac{1}{4}} \tag{1.2}$$

In this specific case, it is necessary to take artificially bigger stones than simple Froude scaling $\lambda$ would have given.

## 1.2 Steady turbulent flow

Breakwater scale-models are usually designed at scales between 1/10th and 1/30th. Out of the armour layer where the flow is without doubt fully turbulent, the situation in the core of a porous structure is different. In order to keep the dissipation rate in a porous medium scale-model equal to a real one, authors, like Jensen and Klinting (1983) [26], looked for a stone scale that keeps the hydraulic gradient $av + bv^2$ constant. This time again, we assume a steady flow. Using the Burcharth and Andersen (1995) [4] dissipation coefficients, it yields :

$$\frac{I_r}{I_s} = \frac{\alpha \frac{(1-n)^2}{n^3} \frac{\nu}{g d_r^2} v_r + \beta \frac{1-n}{n^3} \frac{1}{g d_r} v_r^2}{\alpha \frac{(1-n)^2}{n^3} \frac{\nu}{g d_s^2} v_s + \beta \frac{1-n}{n^3} \frac{1}{g d_s} v_s^2} \tag{1.3}$$

As Jensen and Klinting, we define a scale for the stone diameters $\lambda_{stones} = d_r / d_s$. Inserting $v_r / v_s = \lambda$ required by Froude's model, it yields a second-degree equation in $\lambda_{stones}$ :

$$\lambda_{stones}^2 + \frac{F_{or}}{\sqrt{\lambda}} \lambda_{stones} - \sqrt{\lambda}(1 + F_{or}) = 0 \tag{1.4}$$

with $F_{or}$ the Forchheimer number for the scale-model defined as :

$$F_{or} = \frac{\beta \frac{1-n}{n^3} \frac{1}{g d_r} u_r^2}{\alpha \frac{(1-n)^2}{n^3} \frac{\nu}{g d_r^2} u_r} = \frac{\beta}{\alpha} \frac{1}{1-n} R_{er} \tag{1.5}$$

The solution of the equation (1.4) is given by :

$$\lambda_{stones} = \frac{F_{or}}{2\sqrt{\lambda}} \left[ \sqrt{1 + 4\lambda^{\frac{3}{2}} \frac{1 + F_{or}}{F_{or}^2}} - 1 \right] \tag{1.6}$$

It appears that if $F_{or} \rightarrow 0$ (pure laminar flow), $\lambda_{stones} \rightarrow \lambda^{\frac{1}{4}}$ and if $F_{or} \rightarrow +\infty$ (fully turbulent flow), $\lambda_{stones} \rightarrow \lambda$.

## 1.3 Porous plate

The value of pressure loss is kept by scaling using the Froude's similarity because the theoretical expression is the sum of a turbulent term (in $v^2$) and an inertia one (in $\frac{\partial v}{\partial t}$).

# 2 FIRST CAMPAIGN : SLOSHING

This chapter is devoted to the experimental tests on a hexapode in order to extract the characteristics of a given porous medium. In the literature, recent investigations performed by Molin & al. (2016) [45] and Arnaud& al. (2017) [1]) deal with damping effects of porous media trough sloshing tests. The porous media are idealised by dense arrays of smooth vertical cylinders emerging from the free surface. The porosity of the media, the cylinder diameter and the specific surface are finely controlled. The cylinder diameter is small compared with the wavelength. The modification of the dispersion relation is studied through a semi-analytical model. The arrays of cylinders are supposed homogeneous porous media and a linearised potential flow approach is used. Friction and inertia coefficients are added a posteriori to account for viscous flow effects and for added inertia effects.

In our case, we are dealing with irregular stones. The semi-empirical coefficients a, b and c of the extended Forchheimer equation introduced in the developed numerical diffraction model are not the same than those used for cylinders. The numerical model is calibrated to fit the data. Laws for the inertia and dissipation coefficients are proposed. Three porous media sharing the same parameter $D_{n50}$ were investigated in order to observe the influence of size distribution spreading on the dissipation coefficients.

## 2.1 Experimental set-up

Sloshing tests are performed with a tank filled with water and a porous medium at the bottom. The tank measures $L = 60cm$ long and $B = 50cm$ wide. The porous medium fits these dimensions and the vertical dimension is $12.5cm$ high. The water depth is either $26.8cm$ or $40.0cm$ (including the porous medium). In this configuration, our porous media don't emerge from the free surface. We choose this configuration of tests to simplify the problem as much as possible. We are mainly interested in the values of the dissipation and inertia coefficients.

Figure 2.1: The tank on the hexapod, $h = 40.0cm$, Sloshing tests

The system is installed on the hexapod of *Ecole Centrale de Marseille* (Fig. 2.1). The hexapod is a dynamic system providing six degrees of freedom. The six independent actuators allow motion generation for up to 1T of load. The maximum acceleration is $1g$ and the maximum speed is $1m.s^{-1}$. The displacements as part of the tests are harmonic in the longitudinal direction of the tank, with amplitudes from $A = 1mm$ to $A = 5mm$. Several frequencies around the resonance peak (Eq. (2.1)) are scanned. The free surface elevation at one end of the tank is measured with a capacitive probe. The RAO can then be computed. The global loads on the hexapod tray are also measured through loads cells installed between each actuators and the tray.

The natural frequency of the first sloshing mode of a tank with water is merely obtained by :

$$\omega^2 = \frac{g\pi}{L}\tanh\left(\frac{h\pi}{L}\right) \tag{2.1}$$

Placing a porous medium in the tank attenuates the resonance and shifts the natural frequency to lower frequencies. The three tested porous media share the same $d_{n50}$ but have different size distribution spreading. The table Tab. 2.1 gathers the experimental configurations. The size distribution curves are placed in Appendix A. Figure 2.2 shows the size distribution number 3.

| **Size distribution** | **Porosity $n$** | $d_{n50}$ | $d_{n85}$ | $d_{n15}$ | $\frac{d_{n85}}{d_{n15}}$ | $n_{RRd}$ | **Water depth h** |
|---|---|---|---|---|---|---|---|
| 1 | 46.6% | 4.1cm | 4.6cm | 3.6cm | 1.26 | 12.3 | 26.8cm |
| 2 | 47.5% | 4.0cm | 4.9cm | 2.9cm | 1.67 | 5.9 | 26.8cm |
| 2 | 47.5% | 4.0cm | 4.9cm | 2.9cm | 1.67 | 5.9 | 40.0cm |
| 3 | 47.5% | 4.1cm | 6.3cm | 2.7cm | 2.31 | 3.9 | 26.8cm |

Table 2.1: Size distributions, Sloshing

As mentioned in chapter 1.3, the ratio $d_{n85}/d_{n15}$ and the coefficient of uniformity $n_{RRd}$ are measures of the spreading of the size distribution in terms of rock diameters ; the higher the slope, the less spread the size

distribution. The three samples have coefficients of uniformity significantly different, from $n_{RRd}$ = 3.9 to $n_{RRd}$ = 12.3, but according to table Tab. 3.1, they are still all part of size distribution type with high gradation $1.5 < d_{n85}/d_{n15} < 2.5$.

The porosity is kept almost constant despite the change of the gradation. The constraint of the walls of the cage could explain the high porosity values we obtained during the tests. They are a little bit higher than the realistic porosity rates defined by Van Gent [60], $35\% \leq n \leq 45\%$. .

Figure 2.2: Porous medium, Sloshing tests

## 2.2 Theoretical model

Consider a 2D vertical situation in the (x, z) plan, with a rectangular tank of length L, and inside a porous medium of height d, named sub-domain 1 (Fig. 2.3). The total water depth is h, and the free fluid domain, above the porous medium, is named sub-domain 2.

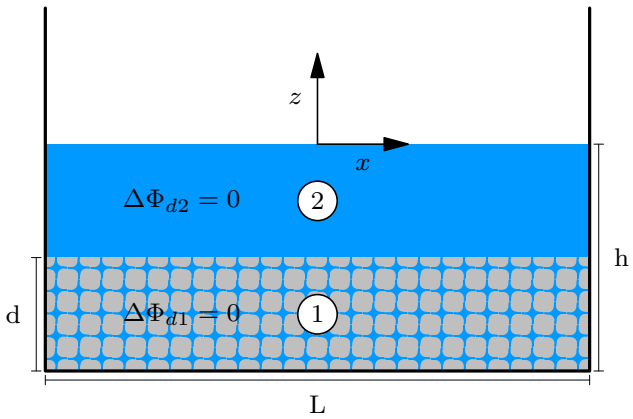


Figure 2.3: Geometry, Sloshing tests

The harmonic displacements of the tank are along the (Ox) axis, with an amplitude A and a pulsation $\omega$.

$$X(t) = A\sin(\omega t) \tag{2.2}$$

First, only the inertia loads that apply to the fluid in a moving frame of reference are considered. A new inertia force is applied and can be added in equation (1.1) of section 2.1.1.1 that leads to :

$$\iiint_F \frac{\partial v_{pR}}{\partial t}\,\mathrm{d}V = -\frac{1}{\rho}\iint_{\partial\Sigma} p_I\,\overrightarrow{\mathrm{d}S} - \iiint_P C_M\frac{\partial v_{pR}}{\partial t}\,\mathrm{d}V - \iiint_\Sigma \frac{\partial v_E}{\partial t}\,\mathrm{d}V \tag{2.3}$$

where $F$ refers to the fluid domain, $P$ to the rock domain and $\Sigma = F + P$ the overall domain, $v_{pR} = v_p - v_E$ is the relative pore velocity, $v_E$ is the velocity of the hexapod.

The equation (2.4) is obtained in a similar way as equation (4.8) of section 1.4.4.1. The surface integral is transformed into a volume integral thanks to Ostrogradski theorem. By expressing the equation (2.3) exclusively on $\Sigma$ and with the relative filter velocity $v_{dR} = nv_{pR} = v_d - nv_E = v_d - v_{dE}$, it yields :

$$\begin{aligned}\frac{1}{\rho}\overrightarrow{\nabla}\,p_I &= -(1+C_M\frac{1-n}{n})\frac{\partial\vec{v_{dR}}}{\partial t} - \frac{\partial\vec{v}_E}{\partial t}\\ &= -(1+C_M\frac{1-n}{n})\frac{\partial\vec{v}_d}{\partial t} + (1+C_M\frac{1-n}{n})\frac{\partial\vec{v_{dE}}}{\partial t} - \frac{1}{n}\frac{\partial\vec{v_{dE}}}{\partial t}\\ &= -(1+C_M\frac{1-n}{n})\frac{\partial\vec{v}_d}{\partial t} + C_M\frac{1-n}{n}\frac{\partial\vec{v_{dE}}}{\partial t} - \frac{1-n}{n}\frac{\partial\vec{v_{dE}}}{\partial t}\end{aligned} \tag{2.4}$$

The previous equation demonstrates that the complete momentum equation can be expressed with the absolute velocity in the relative coordinate system of the moving tank, such as :

$$\iiint_\Sigma \left(\frac{\partial\vec{v}_d}{\partial t} + \frac{1}{n}(\vec{v}_d.\overrightarrow{\nabla})\vec{v}_d\right)\mathrm{d}V = -\frac{1}{\rho}\iiint_\Sigma \overrightarrow{\nabla}\,p\,\mathrm{d}V + \iiint_\Sigma \left(\vec{g} + \vec{f_{rR}}\right)\mathrm{d}V - \iiint_\Sigma \frac{1-n}{n}\frac{\partial\vec{v_{dE}}}{\partial t} \tag{2.5}$$

with the relative filter velocity $v_{dR}$ used in the Forchheimer equation, such as :

$$\frac{1}{\rho g}\vec{f_{rR}} = -\left[a\vec{v_{dR}} + b\|\vec{v_{dR}}\|\vec{v_{dR}} + c\frac{\partial\vec{v_{dR}}}{\partial t}\right] \tag{2.6}$$

The porous medium is assumed continuous and the potential flow theory is applied to equation (2.5). The convective terms are neglected. Introducing the potential $\Phi_d = \phi_d\,\mathrm{e}^{-i\omega t}$ such as $\vec{v}_d = \overrightarrow{\nabla}\,\Phi_d$, the equation (2.5) yields :

$$-i\omega\phi_d = -\frac{p}{\rho} - gz - f'\omega(\phi_d - An\omega x) + i\omega C_M\frac{1-n}{n}(\phi_d - An\omega x) + iAn\omega^2 x\frac{1-n}{n} \tag{2.7}$$

with :

$$f'\omega = \frac{\nu}{K} + \frac{C_f}{\sqrt{K}}\overline{f'} \qquad \text{and} \qquad \overline{f'} = \frac{\int_0^T |\vec{v_{dR}}|^3\,\mathrm{d}t}{\int_0^T |\vec{v_{dR}}|^2\,\mathrm{d}t} \tag{2.8}$$

By introducing the variable $S = 1 + C_M\frac{1-n}{n} = S = 1 + (1+C_a)\frac{1-n}{n}$, the equation (2.7) becomes :

$$(f' - iS)\omega\phi_d + \frac{p}{\rho} + gz - \left(f' - iC_a\frac{1-n}{n}\right)\omega^2 Anx = 0 \tag{2.9}$$

In our case, the boundaries conditions are :

- for the free surface condition : the domain 2 is a pure fluid domain ($n_2 = \mu_2 = 1$, $S_2 = 1$ and $f_2' = 0$) :

$$\frac{\partial\phi_{d2}}{\partial z} - \frac{\omega^2}{g}\phi_{d2} = 0\Big|_{z=0} \tag{2.10}$$

- for the flow condition between the two domains :

$$\frac{\mu_1}{n_1}\frac{\partial\phi_{d1}}{\partial n} = -\frac{\partial\phi_{d2}}{\partial n}\Big|_{at\ the\ interface} \tag{2.11}$$

- for the condition of pressure conservation between the two domains :

$$(S_1 + i f_1')\phi_{d1} - (C_{a1}\frac{1-n}{n} + i f_1')An\omega x = (S_2 + i f_2')\phi_{d2}\Big|_{\text{at the interface}} \tag{2.12}$$

The efforts measured by the hexapod sensors are obtained by integrating $p_1$ and $p_2$ on the sides of the tank without forgetting to add the efforts transmitted by the rocks to the tank :

$$\sum \vec{F_{measured}} = \iint_{\partial\Sigma} p\,\overrightarrow{\mathrm{d}S} + \left( -\rho \iiint_{\Sigma} \vec{f_{rR}}\,\mathrm{d}V - \rho \iiint_{\Sigma} (1-n)\vec{g}\,\mathrm{d}V + \rho \iiint_{\Sigma} (1-n)\frac{\partial \vec{v_E}}{\partial t} \right) \tag{2.13}$$

Finally, we obtain :

$$\sum \vec{F_{measured}} = -\rho \iiint_{\Sigma} \frac{\partial \vec{v_d}}{\partial t}\,\mathrm{d}V + \rho \iiint_{\Sigma} n\vec{g}\,\mathrm{d}V = \rho \iint_{\partial\Sigma} (i\omega\Phi_d)\,\overrightarrow{\mathrm{d}S} + \rho \iiint_{\Sigma} n\vec{g}\,\mathrm{d}V \tag{2.14}$$

The inertia of the empty tank needs to be subtracted from the measured loads. Tests with an empty tank are performed prior to experimental testing.

## 2.3 Experimental results

Fourier analysis is applied to the measurement to obtain the RAO of the free surface elevation and the hydrodynamic coefficients of the tank, following :

$$F_x(t) = \Re\{i\,\rho LBh\,A\omega^2\,(C_a' + iC_b')\,\mathrm{e}^{-i\omega t}\} \tag{2.15}$$

with $X(t) = A\sin(\omega t)$ the imposed motion, $C_a'$ the added mass coefficient and $C_b'$ the damping coefficient of the global system (see Molin & Remy 2014 [43]). The coefficients $C_a'$ and $C_b'$ does not directly correspond to coefficients $S$ and $f$ of the porous medium. They are respectively proportional to the in-phase and quadrature hydrodynamic efforts.

The figures 2.4, 2.5 and 2.6 show the experimental results for the amplitude RAO and the dissipation coefficients of the system for the four amplitudes and the three size distributions. The different excitation amplitudes are represented by distinct colors and every size distribution has a distinct marker.

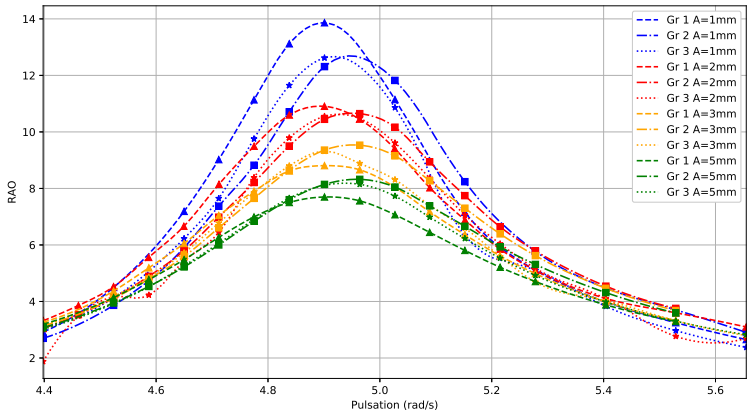


Figure 2.4: RAO, $h = 26.8cm$, Sloshing tests

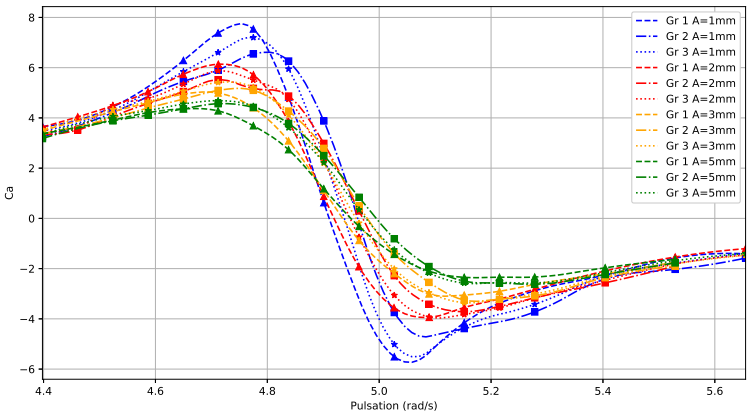


Figure 2.5: $C'_a$, $h = 26.8cm$, Sloshing tests

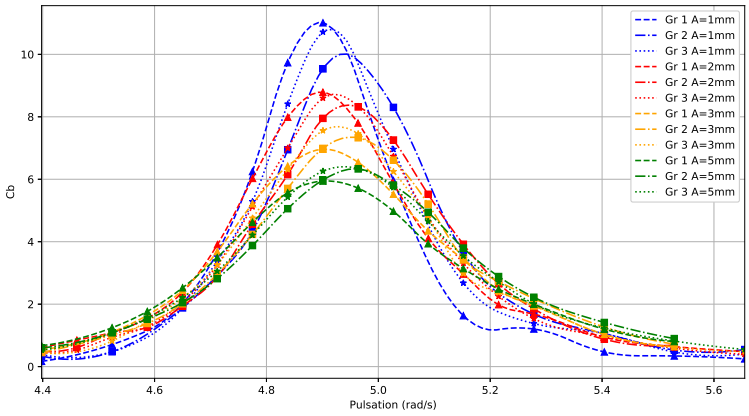


Figure 2.6: $C'_b$, $h = 26.8cm$, Sloshing tests

We already notice that the system has a non-linear damping law. The RAO and the damping coefficient $C'_b$ increases with the excitement amplitude whereas the inertial coefficient becomes smaller.

We also observe that the resonance peak moves a little between the three size distributions. This may suggest dissipation depends on some characteristics of the size distribution other than the nominal diameter $D_{n50}$ and the porosity (both were constants). Unfortunately, these raw results make it difficult to give qualitative conclusions on the influence of the size distribution spreading. The curves of the third size distribution (the most spread one) are located between the two others.

The results for the second water depth $h = 40cm$ and for the size distribution 2 are presented in the following figures 2.7, 2.8 and 2.9. Due to matching resonant frequencies, the tests with a displacement $A = 5mm$ were not performed as it resulted in overtopping. The peak of the resonance at $h = 40cm$ naturally shifted to the higher frequencies according to equation (2.1).

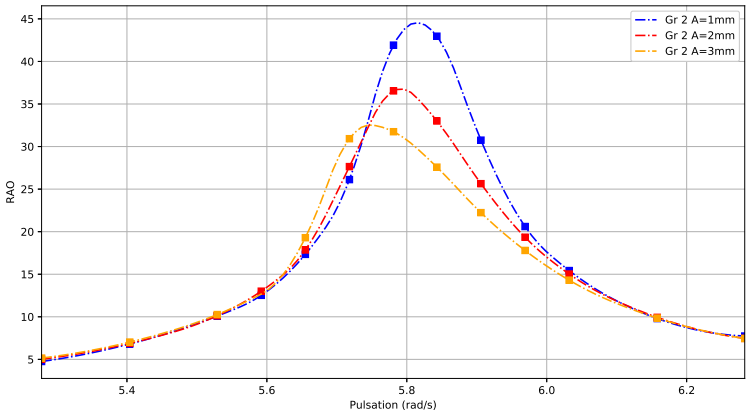


Figure 2.7: RAO, $h = 40.0cm$, Sloshing tests

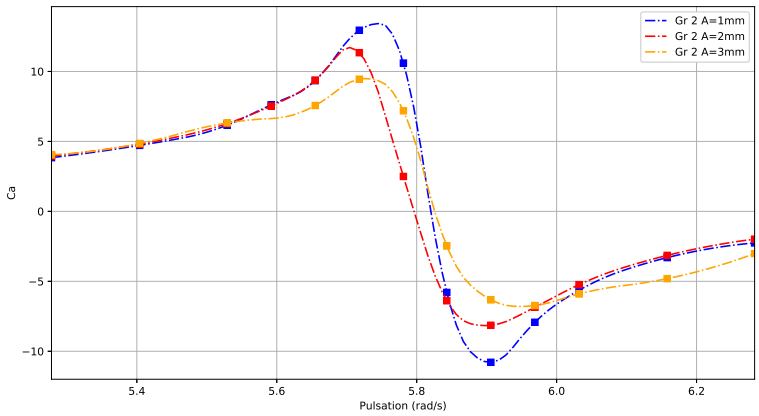


Figure 2.8: $C'_a$, $h = 40.0cm$, Sloshing tests

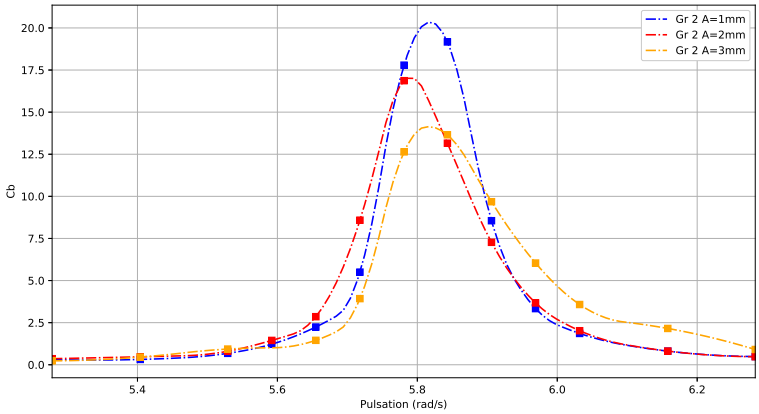


Figure 2.9: $C'_b$, $h = 40.0cm$, Sloshing tests

## 2.4 Parameters' investigation of a porous medium

In this section, the dissipation coefficients $S$ and $f$ of the porous medium are investigated using the numerical model *Diffra3D*.

The problem of finding numerical coefficients $S$ and $f$ to match with the measured coefficients $C'_a$ and $C'_b$ has an unique solution. We decide to use the coefficients proposed by Burcharth and Andersen (1995). They are as follows :

$$\begin{aligned} a &= \alpha \frac{(1-n)^2}{n^3} \frac{\nu}{g d_{n50}^2} \\ b &= \beta \frac{1-n}{n^3} \frac{1}{g d_{n50}} \\ c &= C_M \frac{1-n}{n} \frac{1}{g} \end{aligned} \tag{2.16}$$

where $\alpha$, $\beta$ and $C_M$ are some empirical coefficients depending on flow parameters and stone parameters, see section 1.4.2.

For the amplitudes $A = 2mm$ to $A = 5mm$, according to Burcharth and Andersen (1995), the flow generated by the motion of the tank corresponds to low KC numbers ($KC < 10$) and to fully turbulent regime. For $A = 1mm$, far from the resonance, $R_e$ is close to 300. In the literature, this is the limit of a fully turbulent flow. For these reasons, the coefficient $\alpha$ is set to 500. The $a$ coefficient is now a constant value. This value theoretically corresponds to the laminar part of the dissipation. For the tests performed with the hexapod, we want to determine the better values of $(b,c)$, or in the same way $(\beta, C_M)$ by minimising the root square error (RMS) defined as :

$$\epsilon(\omega) = \sqrt{\frac{(C'_{ac} - C'_{am})^2}{C'^2_{am}} + \frac{(C'_{bc} - C'_{bm})^2}{C'^2_{bm}}} \tag{2.17}$$

where $C'_{am}$ and $C'_{bm}$ correspond to values of measured $C'_a$ and $C'_b$ and $C'_{ac}$ and $C'_{bc}$ are the values computed with *Diffra3D*.

Figures 2.10 represent two examples of RMS ranges for the second size distribution, $T = 1.22s$ and $T = 1.35s$, $A_i = 3mm$. The blue points show the couple $(\beta, C_M)$ for which the RMS is minimal.

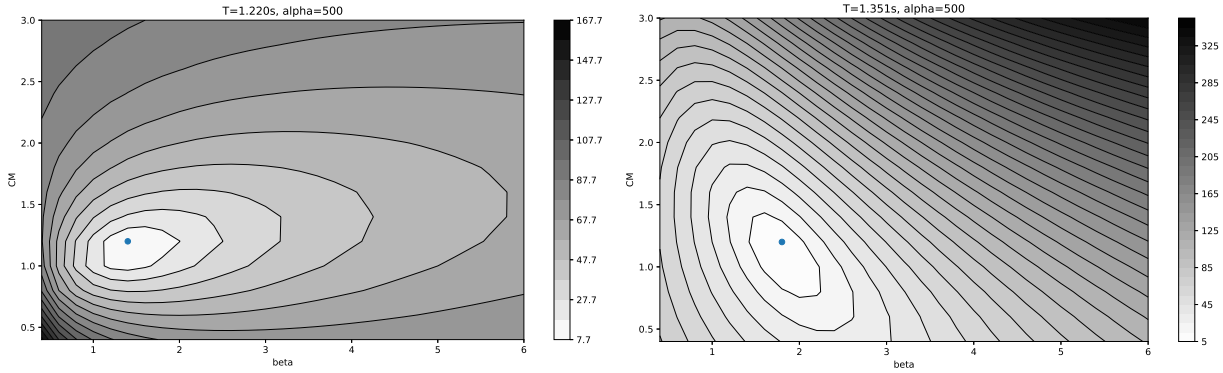


Figure 2.10: RMS for size distribution 2, $A = 3mm$, $h = 26.8cm$, Sloshing tests

This optimisation shows that $\beta$ depends on the adimensional numbers $KC$ and $\beta_S$. In this way, we observe a variation of the coefficients $(\beta, C_M)$ function of the flow inside the porous medium, and that for every size distribution and amplitude. Some curve fittings were performed in order to determine the best dependences with adimensional numbers. Finally, we propose $\beta = f(R_e)$ and $C_M = g(KC)$ as :

$$\begin{aligned} \beta &= 0.3 + \frac{3200}{KC\beta_S} = 0.3 + \frac{3200}{R_e} \\ C_M &= 1.6 - 0.2KC \end{aligned} \tag{2.18}$$

We introduced this new value of $\beta$ in (2.16), leading to :

$$\begin{aligned} a v_d + b v_d^2 &= 500\frac{(1-n)^2}{n^3}\frac{\nu}{g d_{n50}^2} v_d + \left(0.3 + \frac{3200}{R_e}\right)\frac{1-n}{n}\frac{1}{g d_{n50}} v_d^2 \\ &= 500\frac{(1-n)^2}{n^3}\frac{\nu}{g d_{n50}^2} v_d + \frac{3200 n\nu}{\hat{v_d} d_{n50}}\frac{1-n}{n^3}\frac{1}{g d_{n50}} v_d^2 + 0.3\frac{1-n}{n}\frac{1}{g d_{n50}} v_d^2 \\ &= \left(500 + \frac{3118\delta n}{1-n}\right)\frac{(1-n)^2}{n^3}\frac{\nu}{g d_{n50}^2} v_d + 0.3\frac{1-n}{n}\frac{1}{g d_{n50}} v_d^2 \\ &= 2950\frac{(1-n)^2}{n^3}\frac{\nu}{g d_{n50}^2} v_d + 0.3\frac{1-n}{n}\frac{1}{g d_{n50}} v_d^2 \\ &= \alpha'\frac{(1-n)^2}{n^3}\frac{\nu}{g d_{n50}^2} v_d + \beta'\frac{1-n}{n}\frac{1}{g d_{n50}} v_d^2 \\ &= a' v_d + b' v_d^2 \end{aligned} \tag{2.19}$$

where $\delta = \frac{v_d}{\hat{v_d}} \approx 0.9$ and $n \approx 0.47$.

From equation (2.19), new values for $\alpha$ and $\beta$ are determined : $\alpha = 2950$ and $\beta = 0.3$. The new value for $\alpha$ is large compared to the original value ($\alpha = 500$). This corresponds to a higher dissipation due to the laminar flow.

As we can see in the figures 2.11, 2.12, 2.13 and 2.14, the numerical results with the parameters $\alpha = 2950$, $\beta = 0.3$ and $C_M = 1.6 - 0.2KC$ compare well with the experimental results for $h = 26.8cm$.

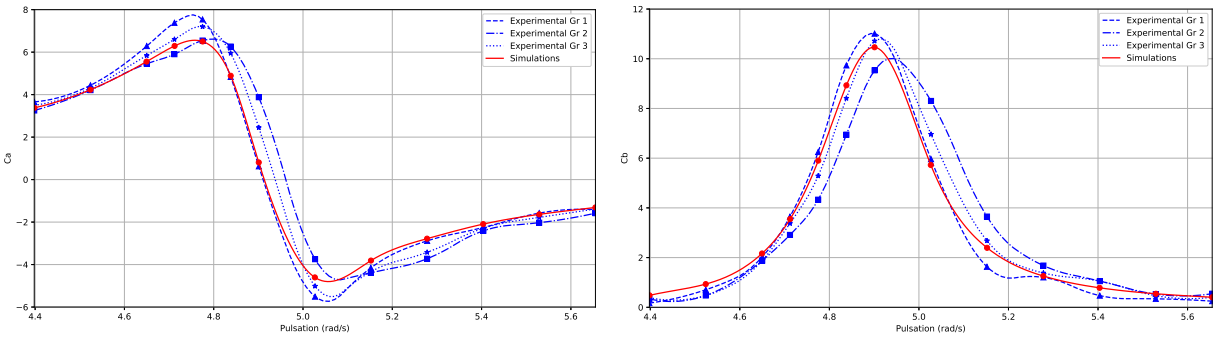


Figure 2.11: Experimental and numeric results, $A = 1mm$, $h = 26.8cm$, Sloshing tests

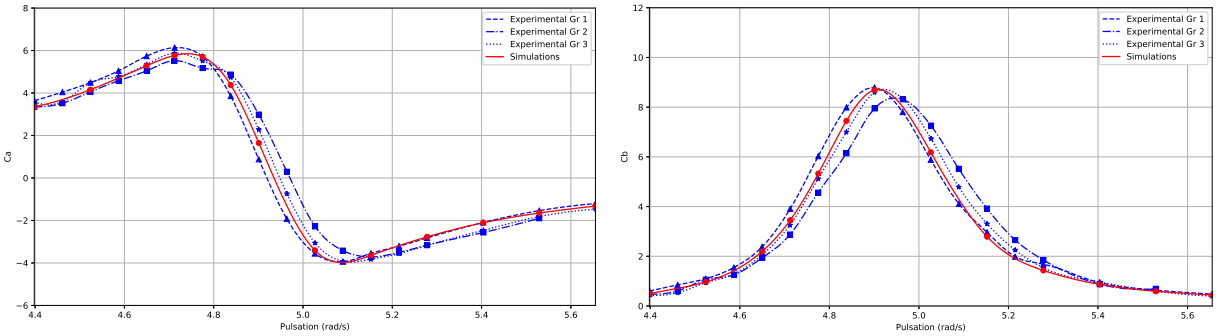


Figure 2.12: Experimental and numeric results, $A = 2mm$, $h = 26.8cm$, Sloshing tests

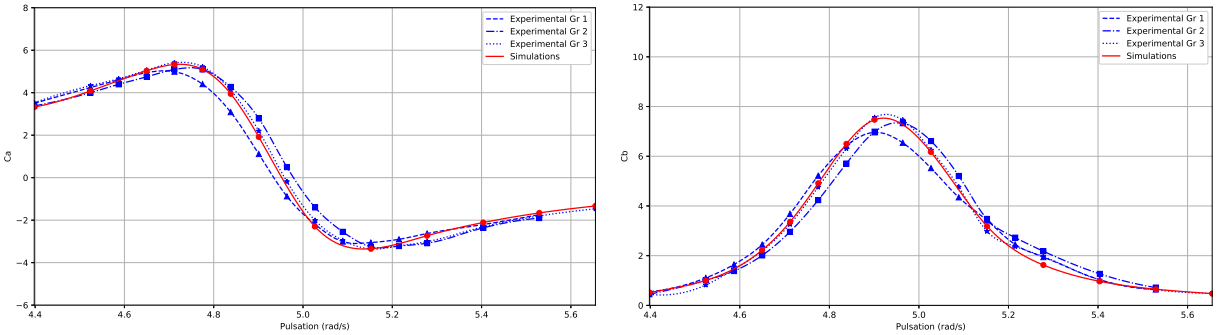


Figure 2.13: Experimental and numeric results, $A = 3mm$, $h = 26.8cm$, Sloshing tests

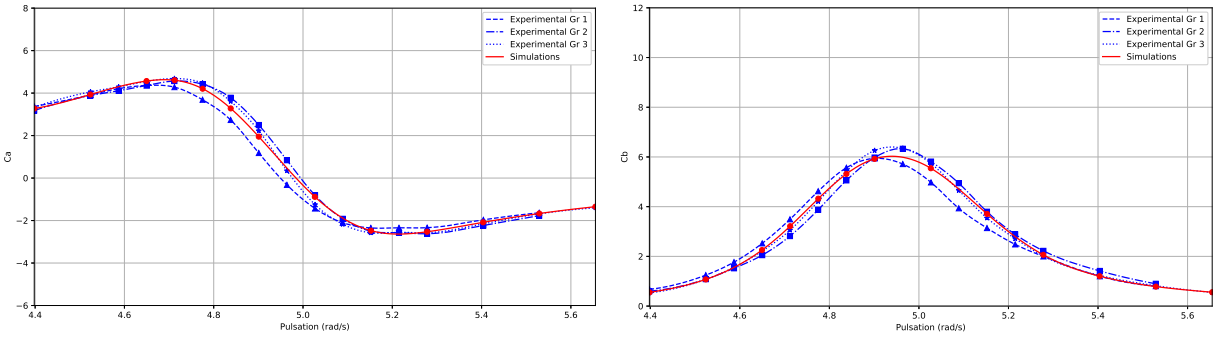


Figure 2.14: Experimental and numeric results, $A = 5mm$, $h = 26.8cm$, Sloshing tests

If we now look at the results for the higher water depth $h = 40cm$, the proposed expressions are still valid (see figures 2.15, 2.16 and 2.17). Nevertheless, we observe small discrepancies at the resonance.

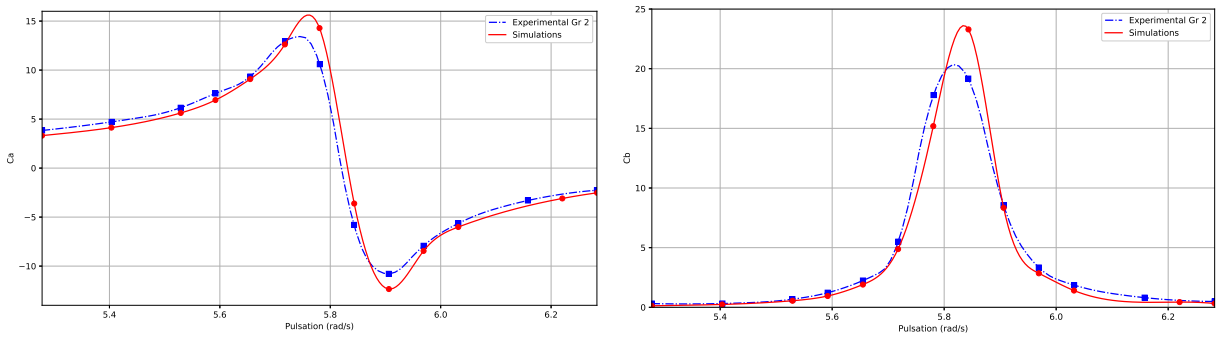


Figure 2.15: Experimental and numeric results, $A = 1mm$, $h = 40.0cm$, Sloshing tests

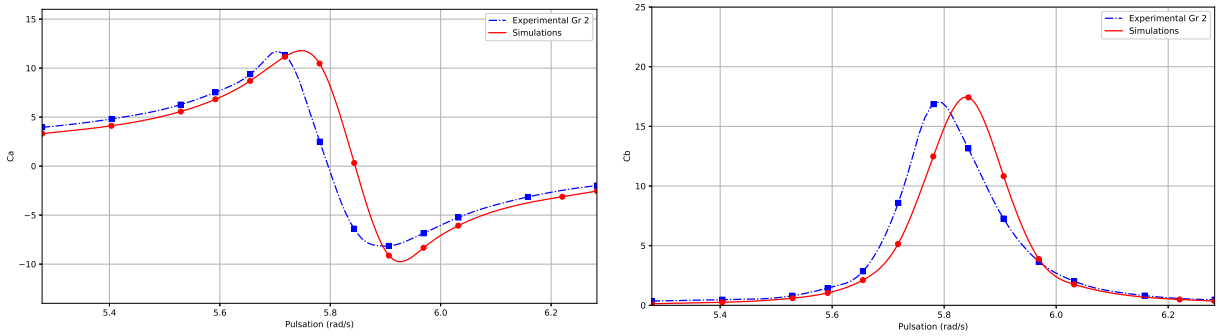


Figure 2.16: Experimental and numeric results, $A = 2mm$, $h = 40.0cm$, Sloshing tests

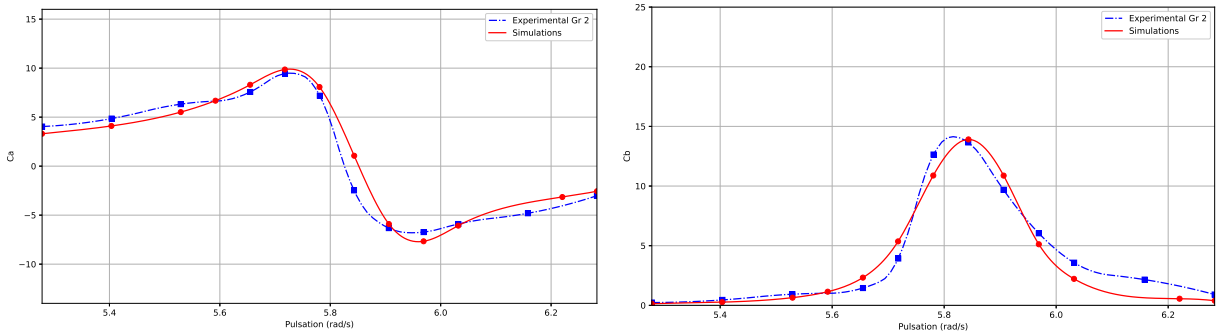


Figure 2.17: Experimental and numeric results, $A = 3mm$, $h = 40.0cm$, Sloshing tests

## 2.5 Discussions

Now, the question is : are these new expressions exportable to others situations with different flow characteristics ?

### 2.5.1 Flow characteristics

First of all, let's start by looking at the values of the adimensional numbers. The ranges of these values for every sloshing test is given in table Tab. 2.2. The values of Ursell numbers are a little overestimated because we use $h = 26.8cm$ and $h = 40.0cm$ to compute them (the porous medium is not taken into account).

| Water depth h | $A$ | $R_e$ | $F_o$ | $KC$ | $\beta_S$ | $U_r$ |
|---|---|---|---|---|---|---|
| 26.8cm | 5mm | 1666–5568 | 0.32–1.07 | 1.42–4.20 | 1176–1513 | 0.04–0.17 |
| 26.8cm | 3mm | 988–3927 | 0.19–0.75 | 0.84–3.00 | 1176–1513 | 0.03–0.12 |
| 26.8cm | 2mm | 655–2913 | 0.13–0.56 | 0.56–2.22 | 1176–1513 | 0.02–0.080 |
| 26.8cm | 1mm | 326–1665 | 0.06–0.32 | 0.28–1.27 | 1176–1513 | 0.01–0.06 |
| 40.0cm | 3mm | 932–8355 | 0.18–1.62 | 0.66–5.34 | 1412–1681 | 0.02–0.09 |
| 40.0cm | 2mm | 615–6526 | 0.12–1.26 | 0.44–4.17 | 1412–1681 | 0.01–0.084 |
| 40.0cm | 1mm | 304–4040 | 0.06–0.78 | 0.22–2.59 | 1412–1681 | 0.01–0.05 |

Table 2.2: Adimensional numbers, Sloshing tests

From Burcharth & Andersen (1995) criterion ($R_e > 300$), the flow for our tests is fully turbulent. However, with Gu & Wang (1991) criterion ($R_e > 1000$), part of the tests correspond to the transition between laminar and turbulent.

In term of $KC$ number, values are small, less than 5.3. So, the flow through the porous media are not necessarily separated even though the Reynolds number exceeds the criterion for turbulent flow of Burcharth & Andersen.

This may explain, for the tests with $h = 26.8cm$, why the laminar part of the dissipation is higher than the turbulent part ($F_o << 1$) outside the resonance. At the resonance, the viscous and turbulent efforts theoretically divide equally ($F_o \approx 1$). This emphasises the advantage of the Forchheimer number compared to the Reynolds number.

The range of Stokes parameter $\beta_S$ is quite constant ($1100 < \beta_S < 1700$). The periods of tests do not vary much. These values show that the flow can be considered a little more inertial than laminar. The third term $c\frac{\partial v_d}{\partial t}$ of the extended equation of Forchheimer (Eq. 4.5) also plays an important role here.

These sloshing tests place themselves in the *FINE GRAVEL* region of figure 4.3 proposed by Gu and Wang (1991), in the transition zone. The three kinds of resistances, laminar, turbulent and inertial are all to be considered. The tests performed by Smith (1991) and Van Gent (1993, 1995) in U-tube water tunnels were located a little further from the laminar zone.

### 2.5.2 Evolution of the inertia parameter : a simple case

In order to better understand our formulation with regards to the inertia parameter, we propose to consider a simple case : a smooth cylinder in uniform oscillatory flow positioned far from the free surface and the bottom of the tank.

#### Inertia coefficient $C_M$

In Bougis (2015) [3], we learn that $C_M = 1 + C_a$ strongly depends on Keulegan-Carpenter number $KC$. The figure 2.18 shows the evolution of $C_M$ function of $KC$ for a smooth cylinder in an uniform oscillatory flow positioned far from the free surface and the bottom. We observe the following points :

1. When $KC$ tends towards 0, $C_M$ tends asymptotically to 2, with a slight overshoot. The coefficient of inertia admits the following asymptotic expansion :

$$C_M = 2 + \frac{4}{\sqrt{\pi\beta_S}} + O\left(\frac{1}{\sqrt{\beta_S}}\right) \tag{2.20}$$

2. $C_M$ decreases linearly until $C_M$ admits a minimum for $KC$ of the order of 10 to 15. $C_M$ values can be less than unity for Stokes parameters less than 2500 ($C_a$ admits negative values).

3. $C_M$ tends to a constant value when $KC$ becomes large enough. This means that for a given period, beyond a minimum value of $KC$, the amplitude of the oscillations has no more influence on the value of the inertia force.

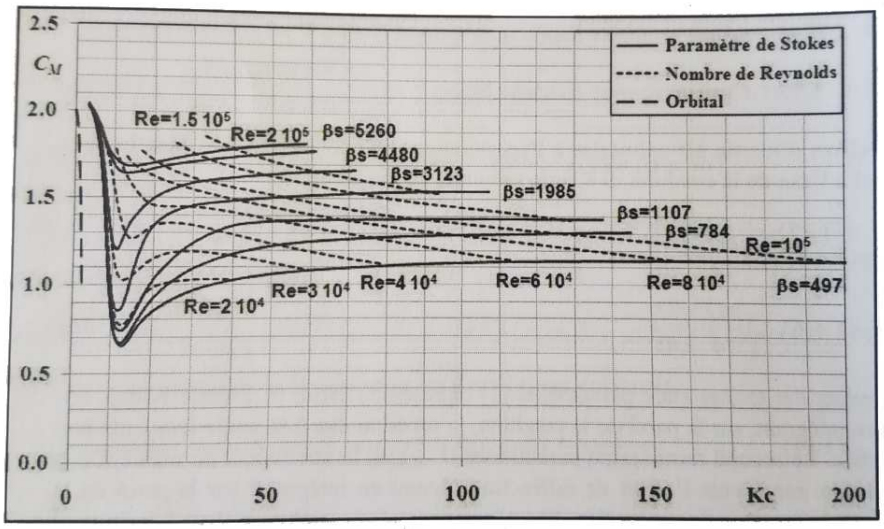


Figure 2.18: $C_M$ of a smooth cylinder function of $KC$ and $\beta_S$, Sarpkaya et Isaacson [3], Sloshing tests

If we try a comparison with a porous medium, we also find that $C_M$ decreases linearly with $KC$ but for smaller $KC$ numbers ($< 5.4$) instead of $5 < KC < 15$. There are many possible explanations. The inertia coefficient of a simple cylinder depends on its relative distance to bottom or on its roughness. The type of flow also plays a role. In the experimental tests, the flow is not a simple horizontal oscillatory flow . At a low $KC$ number, the vertical velocities are of the same order as the horizontal ones. An orbital flow has major effects on the inertia coefficient of a cylinder when $KC$ is small. It corresponds to the "orbital" curve in figure 2.18. The effect of orbital trajectory works as though the curves were shifted towards smaller $KC$-values.

Only small ranges of $R_e$-values, $KC$-values and $\beta_S$-values were investigated through sloshing tests. As we see in figure 2.18, the inertia coefficient also depends on $R_e$ and $\beta_S$ which makes it difficult to propose an universal law in this context.

### 2.5.3 Conclusion

Sloshing tests were very instructive. First, we find that at low-KC flows, the inertial dissipation plays a major role. This is necessarily transferable to problems of reflection-transmission coefficients of a porous structure submitting to waves. Having a good dissipation rate is not enough to reproduce the correct hydrodynamic behaviour. Reflection may be overestimated and transmission underestimated or the opposite. At low KC flow, both parameters, resistance $(a, b)$ and inertial $c$ ones have to be adjusted.

For the resistance coefficients ($a$, $b$), we find another couple of parameters ($\alpha = 2950$, $\beta = 0.3$) deduced from Burcharth and Andersen (1995) [4] equations. The criterion for turbulent flow $R_e > 300$ is not suitable for our tests. The limit is for higher Reynolds numbers.

Concerning the inertia coefficient $C_M$, we show that it presents the same shape as a simple cylinder at very small $KC$-values. $C_M$ is decreasing with $KC$.

# 3 SECOND CAMPAIGN : VINTIMILLE

## 3.1 Context of project

The operating company of Monaco harbour acquired the *Cala del Forte* port concession in Ventimiglia (Fig. 3.1). The initial project for this harbour was designed for small boating. Unfortunately the construction was stopped before this was achieved. The Ventimiglia port *Cala Forte* provides numerous posts for pleasure craft and mega-yachts, including a "longside" berth along the main dike. This post will receive a 70m long mega-yacht (Fig. 3.2).

Figure 3.1: State of the port before further constructions, Vintimille

The post is delimited by a 30m long groyne, perpendicular to the main dike. It is a vertical structure of particular design, consisting of rocks caged by a metal framework or by slightly spaced piles. The structure has the advantage of occupying a small footprint, compared to a conventional rubble-mound groyne. It is also compatible with mooring yachts. On one side of the pass, the 70m long yacht is moored longside. And on the other side, 30 to 45m long yachts are moored perpendicular to the main dike (Fig. 3.2).

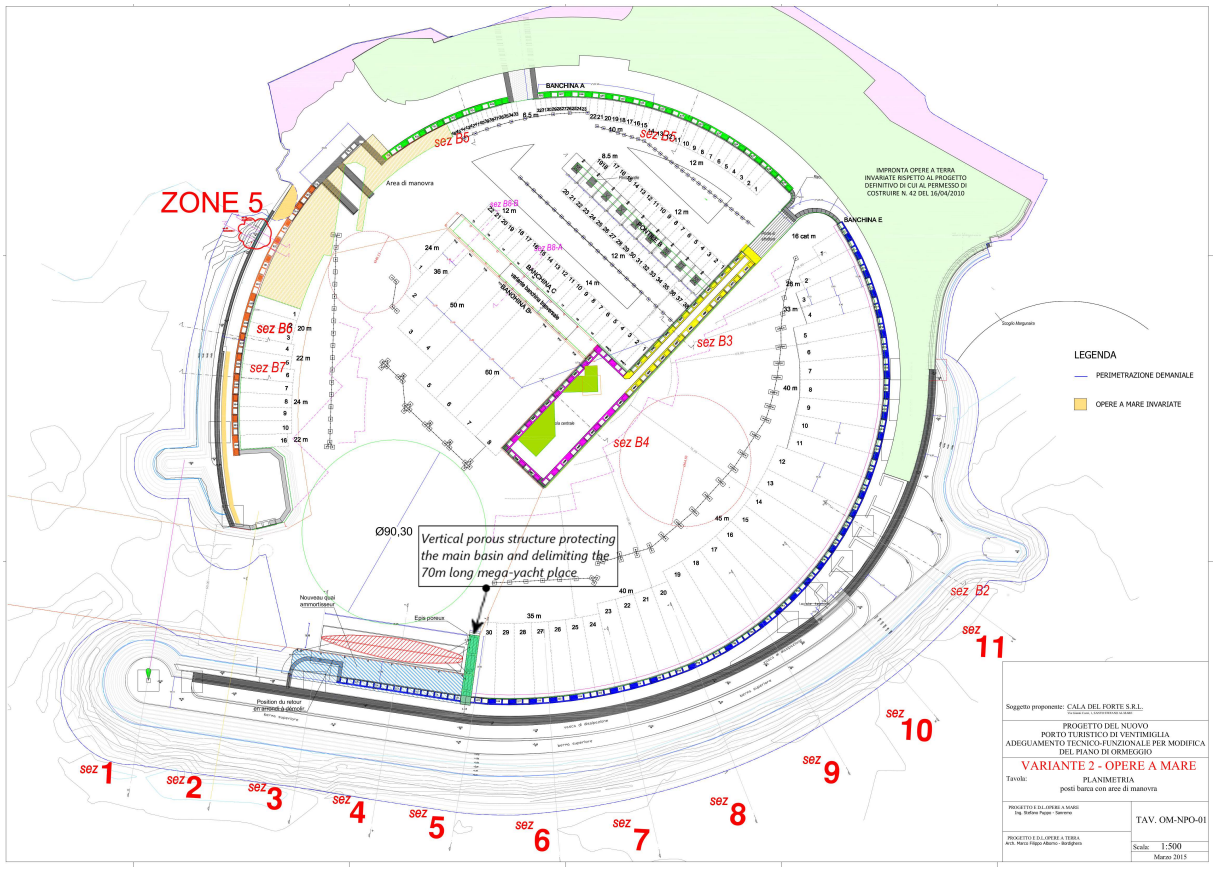


Figure 3.2: Ground plane, Vintimille

The vertical breakwater dissipates energy of the incident waves and partially protects the mooring area along the main dike. It also has the advantage of promoting local biodiversity through the wall of natural crevices presented by the stack of rocks.

The objective of this study was to optimise the hydrodynamic performance of the upright riprap breakwater, which must provide sufficient protection for moorings of the 30 to 45m long yachts in the downstream zone. The objective is also to limit reflections towards the 70m longside station, even if the megayacht may more easily accept a relatively high agitation.

Small-scale tests were conducted to meet the following objectives :

- Evaluate the hydrodynamic performance of the vertical rock structure. The acquired data are used to test and validate the diffraction code again. We finally take advantage of the code to extend the characteristics of the structure for longer waves (not described here).
- Modify the setup by adding a vertical plate at the back face of the structure. Two configurations are considered : with a full plate or a porous plate.

## 3.2 Similarity and scale factors

By choosing to keep constant the Froude number, the proportion of the main forces applied to a fluid in turbulent flow are preserved at the same time. So we have to pay attention that the flow stays turbulent while scaling the rocks. The choice of the scale has been adjusted to the following constraints :

- To respect the turbulent state of the flow inside the porous medium, even for the relatively low wave heights encountered in the port. We observed $H_s = 25cm$ to $100cm$ for frequent sea states upstream of the groyne.
- To be compatible with the wave tank dimensions and the wave maker characteristics.

For reliable measurements over a wide range of periods $T = [3s - 12s]$, a scale of $\frac{1}{40}$, generally adopted in coastal engineering, would have been suitable. Nevertheless, it is important here to reproduce the reflection and the

transmission of energy through a dissipative medium receiving a turbulent flow. Therefore, our choice was on a larger scale $\frac{1}{20}$, with the aim of identifying the effects of transmission over a smaller range of periods $T = [2-9s]$, with a better confidence in the analyses.

## 3.3 Experimental set-up

The small-scale tests were conducted at the wave tank of *Ecole Centrale de Marseille*, for a duration of two weeks. The water depth at the foot of the structure is about $h_0 = 7.6m$ (real-scale), which corresponds to $h = 38cm$ at the test-scale.

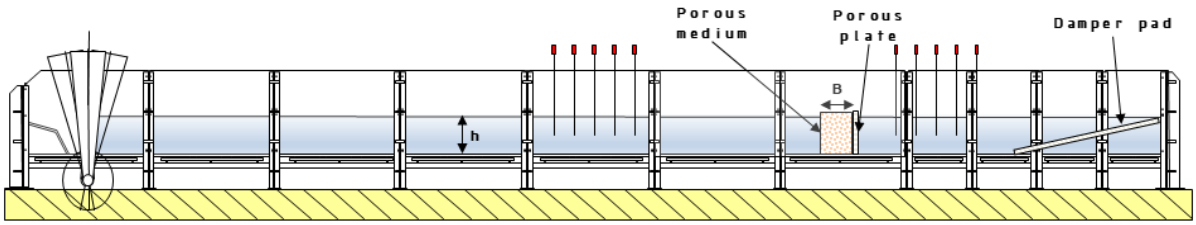


Figure 3.3: Schematic cross-section of the wave tank with scale model of Vintimille

### 3.3.1 Scale-model of the structure

The scale-model is representative of a section of the upright riprap structure. One of the basic sections is illustrated in figure 3.4.

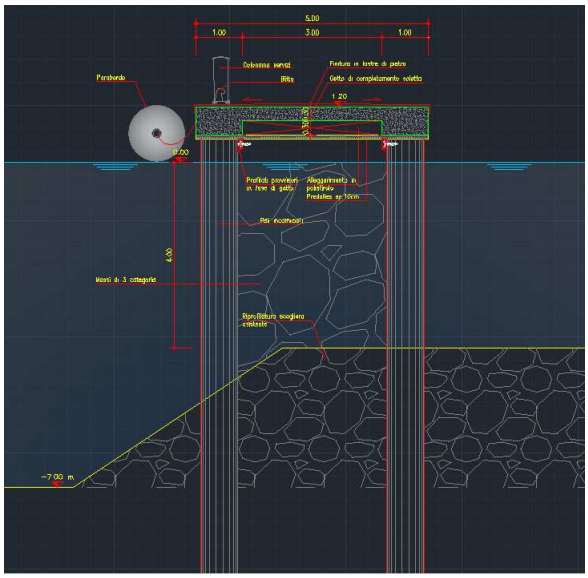


Figure 3.4: Section of the verticalized stone groyne, Vintimille

The structure is 5m wide, with an inner area of 3m for the caged riprap. The diameter of the piles is 0.8m. Several solutions are possible in order to contain the blocks. The sketch below proposes a system of spaced piles, on which links are fixed (Fig. 3.3.1). The use of sufficiently tight piles (gap of about 50cm between piles) to maintain the blocks is a possible alternative.

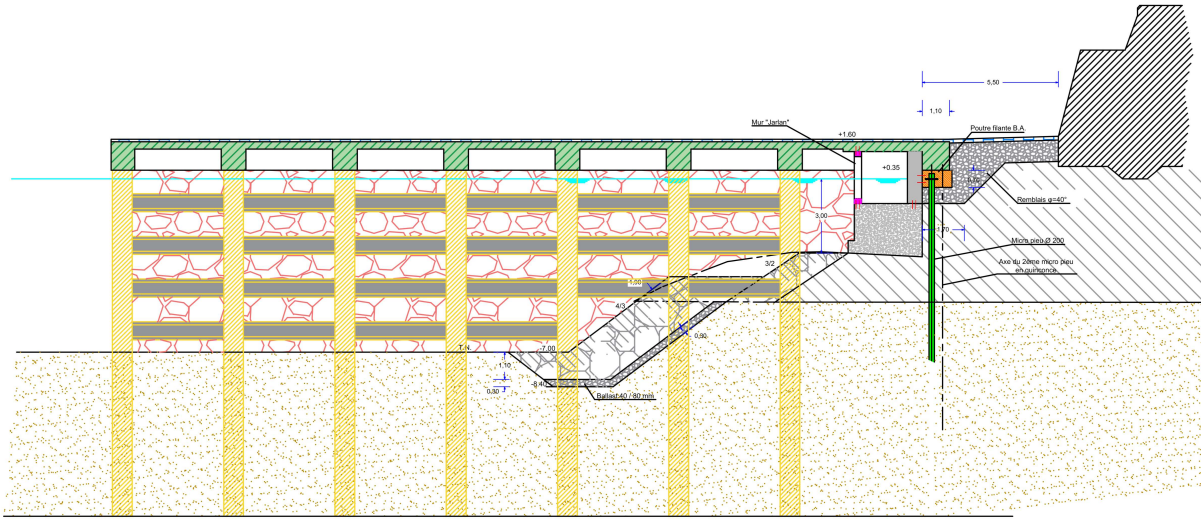


Figure 3.5: Elevation view. Staggered piles with intermediate links, Vintimille

The yellow structure of the scale-model built for the tests of Banyuls-sur-Mer and Istres (Chap. 3.4) was reused but, in this case, the stones are constrained by simple vertical metal rods. The system of piles, more or less spaced, with or without links, is not represented. Compared to the effective width of caged rock, the presence of piles has a minimal impact on the overall hydrodynamic behaviour. They achieve very little dissipation.

The model could be modified in its downstream part by inserting a porous or not porous plate. The figures 3.6, 3.7 and 3.8 illustrate the three setups, with successively : without a plate, with a plate of porosity $n = 5\%$ and with a solid plate.

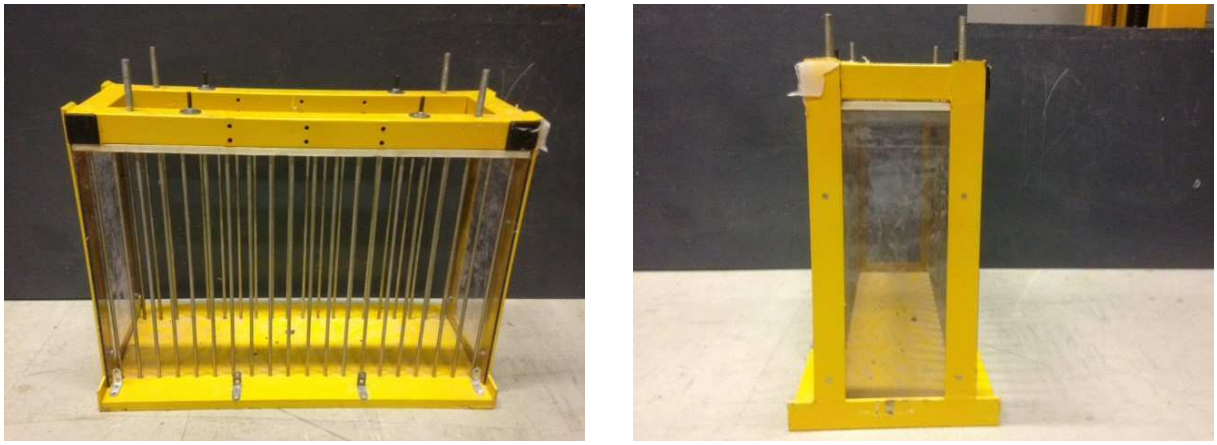

Figure 3.6: Empty cage, Vintimille

Figure 3.7: With a porous plate at the back face, Vintimille

Figure 3.8: With a solid plate at the back face, Vintimille

The three configurations have been tested and compared in terms of hydrodynamic performances :

- The simple groyne, filled with vertical stones.
- The same structure with a downstream sealed plate, so as to prevent any downstream energy transfer.
- The same structure, with a slightly perforated plate (porosity $n = 5\%$), partially transmitting energy downstream.

### 3.3.2 Rock description

Stones were weighed one-by-one before being laid, also one-by-one (akin to the real-scale process conducted by a crane), in the vertical cage. The curve of size distribution is given in Appendix B for the distribution of the stones used in this experimental test. The table below summarises the essential values.

| **Percentile** | **Mass M** | **Nominal diameter $d_n$** | **Porosity** |
|---|---|---|---|
| 15% | 48g | 2.6cm | 45.0% |
| 50% | 69g | 3.0cm | |
| 85% | 94g | 3.3cm | |
| **Coefficient of uniformity $n_{RR}$** | 4.4 | 13.2 | N/A |

Table 3.1: Size distribution, Vintimmille

### 3.3.3 Summary of the test parameters

The different test parameters are summarised below :

- The test scale is 1/20th.
- The water depth is h=38cm.
- The dimensions of the model at this scale are :
  - Height : 41cm (between -7m LMM and 1.2m LMM).
  - Width : 15cm (3m wide).
  - Length : 65cm (13m long of the groyne)
- Porous medium characteristics are :

- Porosity 45.0%
- $d_{n50} = 3.0cm$, $d_{n85}/d_{n15} = 1.25$ (narrow size distribution), $n_{RRd_{n50}} = 13.2$

- The generated incident waves are :
  - H=[12.5mm, 25.0mm, 50.0mm]
  - T=[0.45s 0.67s 0.89s 1.34s 1.79s 2.10s]

The table 3.2 summarises the wave characteristics that are also reported in the diagram of Le Mehauté (1976) on the applicability of wave theories (Fig. 3.9). We notice that only the tests with the smallest amplitude $A_i = 6.25mm$ and $T \geq 0.89s$ are inside or close to the range of the linear wave theory. The others performed waves for $T \geq 0.89s$ are better described by the Stokes 2nd order wave theory.

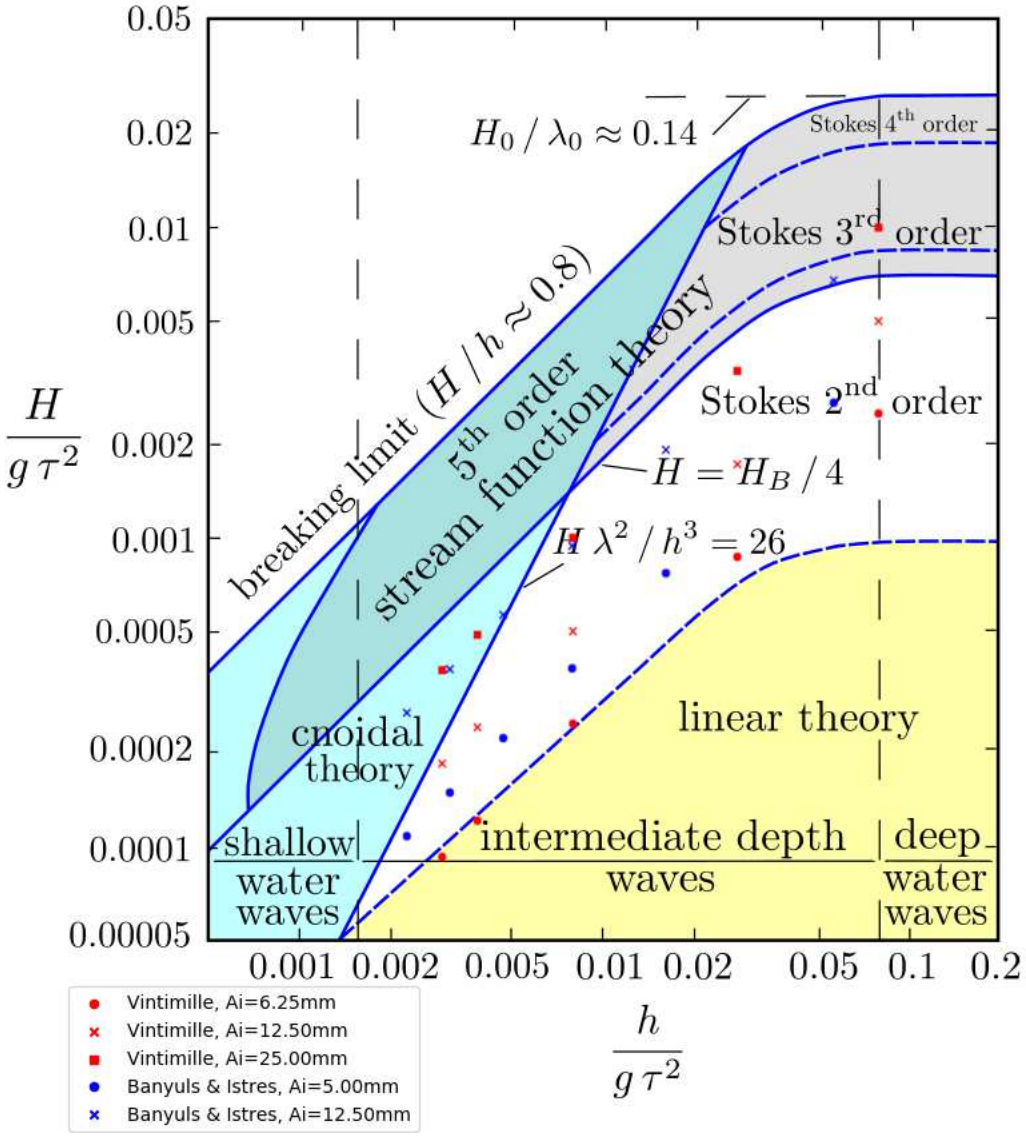


Figure 3.9: Applicability of wave theories, Le Mehauté (1976)

| | | Wave period $T$ | | | | | |
|---|---|---|---|---|---|---|---|
| **Amplitude $A_i$** | **Variable** | **0.45s** | **0.67s** | **0.89s** | **1.34s** | **1.79s** | **2.10s** |
| 6.25mm | $H/(g\lambda^2)$ | 1.27e-2 | 2.61e-3 | 8.96e-4 | 2.59e-4 | 1.26e-4 | 9.64e-5 |
| | $U_r$ | 3.00e-4 | 1.45e-3 | 4.27e-3 | 1.48e-2 | 3.03e-2 | 3.96e-2 |
| 12.50mm | $H/(g\lambda^2)$ | 2.54e-2 | 5.22e-3 | 1.79e-3 | 5.18e-4 | 2.52e-4 | 1.93e-4 |
| | $U_r$ | 5.77e-4 | 2.82e-3 | 8.20e-3 | 2.84e-2 | 5.83e-2 | 7.62e-2 |
| 25.00mm | $H/(g\lambda^2)$ | 5.18e-2 | 1.44e-2 | 3.58e-3 | 1.36e-3 | 5.04e-4 | 3.86e-4 |
| | $U_r$ | 1.15e-3 | 5.64e-3 | 1.64e-2 | 5.68e-2 | 1.17e-2 | 1.52e-1 |
| - | $h/(g\lambda^2)$ | 3.87e-1 | 7.92e-2 | 2.72e-2 | 7.90e-3 | 3.80e-3 | 2.90e-3 |

Table 3.2: Wave characteristics of experimental tests, Vintimille

## 3.4 Comparisons between numerical and experimental results

The reflection and the transmission coefficients of experimental tests are measured thanks to Andersen's method (2017) [39]. The experimental results are compared with the numerical models *Diffra3D*, *Wave2Foam* and with the analytical model of Madsen & White (1976) previously presented.

Before the comparisons, we need to fix the parameters that describe the porous medium in the numerical models. We compare two selections of parameters :

1. Selection 1

   The resistance coefficients used to describe the porous medium of the structure are those highlighted in the sloshing tests, $a = 2950$ and $b = 0.3$. With this couple, the inertia coefficient $C_M$ is optimised, as in the sloshing campaign, by minimising the RMS error defined as :

   $$\epsilon(T) = \sqrt{\frac{(R_c - R_m)^2}{R_m^2} + \frac{(T_c - T_m)^2}{T_m^2}} \tag{3.1}$$

   where T is the period, $R_m$ and $T_m$ corresponds to values of measured reflection and transmission coefficients. $R_c$ and $T_c$ are the computed values.

   This optimisation is performed to verify that the evolution of the inertia coefficient as function of the period is similar to the previous results.

2. Selection 2

   The values of $\alpha = 500$, $\beta = 2$ and $C_M = 1.8$ are used. $\alpha = 500$ and $\beta = 2$ correspond to the values proposed by B. Jensen et al. (2014) [25] after steady flow experimental tests (see section 1.4.4.2). $C_M = 1.8$ corresponds to the coefficient $\gamma_p = 0.34$ suggested by Van Gent (1993) [59], see section 1.4.4.1).

The figures in the following results section abide by the legend summarised here:

- Experimental data : blue
- *Diffra3D* + Selection 1 : red
- *Diffra3D* + Selection 2 : purple
- *Wave2Foam* + Selection 1 : green
- Analytical model + Selection 1 : orange

The results of the model *Wave2Foam* are only available for the simple porous case without plate for $A_i$ = 12.5$mm$ and $A_i$ = 25.0$mm$, $T \geq 0.67s$. The smallest amplitude $A_i = 5.62mm$ requires a very important refinement of the mesh at the level of the free surface in order to catch the transmitted waves. The smallest period $T = 0.45s$ also requires a very thin mesh in the horizontal direction. The VOF model requires at least 20 to 30 cells per amplitude and 30 to 50 cells per wavelength. The calculation time on a machine with over 60 cores lasts more than a few days for the smallest period. This constraint demonstrates the difficulty of using VOF method to model small wavelets (small amplitude and small period) commonly found in ports.

### 3.4.1 A simple porous medium

The first configuration corresponds to the porous structure without plate (see figures 3.6 and 3.10 for the models).

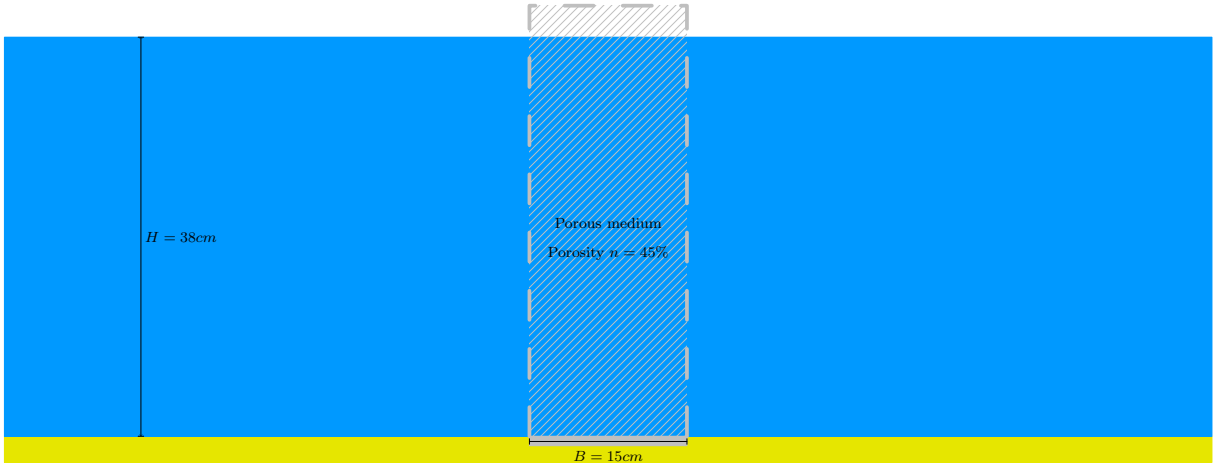


Figure 3.10: Geometry, Simple porous medium, Vintimille

**Discussion on $C_M$**

The figure 3.11 shows the RMS error function of $C_M$ for $A_i = 6.25mm$. The minimum are indicated by dots on the figure. These dots correspond to the chosen values of $C_M$.

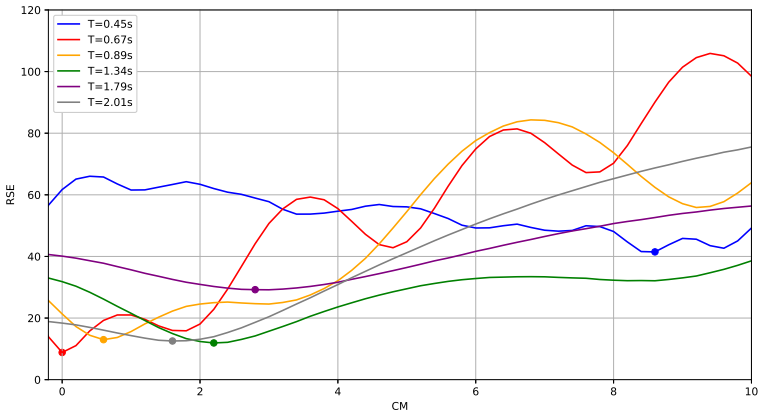


Figure 3.11: RMS, $A = 6.25mm$, Simple porous medium, Vintimille

The values of the inertia coefficient $C_M$ function of the periods for the three wave heights are presented in figure 3.12. The figures 3.13, 3.14, 3.15, 3.16 and 3.17 show the different non-dimensional numbers $R_e$, $F_o$, $KC$, $\beta_S$ and $A_c$ associated with the same tests. The table 3.3 summarises these values.

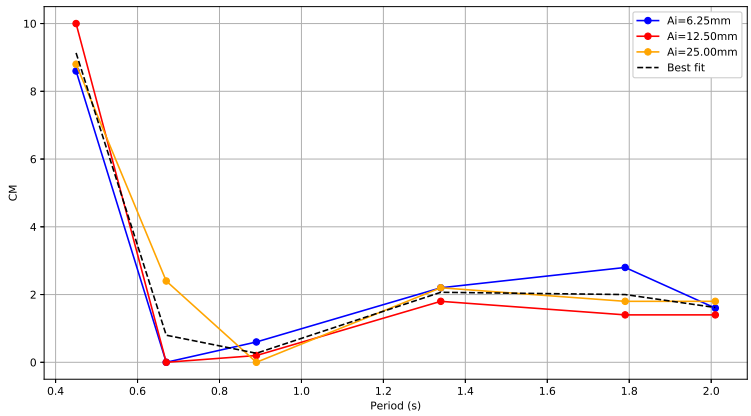


Figure 3.12: Inertia coefficient $C_M$, Simple porous medium

Apart from the first period $T = 0.45s$ and for the smallest amplitude $A_i = 6.25mm$, a fully turbulent flow condition with respect to the Reynolds number ($R_e > 300$) is verified. $KC$ number is increasing over the range of tested periods but stays low ($0.1 < KC < 4$ for $A_i = 6.25mm$ and $0.1 < KC < 12.3$ for $A_i = 25.0mm$).

We observe a decrease of $C_M$ for very little $KC$ numbers (small periods). Then there is a second part where $C_M$ increases until it becomes stable. $C_M = 1.8$ for higher KC-numbers (larger periods) is the value proposed by Van Gent.

It appears that the tendency of $C_M$ is similar to the one of a smooth cylinder in uniform oscillatory flow as in figure 2.18. However $C_M$ is here a function of the period $T$ and not of $KC$. This difference comes from the type of dissipation in these tests. As it was emphasised, the linear part of the dissipation is predominant ($\alpha$ very large compared to $\beta$). Then $C_M$ is not a function of the amplitude.

The inertia coefficient $C_M$ may play an important role in this range of $KC$ numbers. The behaviour of a porous structure may have a strong inertial component for low-KC flows. However, we need to keep in mind that the waves performed for the two smallest periods ($T = 0.45s$ and $T = 0.67s$) can not be well described by the linear wave theory. The wave steepness is too large. Others experimental tests could be performed with constant steepness to confirm this behaviour.

For the simulations with the parameters of Selection 1, we took a best fit of $C_M$ values (the black dashed curve of figure 3.12) as a law for the inertia coefficient.

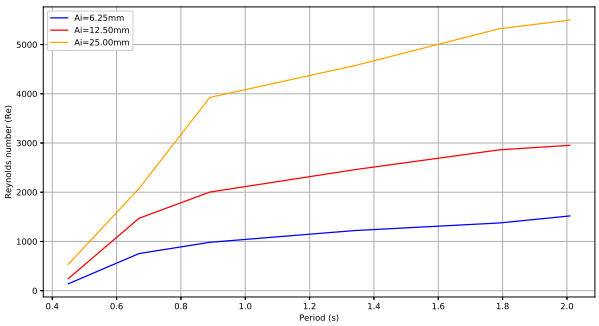


Figure 3.13: $R_e$ number, Simple porous medium

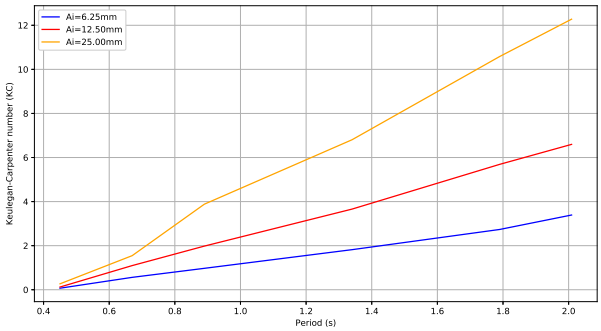


Figure 3.14: $KC$ number, Simple porous medium

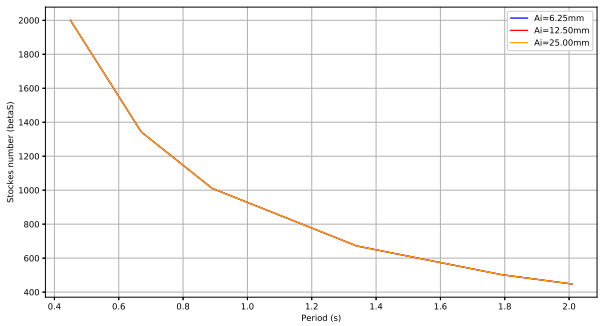


Figure 3.15: $\beta_S$ number, Simple porous medium

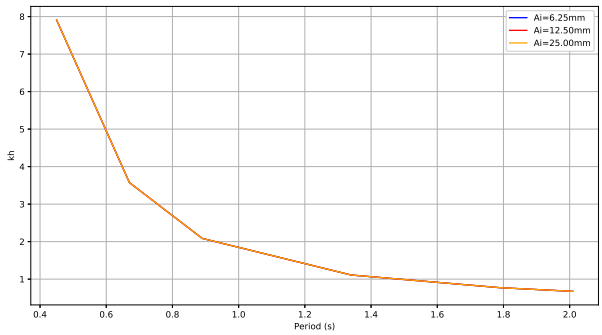


Figure 3.16: $kh$, Simple porous medium

An interesting number to describe the flow in the porous medium can be displayed. This number, the acceleration number $A_c$, is introduced by Van Gent (1995) [60] and defined by :

$$A_c = \frac{\hat{v_p}}{gT} \tag{3.2}$$

According to Van Gent, the coefficient $\gamma_p$ ($S = \left(1+\gamma_p \frac{1-n}{n}\right)/n$) could depend on this non-dimensional number as $\gamma_p = 0.85 - 0.015/A_c$. $\gamma_p$ increases when $A_c$ increases. In our case, there are also some interesting features to observe. The inflexion point on the $C_M$ curve corresponds to the one of the $A_c$ number. $C_M$ decreases when $A_c$ increases. A theoretical law has not been found because $A_c$ number is a very small number ($< 0.015$ here) which makes it difficult to establish coefficients.

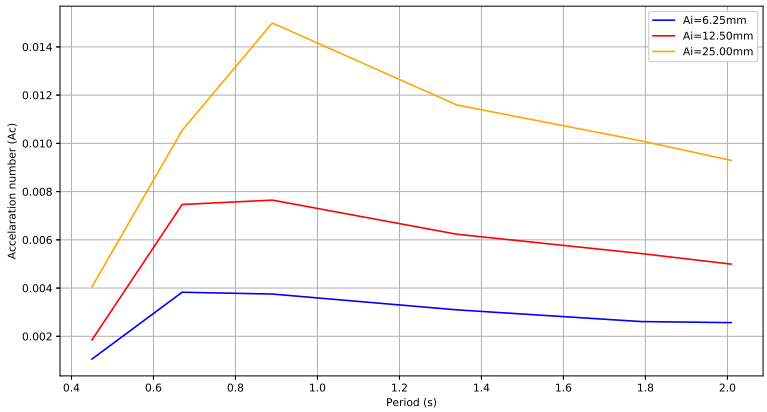


Figure 3.17: $A_c$ number, Simple porous medium

| **Simple porous medium** | | | | |
|---|---|---|---|---|
| $A_i$ | $R_e$ | $F_o$ | $KC$ | $\beta_S$ |
| 6.25mm | 139–1518 | 0.02–0.28 | 0.07–3.39 | 448–2000 |
| 12.50mm | 244–2953 | 0.04–0.55 | 0.12–6.60 | 448–2000 |
| 25.00mm | 536–5497 | 0.10–1.02 | 0.27–12.3 | 448–2000 |

Table 3.3: Simple porous medium, Adimensional numbers, Vintimille

**Hydrodynamic coefficients**

The results of the experimental versus numerical tests for the reflection and transmission coefficients are presented for the three amplitudes A=[6.25mm, 12.50mm, 25.00mm] and for the range of periods T=[0.45s 0.67s 0.89s 1.34s 1.79s 2.01s] in figures 3.18 to 3.23.

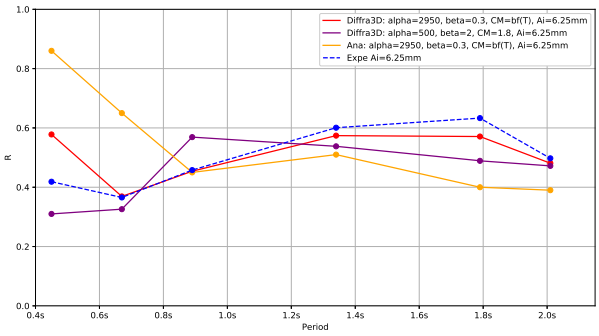


Figure 3.18: Reflection curve, Ai=6.25mm

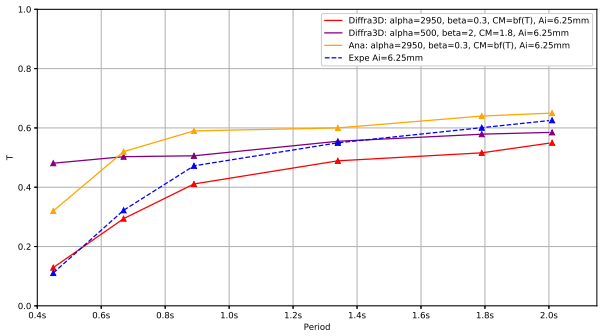


Figure 3.19: Transmission curve, Ai=6.25mm

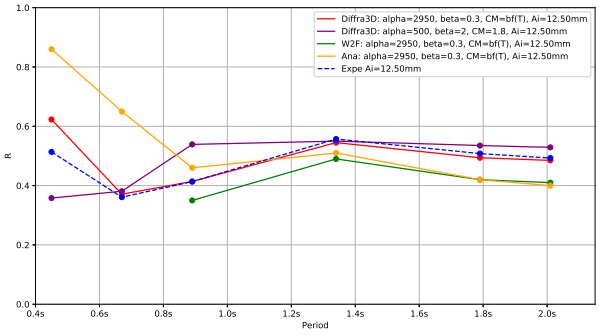


Figure 3.20: Reflection curve, Ai=12.5mm

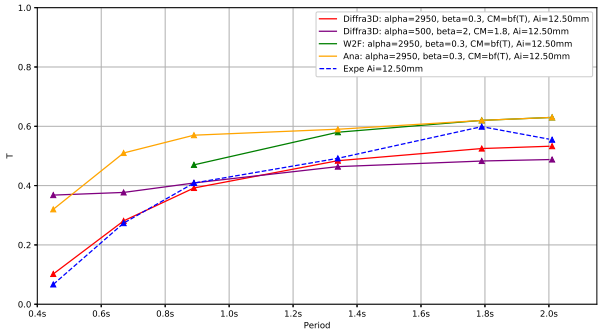


Figure 3.21: Transmission curve, Ai=12.5mm

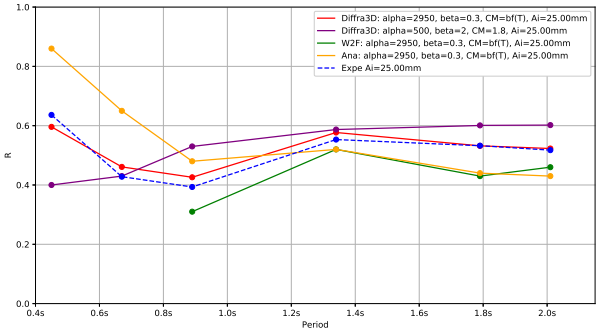


Figure 3.22: Reflection curve, Ai=25.0mm

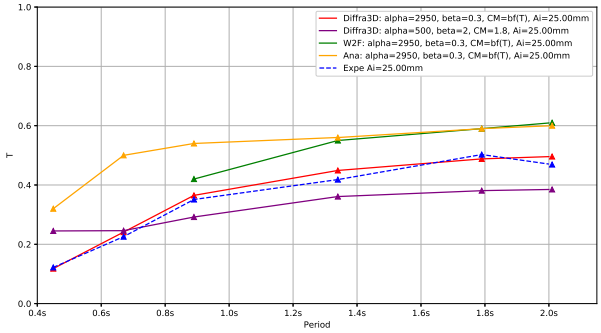


Figure 3.23: Transmission curve, Ai=25.0mm

The experimental hydrodynamic coefficients are commonly found values. The porous structure is more effective when the amplitude of the incident waves is high. The range of reflection is from $R = 40\%$ to $R = 60\%$. The transmission is increasing with the period of incident waves. The higher the periods are, the higher the transmission is. The transmission reaches a maximum of about $T = 60\%$ for high periods.

The numerical results from *Diffra3D* with parameters of Selection 1 (in red) correspond well with the experiment results. The behaviour for the smallest period $T = 0.45s$ is well reproduced. We also notice that this couple of parameters give lower values of the reflection and the transmission for $A_i = 6.25mm$ and $T > 0.45s$. On the contrary, for $A_i = 25mm$, it gives values a little higher.

The parameters of Selection 2 (in purple) also perform well for $T > 0.89s$ but are less accurate. It overestimates the transmission for the smallest period $0.45s$.

*Wave2Foam* (in green) with the parameters of Selection 1 gives the good trend for reflection and transmission. It underestimates the reflection and overestimates the transmission. The dissipation rate corresponds well.

The simple analytical model (in orange) gives large values for the transmission. The refection is good for $T > 0.67s$. For the smallest periods, the reflection and the transmission are really too large. It shows the limits of the analytical model based on long wave theory.

A transmission level of $T > 40\%$ is anyway not acceptable for the future vertical porous breakwater of Vintimille harbour. The main objective is to protect the mooring places located behind, all along the main dike. This configuration was not chosen. The configurations with a solid plate and a porous plate have then been tested.

### 3.4.2 A porous medium with a solid plate

Setting a solid plate at the back of the porous structure prevents all transmission. This next configuration is described below in figure 3.24.

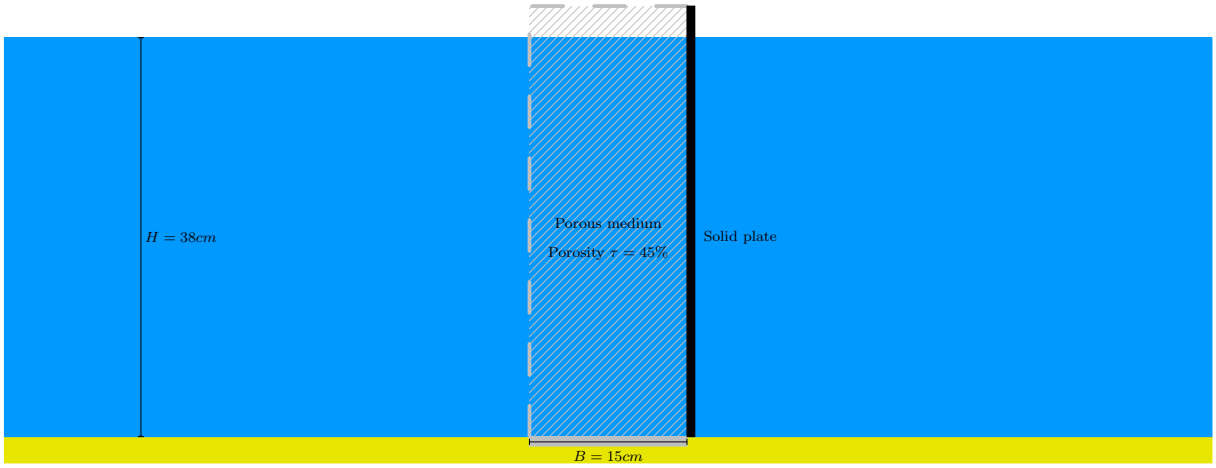


Figure 3.24: Geometry, Porous medium with a solid plate behind, Vintimille

**Discussion on $C_M$**

When these tests are compared to the *Diffra3D* model with $C_M$ set as previously, the results for larger periods are not satisfying. Then, as in the previous section, we have performed a new optimisation for $C_M$. Figure 3.25 shows the evolution of the optimised inertia coefficient $C_M$ depending on the period. The parameters of Selection 1 are used ($\alpha = 2950$, $beta = 0.3$). For $KC$ numbers lower than 1.4, we observe the same tendency as previously. However, for the first period $T = 0.45s$, $C_M$ is a function of the amplitude. For $KC$ numbers larger than 1.4, the inertia coefficient increases and differs from the previous case where $C_M$ were constant.

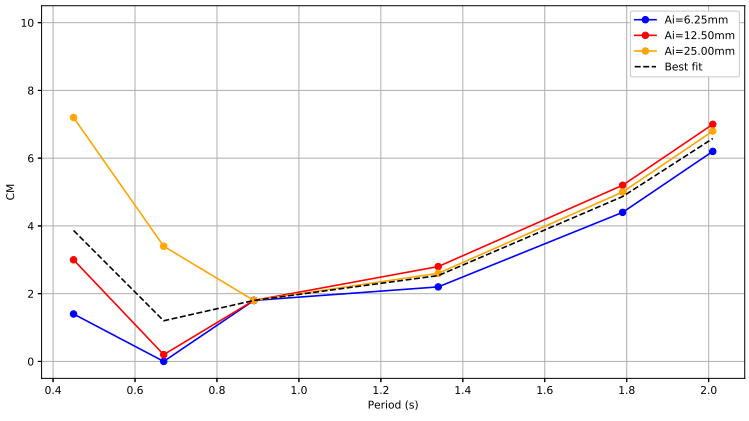


Figure 3.25: Inertia coefficient $C_M$, Porous medium with a solid plate

A study of Riaan van't Veer & Alessio Pistidda (2012) [61] proposes a comparison (Fig. 3.26) of the inertia coefficient $C_M$ for a wall-bounded plate with published data from Sarpkaya & O'Keefe (1996). The inertia coefficient of a free cylinder from Keulegan & Carpenter (1958) is also added for comparison. From a certain value of $KC$, the inertia coefficient of a wall-bounded plate starts increasing significantly. The presence of a solid plate at the back of the porous medium would modify the inertial behaviour of the system for the largest $KC$ numbers. It justifies the fact we use a different best fit (black dashed curve in Fig. 3.25) for CM-values in this case than the one found for a simple porous medium.

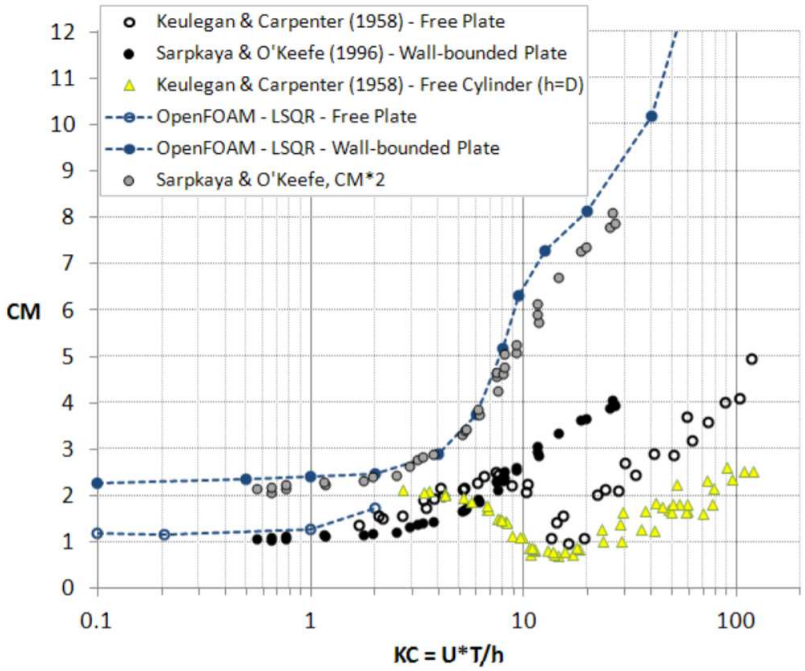


Figure 3.26: Comparison of inertia coefficient for free and wall-bounded plates, Riaan van't Veer & Alessio Pistidda (2012)

The table 3.4 summarises the adimensional numbers of this configuration. They are close to the adimensional numbers computed with a simple porous medium.

| **Porous medium with solid plate** | | | | |
|---|---|---|---|---|
| $A_i$ | $R_e$ | $F_o$ | $KC$ | $\beta_S$ |
| 6.25mm | 337–934 | 0.06–0.17 | 0.17–2.08 | 448–2000 |
| 12.50mm | 510–1978 | 0.09–0.37 | 0.26–4.42 | 448–2000 |
| 25.00mm | 623–3745 | 0.12–0.69 | 0.31–8.36 | 448–2000 |

Table 3.4: Porous medium with solid plate, Adimensional numbers, Vintimille

**Hydrodynamic coefficients**

The results of experimental tests versus *Diffra3D* simulations are presented for the three same amplitudes A=[6.25mm, 12.50mm, 25.00mm] in figures 3.27, 3.28 and 3.29.

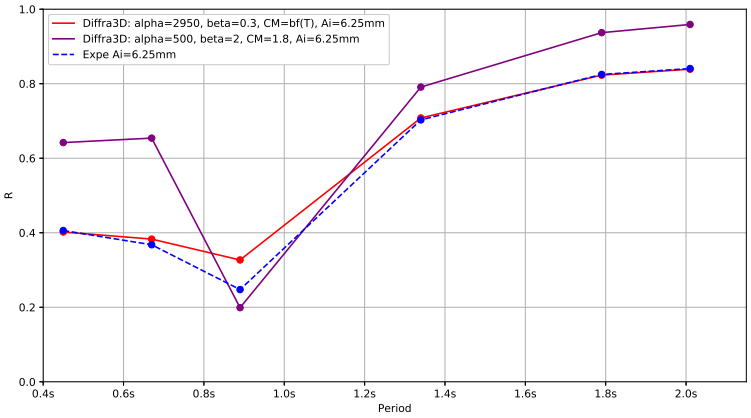


Figure 3.27: Reflection curve, Ai=6.25mm

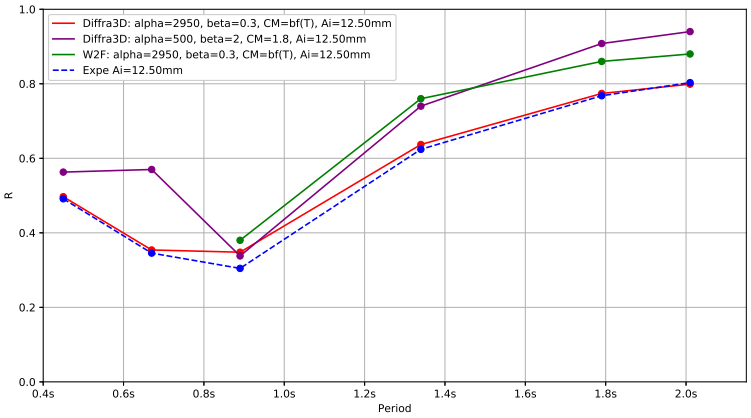


Figure 3.28: Reflection curve, Ai=12.5mm

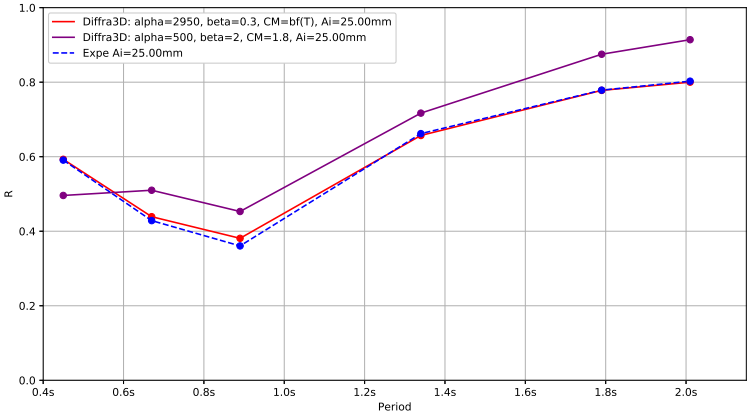


Figure 3.29: Reflection curve, Ai=25.0mm

*Diffra3D* with parameters of Selection 1 gives good comparisons for the three amplitudes. The Selection 2 gives also a good tendency but overestimates the reflection for most cases.

A vertical porous medium with a small width and with a solid plate at the back is a bad damping structure. Little amount of energy is dissipated. The boats behind are well protected but the area in the front of the structure where the 70m long mega-yacht is moored would become too much agitated. An intermediary solution is needed and tested by adding a porous plate instead of a solid one.

### 3.4.3 A porous medium with a porous plate $\tau = 5\%$

The plate installed at the back of the porous structure is slightly porous with a porosity value of $\tau = 5\%$. The figure 3.30 shows this configuration.

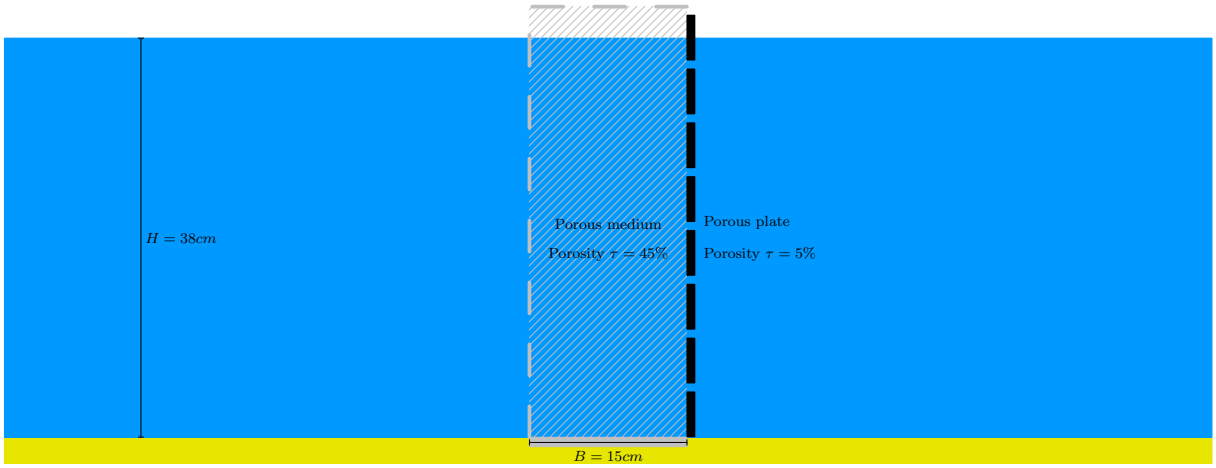


Figure 3.30: Geometry, Porous medium with a porous plate ($\tau = 5\%$) behind, Vintimille

**Discussion on $C_M$**

This configuration is between the two previous configurations : simple porous medium without a solid plate and with a solid plate. The values of $C_M$ for the Selection 1 are then chosen as the average of the values of the two previous configurations (see the black curve in figure 3.31).

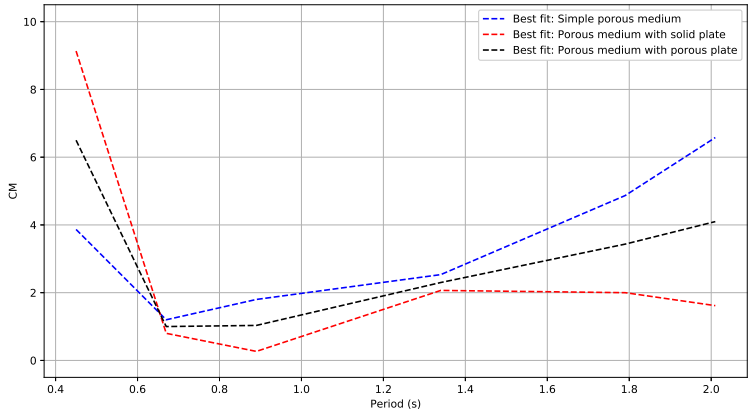


Figure 3.31: Inertia coefficient $C_M$, Porous medium with a porous plate

The table below gives the adimensional numbers for this set of experiments.

| **Porous medium with porous plate** | | | | |
|---|---|---|---|---|
| $A_i$ | $R_e$ | $F_o$ | $KC$ | $\beta_S$ |
| 6.25mm | 176–1020 | 0.03–0.19 | 0.09–2.28 | 448–2000 |
| 12.50mm | 350–1877 | 0.06–0.35 | 0.18–4.19 | 448–2000 |
| 25.00mm | 688–3378 | 0.13–0.62 | 0.34–7.54 | 448–2000 |

Table 3.5: Porous medium with porous plate, Adimensional numbers, Vintimille

**Hydrodynamic coefficients**

The results of experimental versus numerical tests are presented for the three same amplitudes A=[6.25mm, 12.50mm, 20.00mm] in figures 3.32 to 3.37.

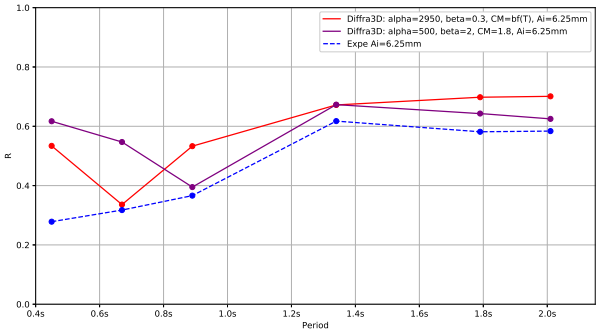


Figure 3.32: Reflection curve, Ai=6.25mm

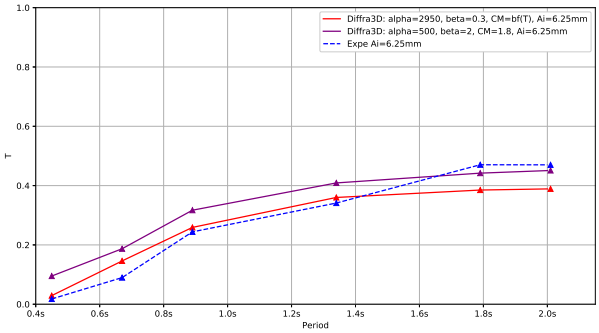


Figure 3.33: Transmission curve, Ai=6.25mm

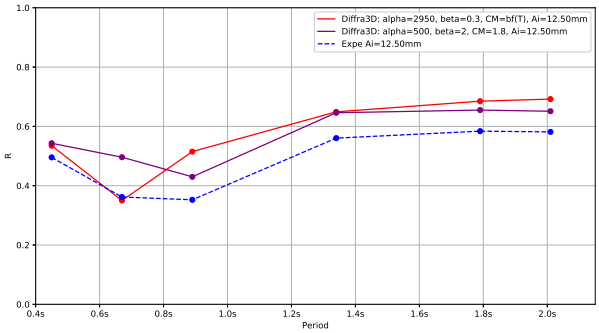


Figure 3.34: Reflection curve, Ai=12.5mm

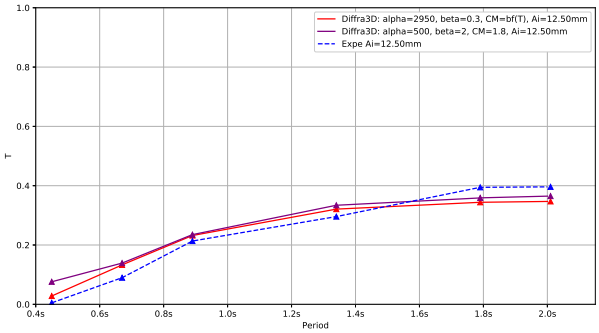


Figure 3.35: Transmission curve, Ai=12.5mm

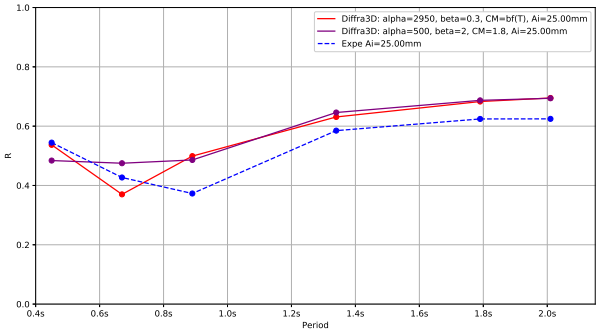


Figure 3.36: Reflection curve, Ai=25.0mm

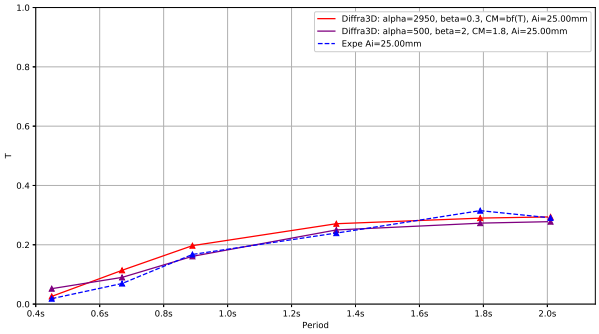


Figure 3.37: Transmission curve, Ai=25.0mm

With a porous plate, the reflection is almost constant for $T \geq 1.34s$. Around $R = 60\%$, it corresponds to the upper limit of the configuration without a plate. For the smallest periods, the reflection is nearly untouched. The transmission is kept lower than 40% for almost every amplitude and period. Finally, a porous medium with a porous plate gives the required performance. It has quite good damping properties for a large range of periods and does not transmit too much energy behind. This configuration was chosen for construction.

The two selections 1 and 2 of parameters give good transmission levels. The reflection is a little overestimated. For the smallest periods $T \leq 0.89s$, the two simulations are not accurate especially for $A_i = 6.25mm$.

## 3.5 Conclusion

The construction of a breakwater in the entry of the harbour of Vintimille was required to protect the boats moored all along the main dike. This breakwater was chosen as a vertical structure to take the least space

possible. A 70m-long mega-yacht is moored on the left side. On the right side, 30 to 45m-long yachts are also moored. The porous nature of the structure is adopted for environmental purposes. A porous plate at the back of the porous medium is placed to prevent too much transmission of the waves and to avoid a too high level of reflection. This solution is a compromise.

The numerical model *Diffra3D* reproduces well the hydrodynamic performance of the tested configurations for all the range of periods and amplitudes with the Selection 1 of the resistance parameters : $\alpha = 2950$, $\beta = 0.3$ and $C_M$ function of the period.

The parameters of Selection 2 ($\alpha = 500$, $\beta = 2$ and $C_M = 1.8$) give relatively good results too for the largest periods. As the inertia coefficient $C_M$ tends to a constant value when $T$ or $KC$ increases, it is often justifiable to fix constant the inertial parameter for real cases where $KC$ numbers are high. For example, if we look at the literature, the experimental parameters of Van Gent (1993) [59], $\gamma_p$ such as $S = (1 + \gamma_p \frac{1-n}{n})/n$ is often fixed to 0.34 in numerical tests. With our expression, the value of $C_M$ would be $\approx 1.8$.

However, *Diffra3D* is unable to perfectly fit the experimental data for the smallest periods with the parameters of Selection 2, $C_M$ as constant. The smallest periods are of laminar and inertial nature.

# 4 THIRD CAMPAIGN : ISTRES AND BANYULS-SUR-MER

The new project of Istres harbour (FRANCE, 13) and the renovation project of Banyuls-Sur-Mer harbour (FRANCE, 66) provided the occasion to implement innovative vertical breakwaters.

Experimental tests on a small-scale model have been undertaken in order to answer the following issues :

- To understand the hydrodynamic performance of a simple vertical rocks structure, in terms of reflection and transmission, with parameters like stone size.
- To evaluate global loads on the overall structures and local efforts on the metal framework or on the bored piles which keep the stones vertical.
- To validate the diffraction code *Diffra3D* with real case study data.

To solve these issues, three different size distributions $d_{n50}$ were tested.

In this chapter, first, the context of the projects are presented in order to identify and locate appropriate positions for the breakwaters, and to consider environmental and other specific issues that justify the use of these alternative and innovative technical solutions. Then, the experimental set-up for the small-scale model of a vertical rockfill breakwater is described. The experimental results are compared to the simulation results.

## 4.1 Context of projects

### 4.1.1 Istres' harbour

The extension project of *Heures Claires*' harbour in Istres is a part of a global plan to upgrade existing infrastructures in order to welcome new pleasure craft and harmonise maritime and urban areas.

The preliminary studies resulted in a few principles for the restructuring of the port's maritime infrastructures. The task that draws our attention is the wave-damping breakwater that will equip the first pontoon, which is shown in figure 4.1.

The breakwater is an innovative design, adopting the principle of a vertical rockfill breakwater. A sketch of this innovative breakwater is presented in the introduction (Fig. 3). The rocks that form the porous medium are enclosed by bored piles and dissipate the energy of short-period waves approaching from the south. It has a low 2.4m wide footprint under the 3m wide pontoon and hence, it does not encroach on the mooring surfaces. The vertical riprap structure is naturally integrated into the marine environment, promoting biodiversity.


Figure 4.1: 3D view of Istres harbour with the spot of the interested pontoon

The new breakwater is necessary to complete the protection provided by the main elongated dike and to get residual agitation at least equivalent to that currently met. At this location a classical breakwater was previously installed and boats were only moored behind it. The incident waves at Istres are coming from the east-southeast region and are listed in the table 4.1. Their characteristics are determined at the port's entrance.

| **Period of return** | **Sector East to Southeast** |
|---|---|
| 1 year | $H_s = 1.05m$, $T_p = 4.0s$, $N105$ |
| 5 years | $H_s = 1.20m$, $T_p = 4.3s$, $N105$ |
| 10 years | $H_s = 1.25m$, $T_p = 4.5s$, $N105$ |
| 20 years | $H_s = 1.35m$, $T_p = 4.9s$, $N105$ |
| 50 years | $H_s = 1.45m$, $T_p = 4.9s$, $N105$ |
| 100 years | $H_s = 1.50m$, $T_p = 5.0s$, $N110$ |

Table 4.1: Istres incident waves

### 4.1.2 Banyuls-Sur-Mer's harbour

The harbour of Banyuls-sur-Mer is open to the northwest, allowing part of the energy of the offshore swells to enter. The security of the water body is currently not assured throughout the western part of the port. Boats usually moored in this area are moved ashore or to other ports in winter. The *Georges Petit* wharf and all the pontoons are in poor condition and need to be renovated or replaced.

The municipality of Banyuls-sur-Mer commissioned **HydroGC SAS** as a Research Department to conduct hydrodynamic studies. A numerical study is conducted to evaluate the impact of new configurations in relation to the current one. The main objective, together with the refurbishment of the pontoons, is to secure the port and to extend the calm area of the harbour.

There are many solutions suited to the coastal infrastructure at Banyuls. Here are the principal ones in terms of hydrodynamics protection, which correspond to our interest :

- The extension of the current main dike with at the end the creation of a circular vertical riprap structure

($\varnothing = 20m$) that remains 5m away from the protected sea grasses and makes the harbour entrance calmer, see figure 1. The circular breakwater has a solid wall in its center facing the biggest swells coming from the east to prevent any transmission backwards.

- The extension of the 20m counter-jetty by the addition of a prefabricated caisson, with a damping chamber at the front and spaced gabions at the back, see figure 2.
- The installation of two damping caissons inside the port, with a similar design as the new counter-jetty. These are located to avoid encroaching on the protected sea grass in green in figure 4.2.

These three kinds of breakwaters include porous media and/or damping chambers in order to attenuate the incident waves but also for environmental purposes in the case of the spaced gabions placed at the back of the three caissons.

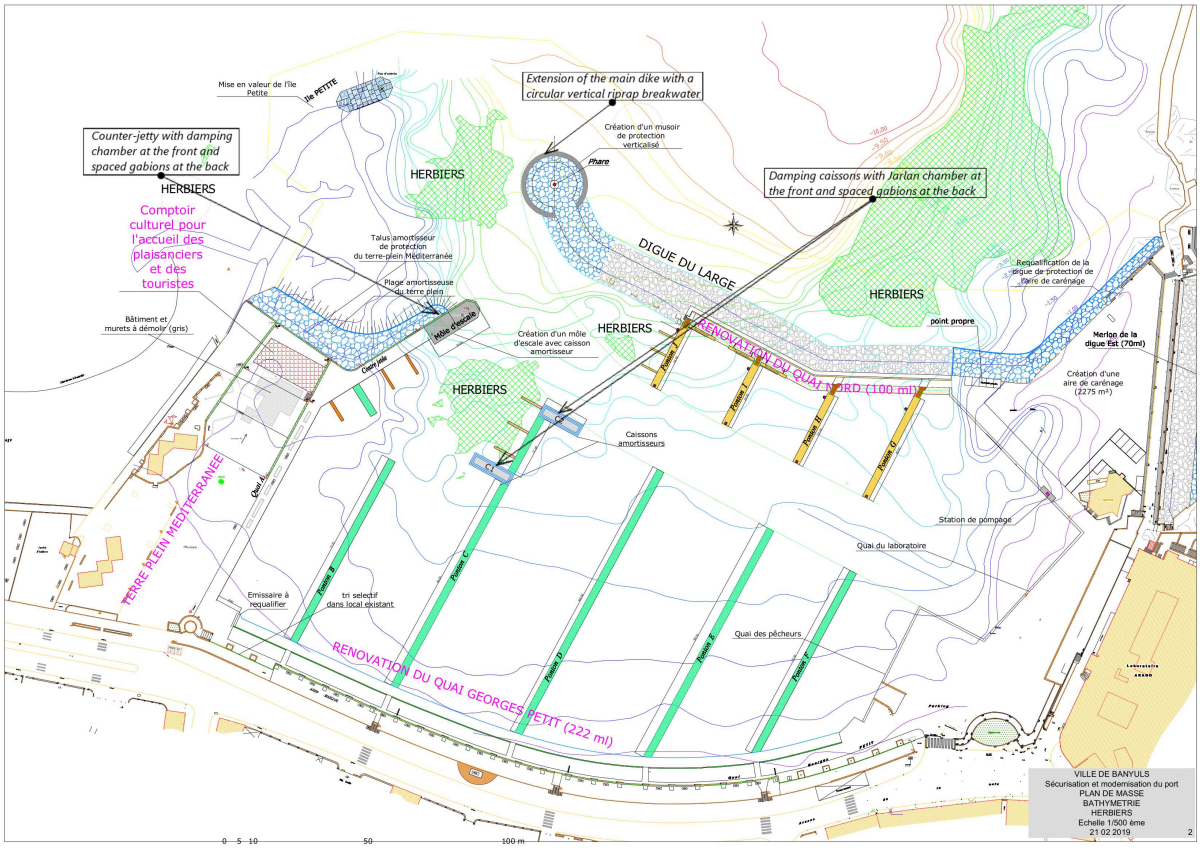


Figure 4.2: Ground plane of Banyuls-sur-Mer harbour

The incident waves at Banyuls are coming from the east region. Their characteristics, used for design, are defined close to the port's entry. They are reported in table 4.2.

| **Period of return** | **Sector East** |
|---|---|
| 1 year | $H_s = 3.1m,\ T_p = 9.4s,\ N71$ |
| 5 years | $H_s = 4.4m,\ T_p = 11.0s,\ N71$ |
| 10 years | $H_s = 5.0m,\ T_p = 12.0s,\ N73$ |
| 50 years | $H_s = 7.4m,\ T_p = 12.8s,\ N79$ |
| 100 years | $H_s = 7.9m,\ T_p = 13.8s,\ N79$ |

Table 4.2: Banyuls incident waves

## 4.2 Similarity and scale factors

Because of the small amplitudes of incident waves in Istres' project, a adapted scale is required. The 2.4m wide porous structure enables us to chose a 1/10 scale that leads to a model width of 24cm (see figure 4.5) and a water depth of 20cm.

The same scale-model is used to model the cross-section of the 20m large circular head breakwater of Banyuls-sur-Mer's. A 20m diameter corresponds to 15m width in 2D equivalent. A new scale of 1/31 is adopted. The scale-model of the porous medium is doubled to 48cm, which corresponds at real scale to approximately 15m in width. The water depth at the real scale becomes 6.2m. This is the water depth in front of the structure in Banyuls-sur-Mer. This second configuration enables us to compare the impact of widening a vertical breakwater.

## 4.3 Experimental set-up

### 4.3.1 Wave tank

The wave tank of the *Ecole Centrale de Marseille* was used for 6 weeks between the end of September to the end of November 2017. The wave tank is 17m long. It is equipped at one end with a flat wavemaker and at the other end with a porous damping structure (Fig. 4.3).

The water depth is set to $h = 20cm$. At this water level, the characteristics of the wavemaker does not enable the generation of the design waves. To fix this problem, a flat PVC floor of 22cm in height and with an initial slope of about 7% over $3m$ (Fig. 4.4) was installed bringing the water depth at the wavemaker to $42cm$.

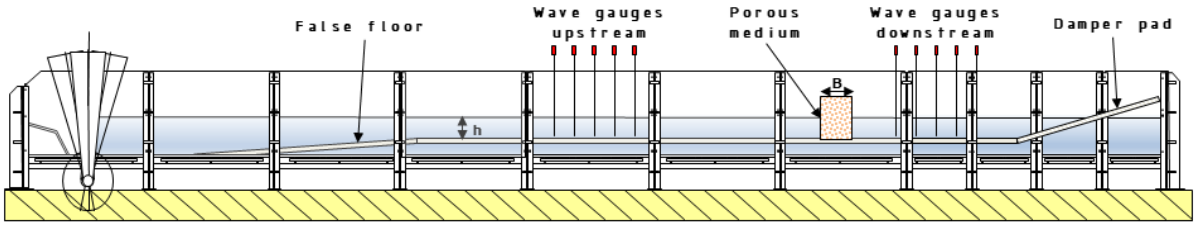


Figure 4.3: Schematic cross-section of the wave tank with scale model, Istres & Banyuls

Figure 4.4: False floor and breakwater model, Istres & Banyuls

### 4.3.2 The experimental model

The model is a cage with a steel structure to contain the blocks. Two plexiglass plates delimit the side edges and a plywood board constitutes the bottom (see figures 4.5 and 4.6).

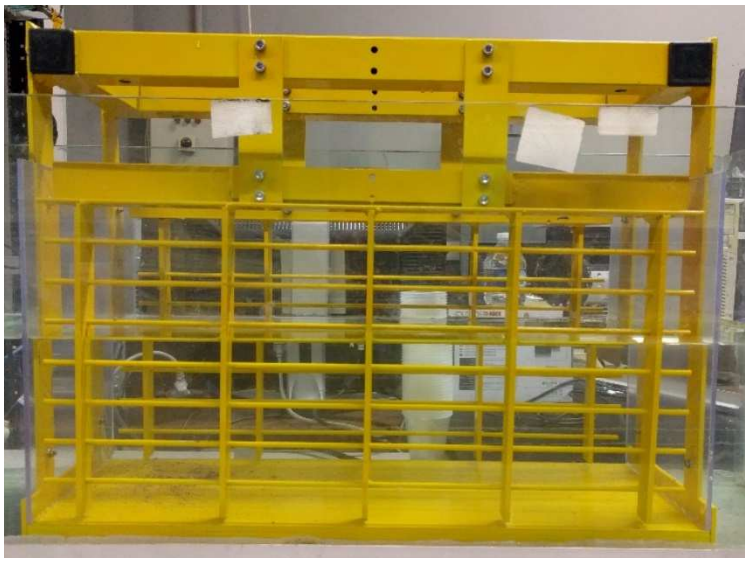

Figure 4.5: Experimental model, Istres & Banyuls

Figure 4.6: Oblique and top view of the cage, B=24cm, Istres & Banyuls

#### Rock description

The stones selected for the test campaign are limestone rock with a mean density of a typical sample measuring $\rho = 2620 kg.m^{-3}$. Three typical grain sizes were selected to explore the influence of rock size and porosity rate on the hydrodynamic performance of the structure (Fig. 4.7). The spread of the porosity rates is in the end $41.5\% \leq n \leq 46.1\%$. The stones are of course irregular. They were weighed one by one before each series of tests in order to determine the particle size curve corresponding to the sample in place as well as to determine the porosity. The porosity is also determined by measuring a water volume displacement. For this purpose, the dry stones are introduced in a small tank, and the variation in water level is measured. Particle size curves are reported in Appendix A. The sample of blocks, which had the smallest stones (G1), was then extended with smaller blocks to form a new distribution (G4). However, the stones in the new distribution, G4, were not laid one-by-one in the 48cm wide scale-model and so the porosity level obtained is not lower than for the original particle sizes, but quite the opposite.

Figure 4.7: From left to right : Size distribution 1, 2 and 3, Istres & Banyuls

The table below summarises the characteristics of the different size distribution used in this campaign. The porosity could not be kept constant by modifying $d_{n50}$.

| **Granulo metry** | $M_{10}$ | $M_{50}$ | $M_{85}$ | $d_{n50}$ | $n_{RRd}$[1] | **Porosity** |
|---|---|---|---|---|---|---|
| G1 | 170g | 233g | 282g | 4.5cm | 17.2 | 41.5% |
| G2 | 527g | 617g | 716g | 6.2cm | 28.4 | 43.6% |
| G3 | 1204g | 1861g | 2647g | 8.9cm | 11.0 | 44.8% |
| G4 | 114g | 182g | 258g | 4.1cm | 10.6 | 46.1% |

Table 4.3: Size distributions, Istres & Banyuls

### 4.3.3 Summary of the test parameters

Here is a summary of the different test parameters :

- The test scale is 1/10 for Istres and 1/31 for Banyuls.
- The water depth is h=20cm.
- The dimensions of the model are :
  - Height : 41cm
  - Width : 24cm (2.4m at scale 1/10). Then 48cm (≈15m at scale 1/31).
- Three different size distributions are tested :
  - Porosity 41.5% ≤ $n$ ≤ 44.8%
  - $4.5cm \leq d_{n50} \leq 8.9cm$
  - $11.0 \leq n_{RRd} \leq 28.4$ : narrow to very narrow size distribution
- The generated incident waves are :
  - H=[5mm, 12.5mm]
  - T=[0.63s 0.95s 1.26s 1.58s 1.90s 2.21s]

The table 4.4 gives the wave characteristics that are also reported in the diagram of Le Mehauté (1976). The performed waves are shown on figure 4.8. We notice that they are all part of Stokes 2nd order wave theory.

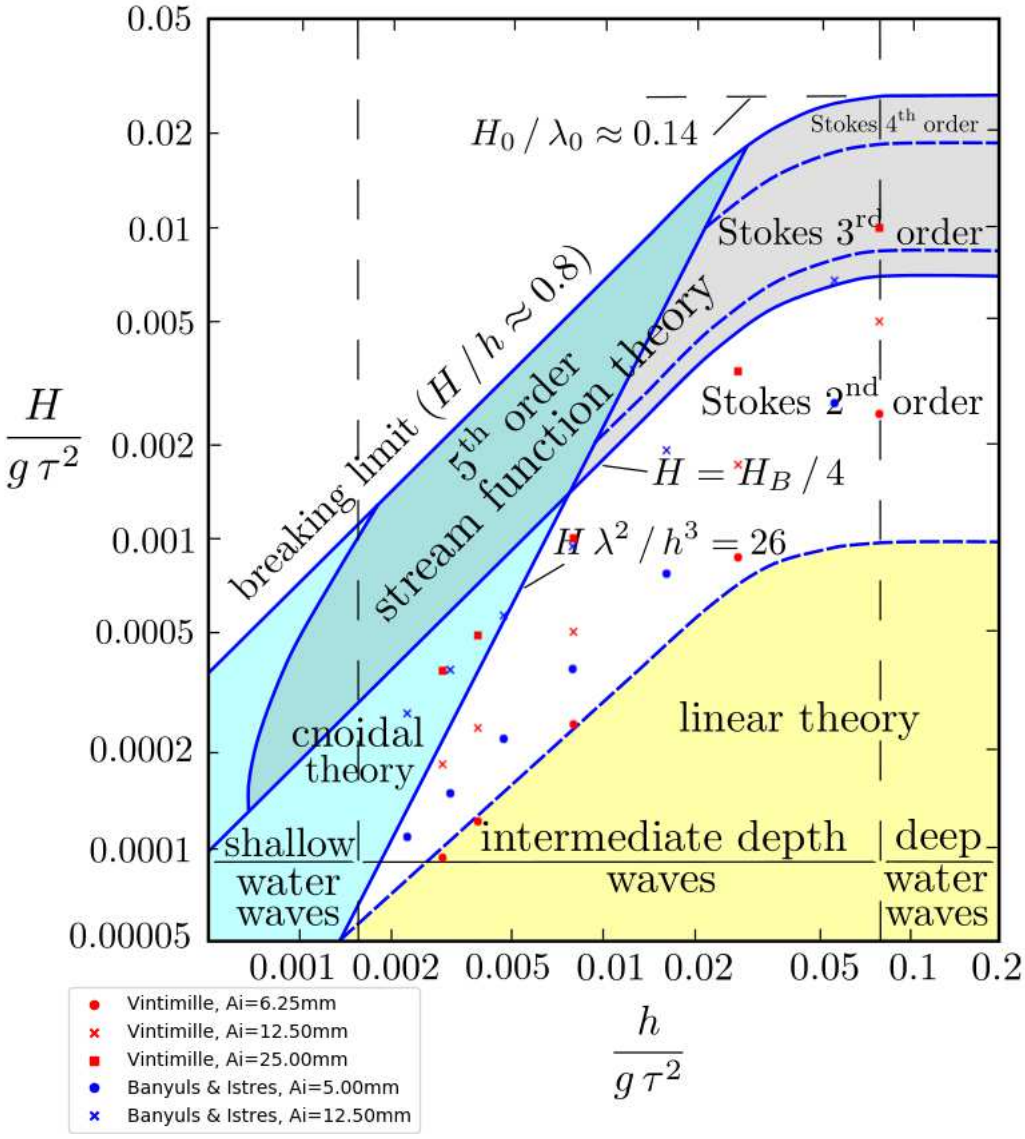


Figure 4.8: Applicability of wave theories, Le Mehauté (1976)

| | | **Wave period $T$** | | | | | |
|---|---|---|---|---|---|---|---|
| **Amplitude $A_i$** | **Variable** | **0.63s** | **0.95s** | **1.26s** | **1.58s** | **1.90s** | **2.21s** |
| 5.00mm | $H/(g\lambda^2)$ | 2.82e-3 | 7.95e-4 | 3.91e-4 | 2.32e-4 | 1.55e-4 | 1.12e-4 |
| | $U_r$ | 5.72e-3 | 2.03e-2 | 4.13e-3 | 6.94e-2 | 1.04e-1 | 1.43e-1 |
| 12.50mm | $H/(g\lambda^2)$ | 7.05e-3 | 1.99e-3 | 9.77e-4 | 5.81e-4 | 3.88e-4 | 2.81e-4 |
| | $U_r$ | 1.43e-2 | 5.08e-2 | 1.03e-1 | 1.73e-1 | 2.60e-1 | 3.59e-1 |
| - | $h/(g\lambda^2)$ | 5.64e-2 | 1.59e-2 | 7.80e-3 | 4.70e-3 | 3.10e-3 | 2.30e-3 |

Table 4.4: Wave characteristics of experimental tests, Banyuls & Istres

## 4.4 Comparisons between numerical and experimental results

This section compares the results between the numerical simulations and the physical experiments. The parameters used for the numerical simulations are the same as those used during the Vintimille experimental campaign, and are summarised here:

1. Selection 1

   The resistance coefficients of the porous medium from the sloshing tests, namely $a = 2950$ and $b = 0.3$. The Inertia coefficient $C_M$ is found by analysing a large range of values [0, 10] and minimising RMS error. This optimisation is performed in order to confirm the evolution of $C_M$ found in the tests for Vintimille (Sec. 3.3.3.4.1).

2. Selection 2

   The resistance parameters $\alpha = 500$, $\beta = 2$ and $C_M = 1.8$.

The figures in the following results section abide by the legend summarised here:

- Experimental data : blue
- *Diffra3D* + Selection 1 : red
- *Diffra3D* + Selection 2 : purple
- Analytical model : orange

### 4.4.1 A simple porous medium

The tested geometry is a vertical porous medium located in the wave tank (Fig. 4.9).

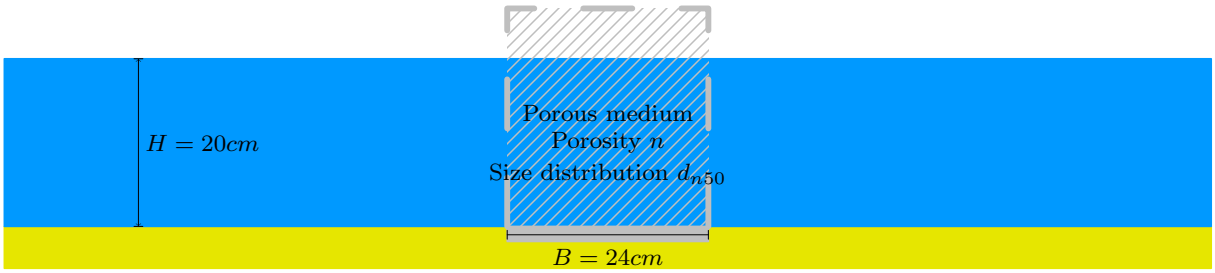


Figure 4.9: Geometry, Simple porous medium, Istres & Banyuls

**Discussion on $C_M$**

The figures 4.10 and 4.11 give the evolution of the optimised $C_M$ as a function of the period for the two amplitudes $A_i = 5.0mm$ and $A_i = 12.5mm$ for the three distribution of stones G1, G2 and G3. The values of $C_M$ obtained for the first configuration in the campaign of Vintimille (paragraph 3.3.3.4.1) are shown for the largest amplitude for comparison.

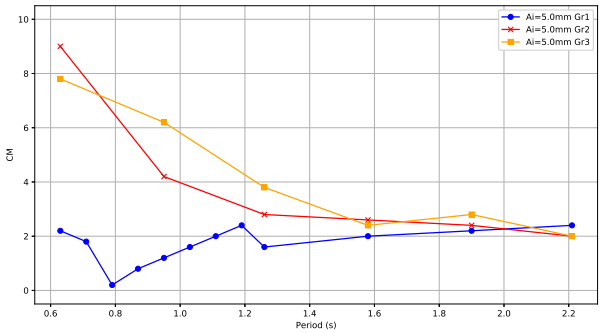


Figure 4.10: Inertia coefficient $C_M$, Ai=5.0mm, Istres & Banyuls

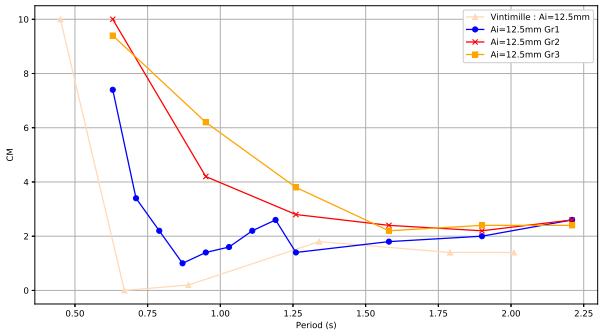


Figure 4.11: Inertia coefficient $C_M$, Ai=12.5mm, Vintimille, Istres & Banyuls

We notice that the evolution of $C_M$ for the distribution G1 follows a similar evolution as a function of the period than the values found in Vintimille tests. G1 decreases for the smallest periods to a lowest value before increasing to a constant value around 2 for $T \geq 1.1s$. However, the period where $C_M$ reaches its minimum is slightly shifted to higher periods.

The differences of configuration between tests G1 and Vintimille tests are reminded in the table below :

| - | **Banyuls & Istres (G1)** | **Vintimille** |
|---|---|---|
| **Water depth h** | 20cm | 38cm |
| **Width B** | 24cm | 15cm |
| **Porosity n** | 41.5% | 45% |
| $d_{n50}$ | 4.5cm | 3.0cm |
| $n_{RRd}$ | 17.2 | 13.2 |

Table 4.5: Differences of configuration between Banyuls & Istres (G1) and Vintimille

We compare in table 4.6 the adimensional numbers $R_e$ and $\beta_S$ of this set of tests with the Vintimille tests. The range of periods is $0.65s \leq T \leq 2.21s$.

| **Vintimille** | | | | |
|---|---|---|---|---|
| $A_i$ | $R_e$ | $F_o$ | $KC$ | $\beta_S$ |
| 12.5mm | 1421–2057 | 0.26–0.38 | 1.03–5.05 | 407–1385 |
| **Size distribution 1** | | | | |
| $A_i$ | $R_e$ | $F_o$ | $KC$ | $\beta_S$ |
| 5mm | 1055–2056 | 0.18–0.36 | 0.33–2.28 | 900–3157 |
| 12.5mm | 1459–4813 | 0.25–0.84 | 0.46–5.34 | 900–3157 |
| **Size distribution 2** | | | | |
| $A_i$ | $R_e$ | $F_o$ | $KC$ | $\beta_S$ |
| 5mm | 1023–3528 | 0.18–0.63 | 0.16–2.04 | 2010–6062 |
| 12.5mm | 2285–7805 | 0.41–1.41 | 0.38–4.51 | 2010–6062 |
| **Size distribution 3** | | | | |
| $A_i$ | $R_e$ | $F_o$ | $KC$ | $\beta_S$ |
| 5mm | 1843–5521 | 0.34–1.02 | 0.15–1.54 | 3576–12544 |
| 12.5mm | 4268–12180 | 0.79–2.24 | 0.34–3.41 | 3576–12544 |

Table 4.6: $B = 24cm$, Adimensional numbers, Istres & Banyuls

The Stokes parameters is $d^2_{n50\,BI}/d^2_{n50\,V} = 4.5cm^2/3.0cm^2 = 2.25$ times bigger for distribution G1 of Banyuls & Istres tests than for Vintimille tests. The Reynolds parameters is about the same at $T = 0.65s$. It rises then more

faster in Banyuls & Istres tests. We have to keep in minds that the two porous media have not the same porosity making the comparison not straightforward.

If we look again to figure 4.12 which shows the evolution of the inertia coefficient of a simple cylinder in oscillatory flow, we notice that the curve of $C_M$ as a function of $KC$ depends on $R_e$ and $\beta_S$. The increase of $R_e$ (dashed curves) tends to remove the inflexion point of the curves between $KC = 10$ and $KC = 20$. $C_M$ reaches its constant for higher $KC$. The increase of $\beta_S$ rises the inflexion point to higher $C_M$ at $KC$ constant. Figures 4.10 and 4.11 show similar results, by increasing $d_{n50}$ the inertia coefficient evolves as in figure 4.12 when the diameter of the cylinder increases.

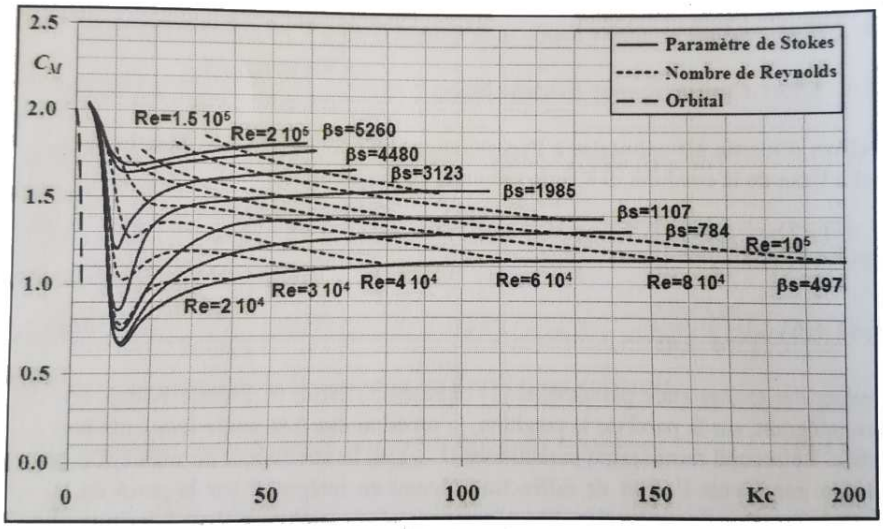


Figure 4.12: $C_M$ of a smooth cylinder function of $KC$ and $\beta_S$, Sarpkaya et Isaacson [3], Sloshing tests

The inertia coefficient $C_M$ of a porous medium may also depend on the nature of the flow, especially for small periods. For high periods, $C_M$ is around 2.0–2.4 instead of 1.4–1.8 In Vintimille tests. Further experimental tests may be conducted to confirm this relation.

As the porosity $n$ and the median nominal diameter $d_{n50}$ modify the adimensional numbers $R_e$, $KC$ and $\beta_S$, it may be possible to find a relation between $C_M$, $n$ and $d_{n50}$. For these reasons, we choose to use a different best fit (black curves in figures 4.13, 4.18 and 4.23) for $C_M$ for the three distributions of stones.

**Results for Size Distribution 1**

The figure 4.13 displays the best fit retained for the distribution G1.

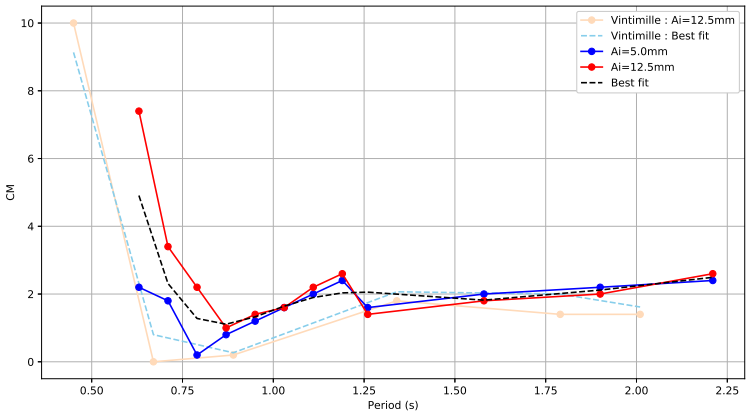


Figure 4.13: Inertia coefficient $C_M$, Simple porous medium, Size distribution 1

The figures 4.14 to 4.17 show the hydrodynamic performance for $R$ and $T$ with size distribution G1 (in blue) for $A_i = 5.0mm$ and $A_i = 12.5mm$. The results obtained with the different models are also displayed.

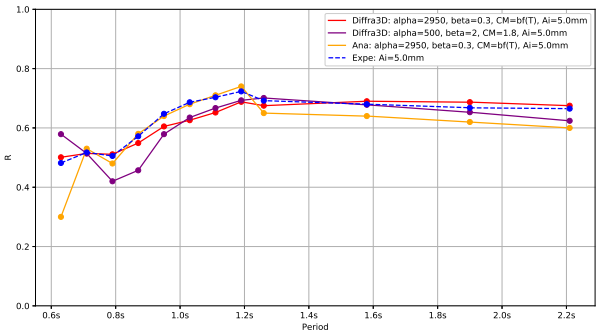


Figure 4.14: Reflection curve, Ai=5.0mm

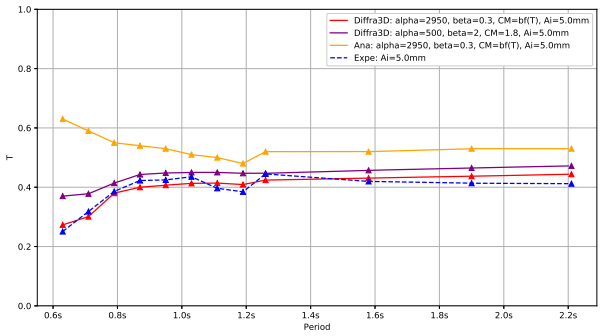


Figure 4.15: Transmission curve, Ai=5.0mm

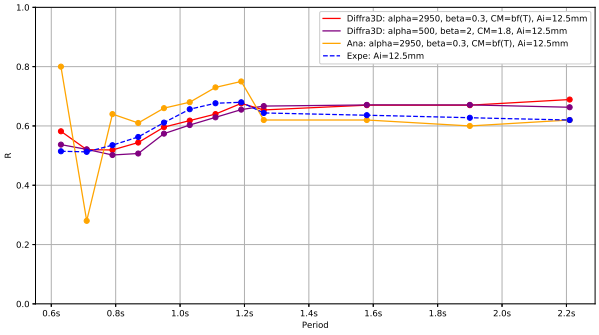


Figure 4.16: Reflection curve, Ai=12.5mm

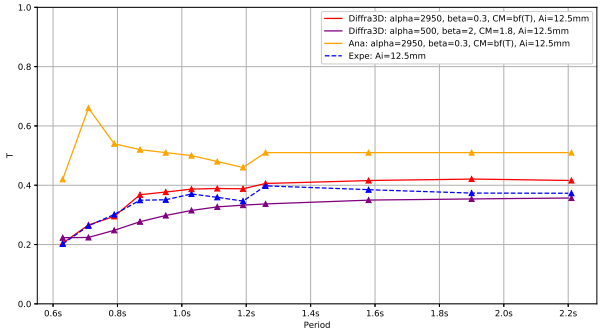


Figure 4.17: Transmission curve, Ai=12.5mm

The reflection and the transmission increase with the period until they reach a constant value between 60%–70% for the reflection and between 35%–45% for the transmission. The increase of the amplitude naturally brings a better dissipation. The reflection and the transmission are slightly lower for $A_i = 12.5mm$ than for $A_i = 5.0mm$.

The numerical model *Diffra3D* with parameter Selection 1 and Selection 2 is fairly faithful to the experimental data for large periods. For the smallest periods, $C_M$ needs to be adjusted to obtain the good behaviour. This is why the Selection 1 of parameters works better than Selection 2.

The analytical model gives results that fit reasonably the experimental data for large periods. It produces no correct results for the small periods, especially if we look at the transmission.

**Results for Size Distribution 2**

The figure 4.18 shows the best fit used for the distribution G2.

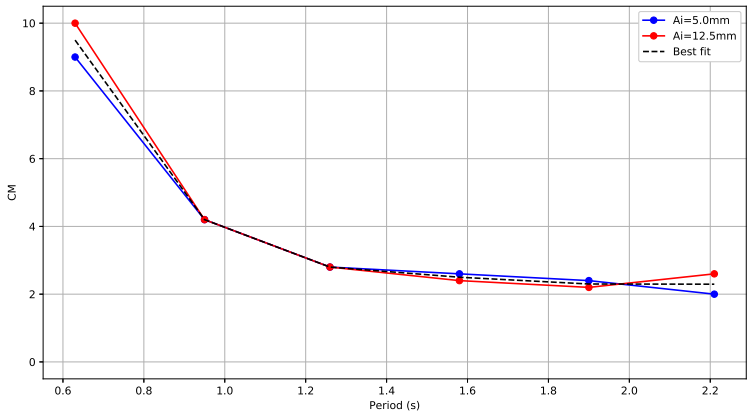


Figure 4.18: Inertia coefficient $C_M$, Simple porous medium, Size distribution 2

The results are displayed in figures 4.19 to 4.22 for the two same amplitudes.

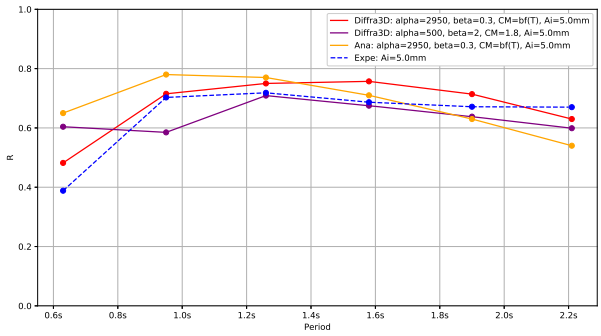


Figure 4.19: Reflection curve, Ai=5.0mm

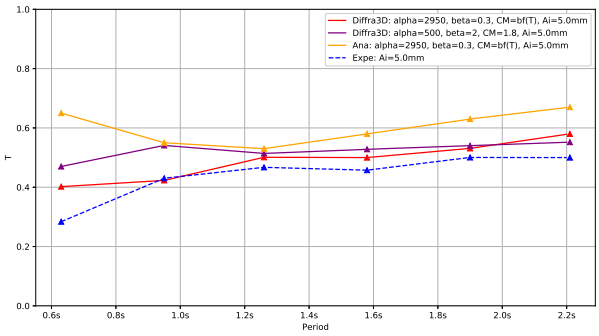


Figure 4.20: Transmission curve, Ai=5.0mm

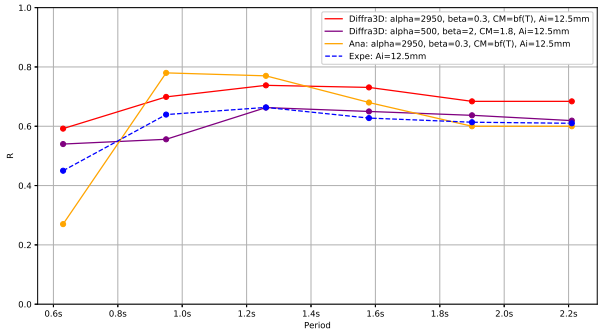


Figure 4.21: Reflection curve, Ai=12.5mm

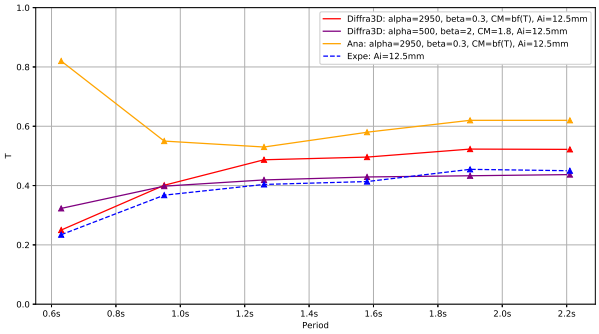


Figure 4.22: Transmission curve, Ai=12.5mm

For $A_i = 5.0mm$, Selection 1 and Selection 2 of parameters give good results for long periods. The results for the amplitude $A_i = 12.5mm$ are of more interest. The Selection 2 gives better results than the Selection 1 for the transmission and the reflection despite the optimisation of $C_M$. The Selection 1 overestimates the results. A possible explication is that the flow becomes more turbulent. The porosity and the nominal medium diameter are higher for the distribution G2 ($n = 43.6\%$ and $d_{n50} = 6.2cm$) than for the distribution G1 ($n = 45.5\%$ and $d_{n50} = 4.5cm$). It results in higher $R_e$ numbers, $KC$ numbers and $\beta_S$ number. The couple of resistance parameters $\alpha = 2950$ and $\beta = 0.3$ are maybe not well adapted for this case. The parameters $\alpha$ and $\beta$ may also depend on the nature on the flow. It may explain why every author in the literature has its own values. B. Jensen et al. (2014) [25] draw the same conclusion. $\alpha = 500$ and $\beta = 2$ are the best compromise of parameters which correspond to the different flow conditions they tested.

**Results for Size Distribution 3**

The figure 4.23 shows the best fit used for the distribution G3.

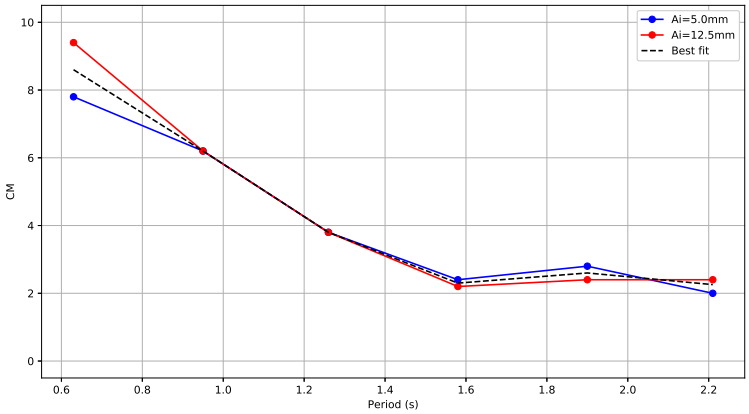


Figure 4.23: Inertia coefficient $C_M$, Simple porous medium, Size distribution 3

The reflection and the transmission are displayed in figures 4.24 to 4.27.

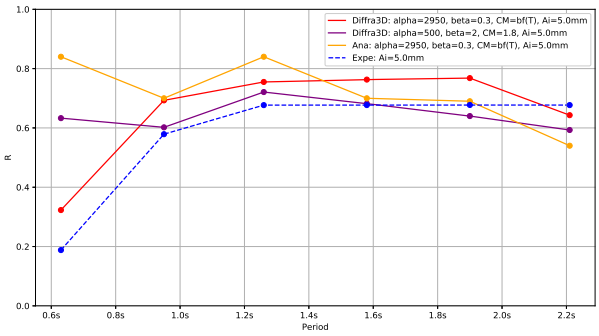


Figure 4.24: Reflection curve, Ai=5.0mm

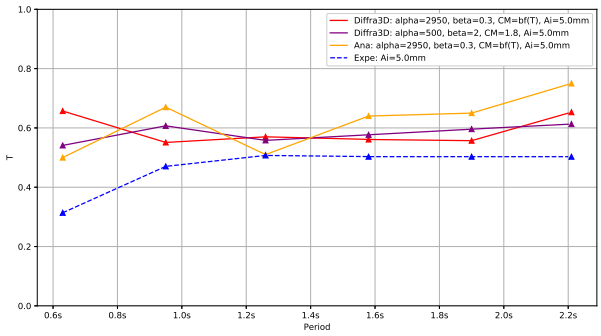


Figure 4.25: Transmission curve, Ai=5.0mm

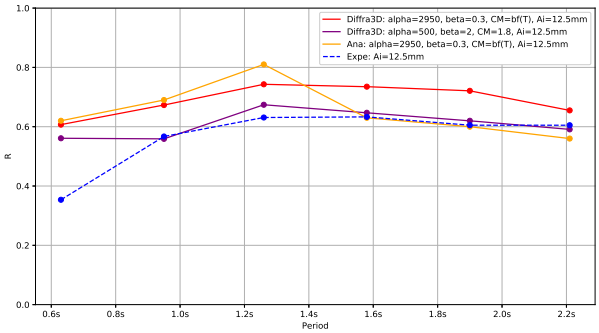


Figure 4.26: Reflection curve, Ai=12.5mm

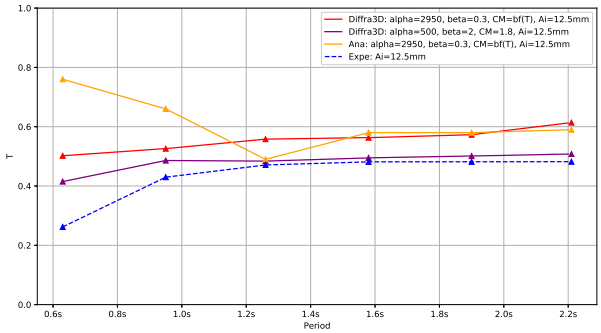


Figure 4.27: Transmission curve, Ai=12.5mm

The third distribution G3, the largest, gives slightly less reflection and then slightly more transmission, than with the distributions G1 and G2. The porosity and the nominal medium diameter of the distribution G3 are higher than the ones of G2 and G3.

This test confirms what we have observed with the distribution G2. The parameters of Selection 2 fit better than the parameters of Selection 1 for almost every period. The adimensional numbers $R_e$ and $\beta_S$ are higher.

The main objective of the vertical porous breakwater located under the first pontoon in Istres harbour is the dissipation of swell energy. The figures 4.28 and 4.29 display the dissipation rate for the three distributions of stones G1, G2 and G3 and for the two amplitudes $A_i = 5.0mm$ and $A_i = 12.5mm$. The dissipation rate is mostly better for the highest amplitude. The velocities are higher in the porous medium and therefore the dissipation is higher.

Drawing a conclusion on which distribution of stones gives the best dissipation rate is not straightforward. The $d_{n50}$ are different and the porosity rates of G1, G2 and G3 are close. However, we notice that the best effective distribution for large period (G1 in blue) is the worst distribution for very small periods. The size of the rocks does not play an critical role in the performance of porous breakwater for the range of amplitudes and periods tested. Any size of rocks can be used to fill the vertical porous breakwater installed under the first pontoon in Istres harbour.

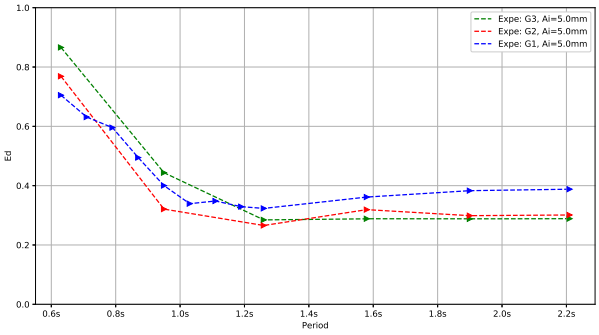


Figure 4.28: Dissipation rate, Ai=12.5mm

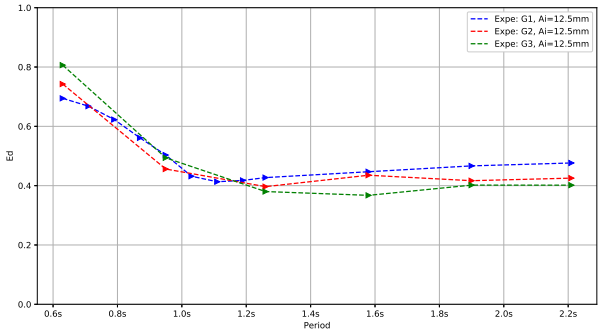


Figure 4.29: Dissipation rate, Ai=12.5mm

### 4.4.2 The porous medium's width is double

The porous medium's width is now doubled to 48cm in comparison to a width of 24cm previously (Fig. 4.30). Figure 4.31) shows the installation in the wave tank. The distribution of stones G4 is used.

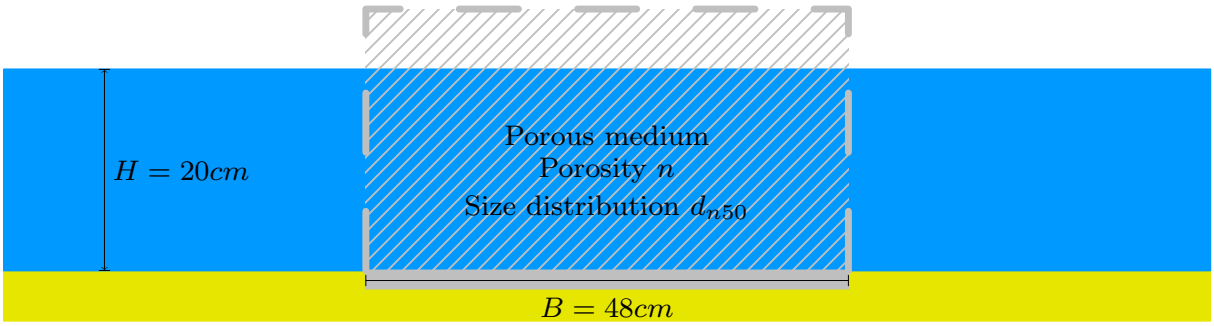


Figure 4.30: Geometry, Widened porous medium, Istres & Banyuls

Figure 4.31: Lateral view of the cage, B=48cm, Istres & Banyuls

The experimental and numerical results of the reflection and the transmission are displayed in figures 4.32 to 4.35. In this case, the values of $C_M$ for the parameters of Selection 1 are those used for the distribution G1 because the two distributions have close $d_{n50}$ ($d_{n50}$ = 4.1$cm$ for G4 and $d_{n50}$ = 4.5$cm$ for G1).

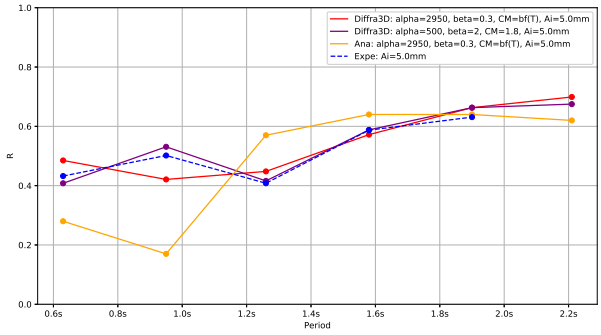


Figure 4.32: Reflection curve, Ai=5.0mm

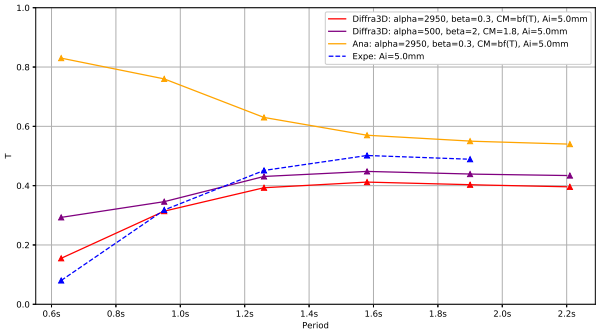


Figure 4.33: Transmission curve, Ai=5.0mm

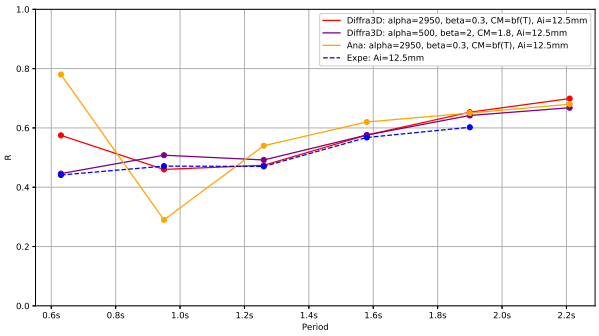


Figure 4.34: Reflection curve, Ai=12.5mm

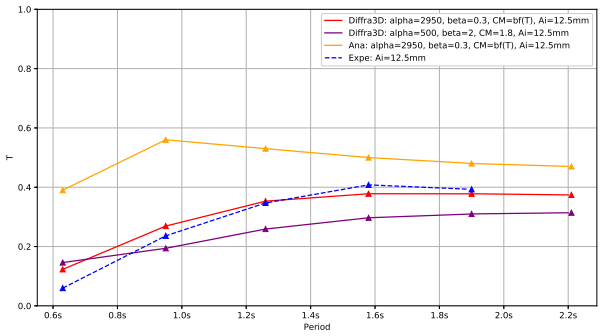


Figure 4.35: Transmission curve, Ai=12.5mm

Doubling the width does not decrease the transmission because the porosity of the stone distribution G4 is higher ($n = 46.1\%$) than for the porosity of G1 ($n = 41.5\%$). The reflection is also better. This shows experimentally that the porosity is the critical parameter to respect in order to achieve a targeted performance.

The two selections of parameters fit well the experimental data. The Selection 1 tends to underestimate the transmission for $A_i = 5.0mm$. The Selection 2 underestimates the transmission for $A_i = 12.5mm$.

The analytical model corresponds better with the reflection than the transmission for large periods. For small periods, the transmission is incorrect.

Preventing the waves that propagate from the east from entering the harbour of Banyuls is the main objective of the vertical circular breakwater that will be built at the end of the main dike. Experiments with a 48cm wide porous medium show that the transmission stays important ($> 40\%$) despite the width of the porous medium. For the port of Banyuls, it means that a simple porous medium, even a wide one, is not an adequate solution. To overcome this problem, it was decided to integrate a solid concrete wall at the center of the circular breakwater. The reflection is degraded but transmission is not possible..

## 4.5 Conclusion

Experiments for the harbour of Istres shows that the size of the stones is not a critical design parameter for a porous breakwater, contrary to porosity. However, the trend is that large stone size tend to give less reflection, and on the contrary, small sizes enable less transmission.

The tests for the port of Banyuls-sur-Mer show that a wide porous medium still allows high transmission. A simple circular porous breakwater is not enough in this case. A solid wall must be included inside the breakwater to prevent any transmission.

This set of tests highlights the fact that the inertia coefficient of a porous medium $C_M$ may depend on the nature of the crossing flow. The figure 4.36 displays the different measured values of $C_M$ for the experiments of Vintimille, Istres and Banyuls.

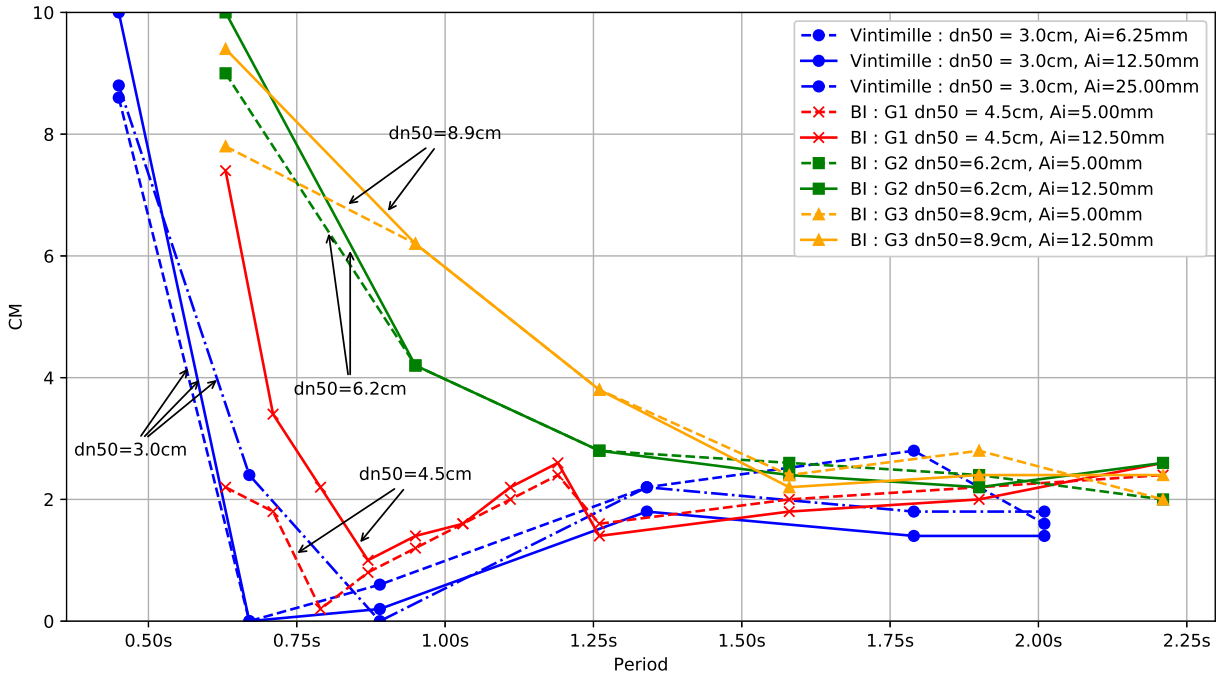


Figure 4.36: Overview of the different values of $C_M$

Increasing the amplitude tends to increase the inertia coefficient for the small periods. Increasing $d_{n50}$ also tends to increase $C_M$ for the small periods. For the range of periods, $T \in [0, 1.3]\,s$, we notice a significant evolution in the inertial coefficient, from 0 to 10. On the contrary, from a period around $T \geq 1.3s$, $C_M$ tends to get close to values between 1.6 to 2.4. We have to keep in mind that these observations are drawn with the parameters $\alpha$ and $\beta$ kept constant. Further studies can fix $C_M$ and vary $\alpha$ and $\beta$.

We need systematic and methodical testing to confirm these observations and to find a quantitative law for the evolution of $C_M$ for small periods. This could be an opportunity for a future study.

# 5 FOURTH CAMPAIGN : SPACED GABIONS

As noticed in chapter 3.4, the project of Banyuls-sur-Mer's harbour was the occasion to imagine two kinds of innovative vertical structures integrating porous media ; the big circular vertical riprap structure and the three damping caissons with a porous wall in the front and spaced gabions at the back (see figure 2).

The conception of a *Jarlan* chamber through optimisations with numerical methods is not new since equation (1.17) was developed by Lajoie & Bougis (2008). What's is innovative is the idea to create a kind of a porous plate with several spaced gabions in order to end up with the damping characteristics of the *Jarlan* chamber. Additionally, the porous media are favourable to young fishes and bring weight for stability in the case of weight-structures. This fourth campaign explores the hydrodynamic characteristics of such breakwaters. The experimental data are then compared to the results from *Diffra3D*. Some other practical applications are presented, for example how a damping chamber works without a floor or how a porous medium inside a *Jarlan* chamber modifies its reflection curve.

In Appendix B, sensitivity tests to design parameters of a classic *Jarlan* caisson such as porosity of the porous plate, hole's type, water depth and chamber's size are presented to regard how such breakwaters work. Commonly, reflection and transmission coefficients of damping caissons are the function of the non-dimensional value $B/\lambda$ with $B$ the width of the chamber and $\lambda$ the wavelength. The range of operation of a classical damping caisson takes place when $0.10 \leq B/\lambda \leq 0.15$. In this section, hydrodynamic coefficients are displayed as a function of the period because they are usually presented in this form to industry clients.

## 5.1 Experimental set-up

The scale model does not correspond to the structures of the project of Banyuls-sur-Mer's harbour. The geometry was especially chosen for our experimental tests to look into our problem. The tests take place once again in the tank at *Centrale Marseille*. The structure is located at approximately 11.4m from the wavemaker. A PVC wall cuts the tank and forms the opaque background of the breakwater. In front of the scale-model, the water depth is h=45.6cm.

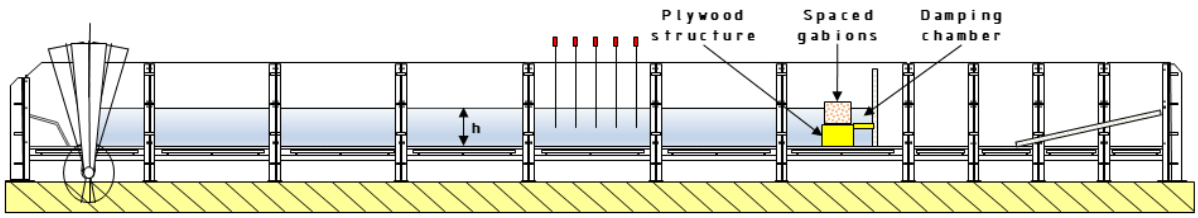


Figure 5.1: Schematic cross-section of the wave tank with the spaced gabions

### 5.1.1 The scale model

The stones which constitute the gabions (in yellow in figure 5.2) are held by a framework of stainless steel rods (see figure 5.3). The whole structure is raised by 30cm on a opaque plywood structure (in purple). Inside the structure, the water depth is equal to 15.6cm. The bottom of the damping chamber (in green) can be removed.

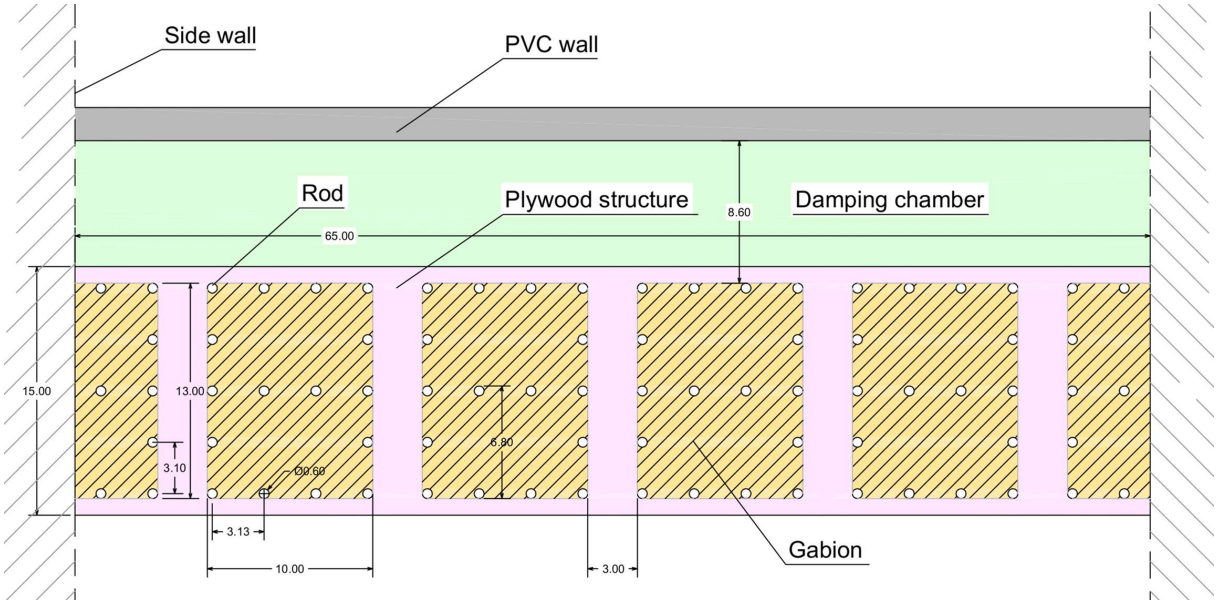


Figure 5.2: View from above - Sketch of spaced gabions

In the picture below (Fig. 5.3), the holes above plywood plate are to place the stones to form the gabions, one-by-one. There are in total five slots for five gabions. The global width of the slots corresponds to $\tau = 23\%$ of the breakwater' width.

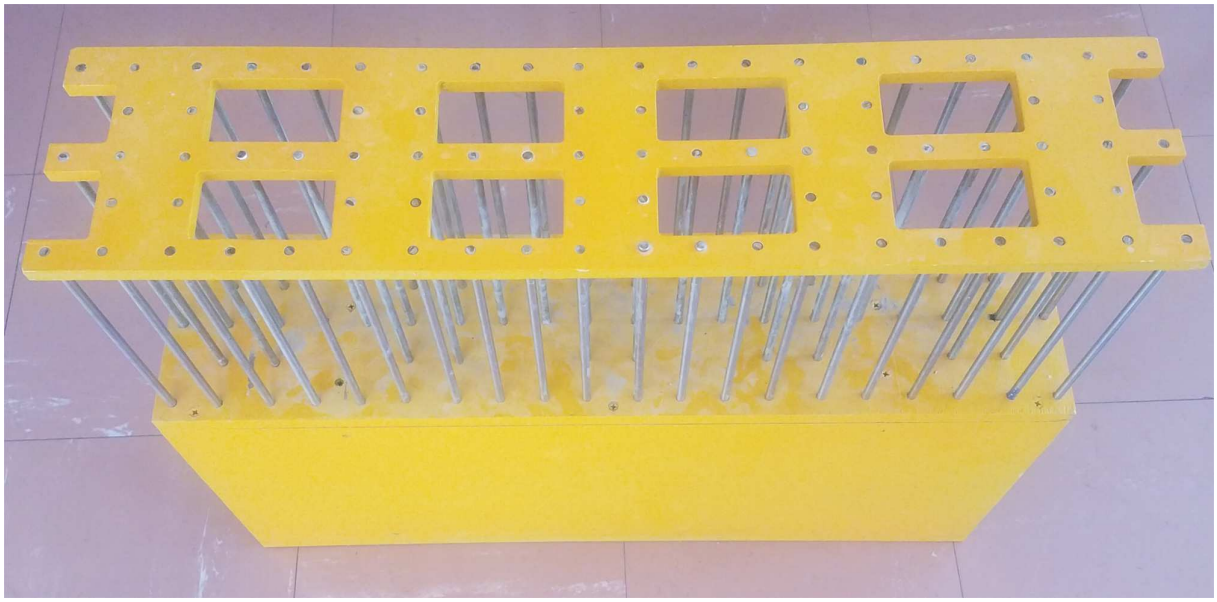

Figure 5.3: Oblique view of the scale-model, Spaced gabions

### 5.1.2 Rock description

The characteristics of the porous media forming the gabions are described in table 5.1. Please refer to Appendix B for the size distribution of the stones used in this experimental test. The relation $d_{n85}/d_{n15} = 1.16$ as $n_{RRd_{n50}} = 18.3$ correspond to a narrow size distribution parameter. The porosity $n = 41\%$ is a commonly found value.

| $M_{15}$ | $M_{50}$ | $M_{85}$ | $n_{RRM}$ | **Porosity** |
|---|---|---|---|---|
| 25g | 40g | 53g | 6.1 | 41% |
| $d_{n15}$ | $d_{n50}$ | $d_{n85}$ | $n_{RRd_{n50}}$ | |
| 2.5cm | 2.7cm | 2.9cm | 18.3 | |

Table 5.1: Size distribution, Spaced gabions

### 5.1.3 Performed experimental tests

Four configurations were investigated for a constant water depth $h = 45.6cm$ :

1. The gabions' size is $b = 13cm$. The chamber's size is $B = 8.6cm$. The water depth inside the chamber is $h_c = 15.6cm$. A sketch is designed in figure 5.12.
2. The bottom of the damping chamber is removed compared to the previous configuration, see figure 5.16. The other parameters stay the same.
3. There is no damping chamber. The other parameters stay the same, see figure 5.18.
4. We start again from the configuration 1. For this setup, the gabions' size is divided by 2, $b = 6.8cm$. The other parameters stay the same, see figure 5.21.

Only regular waves were generated. The range of periods is $0.6s \leq T \leq 2.0s$. and the wave heights are $A_i = 8mm$ and $A_i = 16mm$. The wave steepness is then in the range $0.4\% \leq H/\lambda \leq 2.8\%$ for $A_i = 8mm$ and $0.8\% \leq H/\lambda \leq 5.6\%$ for $A_i = 16mm$.

## 5.2 Theoretical model

Before our experimental results, some numerical investigations were conducted using two different approaches in order to model a porous plate : a 2D theoretical formulation of a porous plate and a 3D modelling. This justifies the use of our numerical model to describe spaced gabions in 3D.

### 5.2.1 Comparison of 2D theoretical formulation of a porous plate with a 3D modelling

The code *Diffra3D* makes it possible to simulate a porous plate through two methods :

- The 2D theoretical formulation of a porous plate described in section 2.1.1.2. For section and top view, refer to figures 5.4 and 5.6.
- A 3D modelling of a porous plate with modelled holes. Section and top views are presented in figures 5.5 and 5.7.

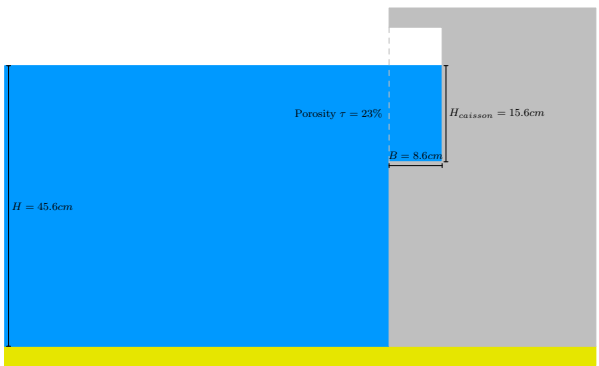


Figure 5.4: Section : 2D model

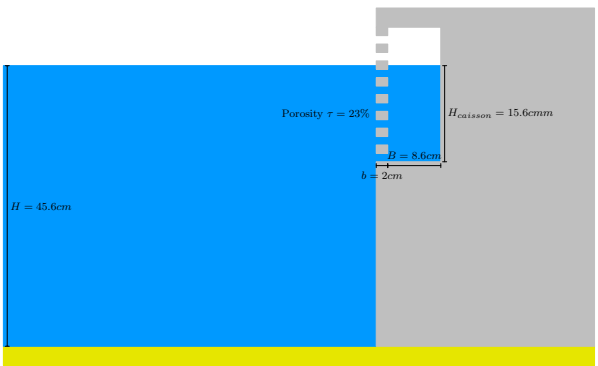


Figure 5.5: Section : 3D model

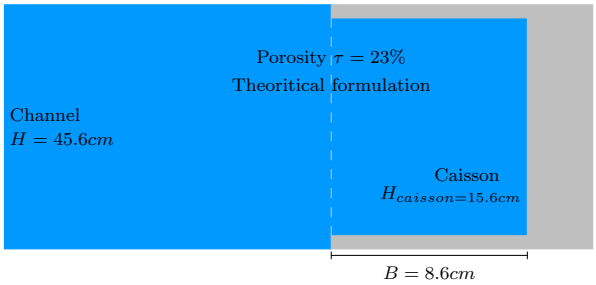


Figure 5.6: Top view : 2D model

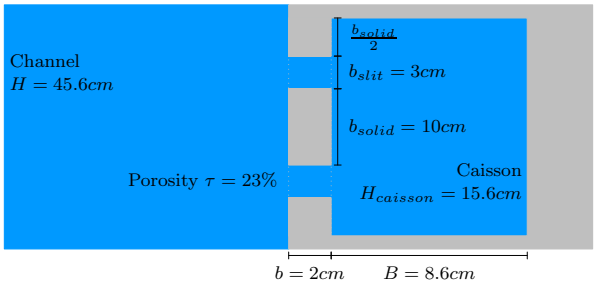


Figure 5.7: Top view : 3D model

We are looking for comparable results with the two models. Then we need to be sure to have similar theoretical backgrounds of how each computes the pressure loss in the two cases. The global pressure loss of the theoretical formulation is given in equation (1.17). Only the singular pressure loss is recalled here :

$$\Delta p = \frac{1}{2} K_p v_{dn}^2 \tag{5.1}$$

with $K_p = \frac{1-\tau}{k_c^2 \tau^2}$.

In the 3D modelling of a porous plate, the inertial term of the pressure loss is directly computed by the model. The singular loss of pressure is added to every hole to match the singular pressure loss of the 2D modelling. This pressure loss can be for this case written by :

$$\Delta p' = \frac{1}{2} K'_p v_{dn}^2 \tag{5.2}$$

with $K'_p = \frac{1}{k_c^2}$.

As the singular loss of pressure takes place when water jets come out of the slots, we put half of this loss of pressure on either side of the slots. This corresponds to the filling and the emptying of the damping chamber. The results of the comparison are presented in figure 5.8 for two wave heights $A_i = 8mm$ and $A_i = 16mm$. They show similar reflection coefficients for both methods, validating the 3D modelling of a thin porous plate.

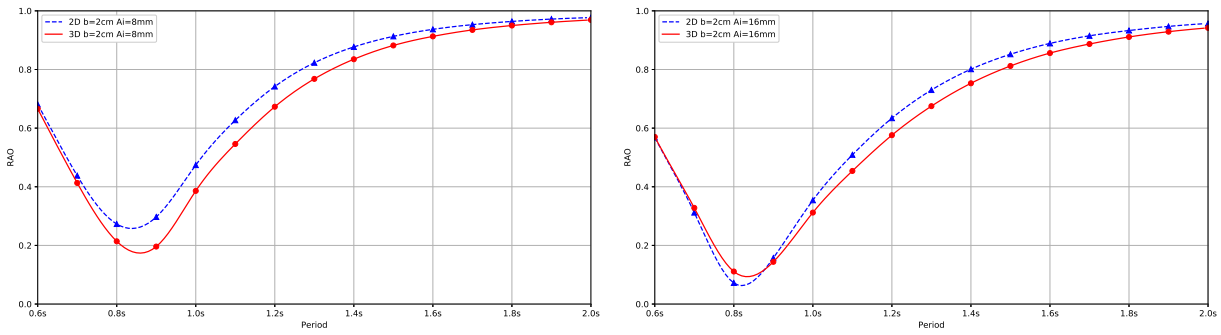


Figure 5.8: Reflection curves - Theoretical formulation (2D) of a porous plate (blue dashed) vs 3D model (red), $b = 2cm$, $A_i = 8mm$ and $A_i = 16mm$

### 5.2.2 The porous plate is widened

The porous plate is now widened to $b = 13cm$ to be equal to the gabions' size of the experimental tests, see figure 5.10. We want to know if the 2D theoretical formulation remains valid for a large porous plate.

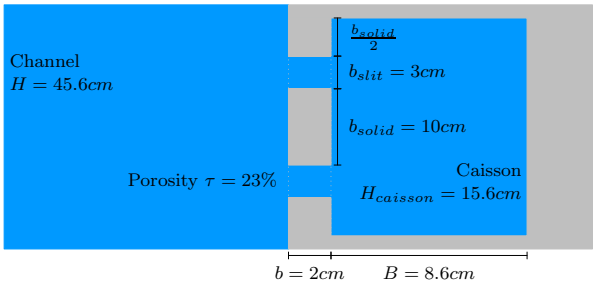


Figure 5.9: Top view : 3D model, $b = 2cm$

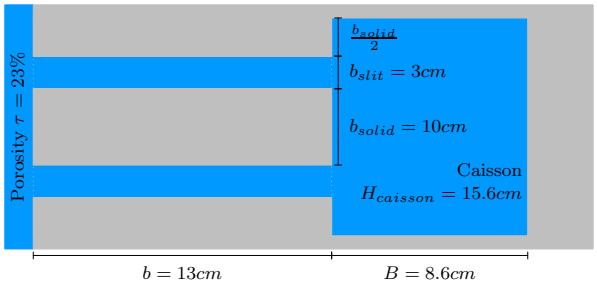


Figure 5.10: Top view : 3D model, $b = 13cm$

The results of the reflection coefficients are presented in figure 5.11 for the two wave heights $A_i = 8mm$ and $A_i = 16mm$. The results of the previous test with a thin porous plate are also displayed for comparison (in transparency). Widening the wall naturally shifts the damping peak to higher periods because it raises the inertial term of the loss of pressure.

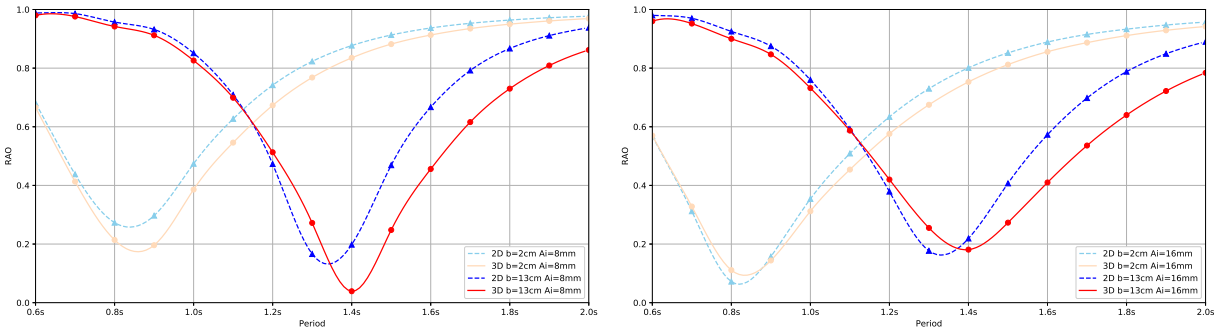


Figure 5.11: Reflection curves - Thicker porous plate, $A_i = 8mm$ and $A_i = 16mm$ - $b = 2cm$ (blue dashed) vs $b = 13$ (red)

We observe that the similarity between the 2D theoretical expression and the 3D modelling is degraded for periods $T > 1.4s$ in comparison to the case with a thin porous plate. A possible explanation comes from the transition between the incoming and the reverse flow. There is a duration while the flow is not homogeneous in the slots. The theoretical 2D formulation can not model this phenomenon.

## 5.3 Comparisons between numerical and experimental results

### 5.3.1 Set-up 1 : Classical *Jarlan* chamber with spaced gabions as thick porous plate

The basic experimental configuration is a damping chamber with a porous plate using spaced gabions. The parameters for the experimental set-up 1 are listed below and visually shown in figures 5.12 and 5.13 :

- Gabions' size : $b = 10cm$
- Chamber's size : $B = 8.6cm$
- Water depth inside the chamber : $h_c = 15.6cm$
- Porosity of the gabions : $n = 41\%$
- Global slots' width compared to breakwater' width : $\tau = 23\%$

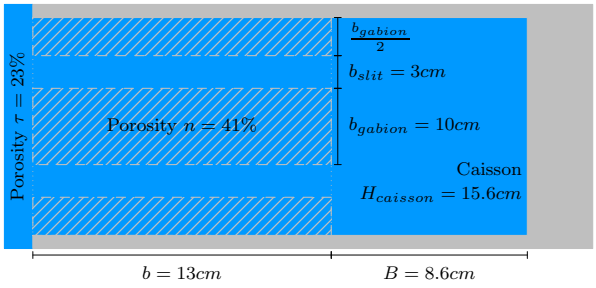


Figure 5.12: Top view : Spaced gabions, $b = 13cm$

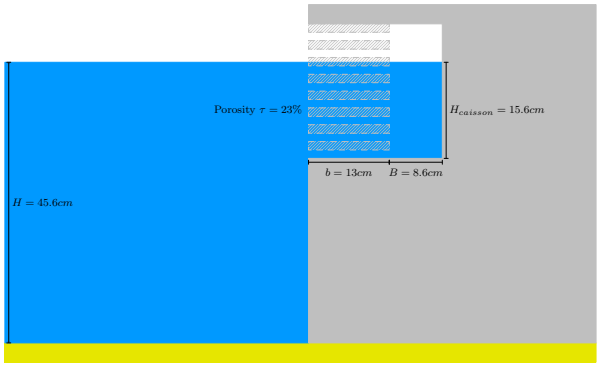


Figure 5.13: Section : Spaced gabions, $b = 13cm$

The experimental coefficients of reflection (in blue) are compared in figure 5.14 with the results from simulations (in red). For comparison, the results from the previous porous plate computations are displayed in translucent color.

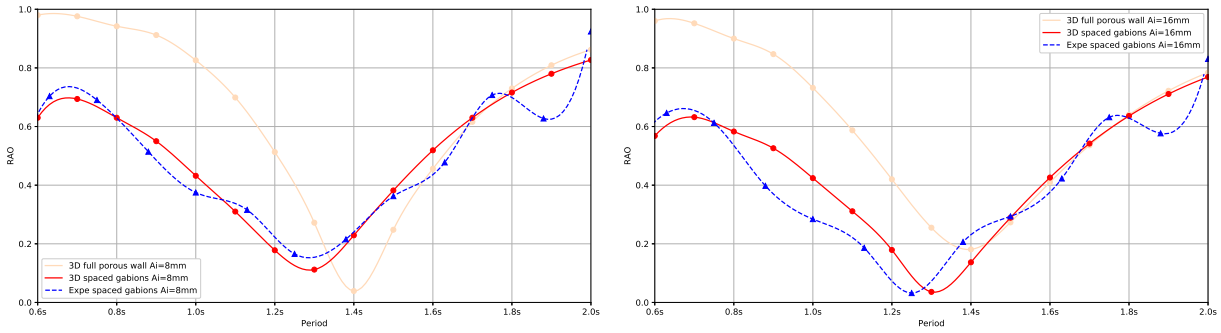


Figure 5.14: Reflections curves - $A_i = 8mm$ and $A_i = 16mm$ - Set-up 1

There is a good fit between the numerical data and experimental results. The model *Diffra3D* reproduces well enough the main hydrodynamic phenomena in this case, even if the minimum for the numerical reflection is lightly shifted for $A_i = 16mm$. We see that incorporating porous media to form the porous plate increases the performance of the damping structure by flattening the curve of reflection. It also shifts the peak towards smaller periods. The inertial term of pressure loss may be less important.

### 5.3.2 Set-up 2 : The bottom of the damping chamber is removed

The experimental set-up 2 checks a result found from simulations. The floor of a damping caisson does not play a major role. The wavelength in the damping chamber is defined by the water depth at the porous plate.

The only modification with previous configuration is that the water depth inside the chamber is now greater : $h_c = 45.6cm$ instead of $h_c = 15.6cm$. We removed the floor of the damping chamber as shown in figure 5.16.

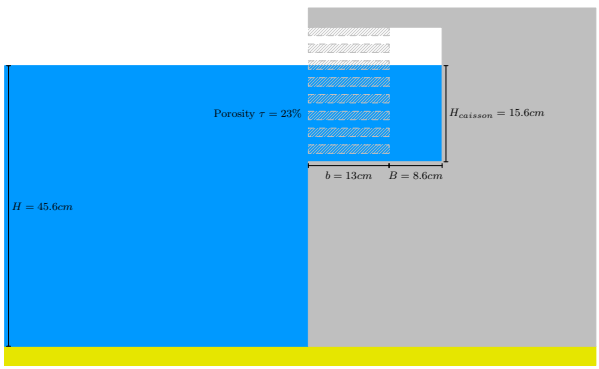


Figure 5.15: Spaced gabions

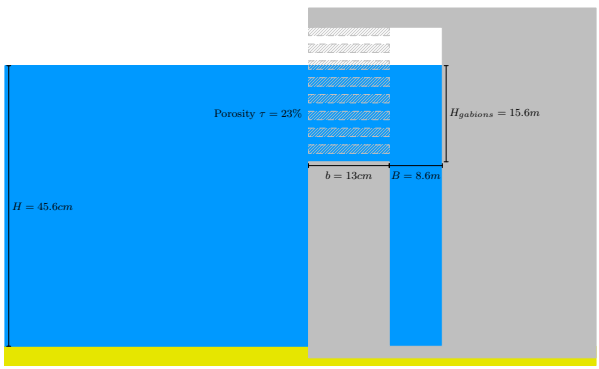


Figure 5.16: Spaced gabions, no floor

The experimental results of the reflection coefficients (in blue) and the computed ones (in red) are presented in figure 5.17. They are compared with the results from the previous configuration (in translucent color).

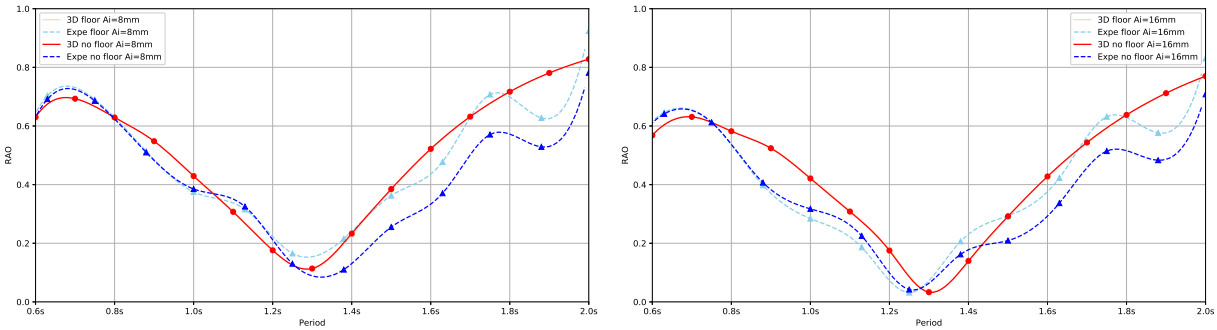


Figure 5.17: Reflections curves - $A_i = 8mm$ and $A_i = 16mm$ - Set-up 1 vs Set-up 2

The reflection coefficient of the damping caisson does not change a lot by removing the floor in the chamber. The reflection curve from the configuration without a floor is a little better for the highest periods (blue and light blue curves). This could be explained by the fact that some turbulences may appear at the new edge inside the chamber. The discrepancy between the experimental results and the numerical ones confirms this explanation. The numerical results are fully identical in the two cases, with and without a floor. A perfect fluid does not create any turbulence. The water particles held by the solid wall stay immobile. This problem could be solved by adding a theoretical pressure drop at the entrance of the lower part of the dissipation chamber.

This configuration opens an innovative and practical way of designing damping caissons with only sheet piles when the soil enables it.

### 5.3.3 Set-up 3 : Spaced gabions without damping chamber

Firstly, this configuration highlights the effectiveness of a damping chamber but also shows an interesting advantage of using spaced gabions instead of a simple porous plate. We tested the hydrodynamic performance of spaced gabions without any damping chamber behind (Fig. 5.18) and we compare the results with a simple gabion in front of a solid wall as described in figure 5.19.

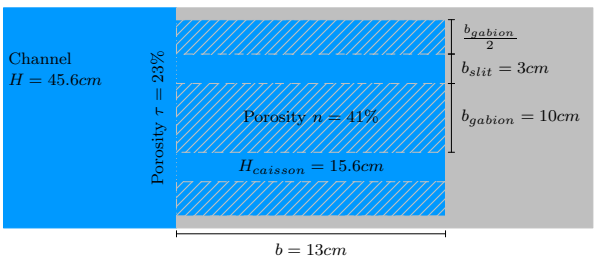


Figure 5.18: Spaced gabions with no chamber (red curve on figure 5.20)

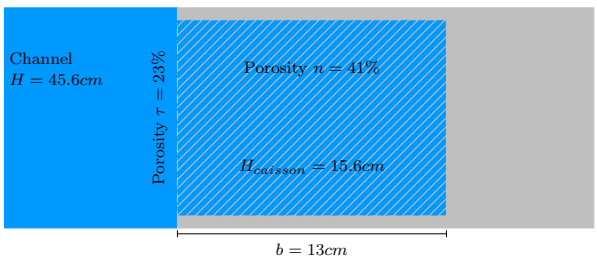


Figure 5.19: Simple gabion in front of a solid wall (green curve on figure 5.20)

Only the experimental coefficients of reflection (in blue) for $A_i = 16mm$ are available. We compare them with the computed results in figure 5.20.

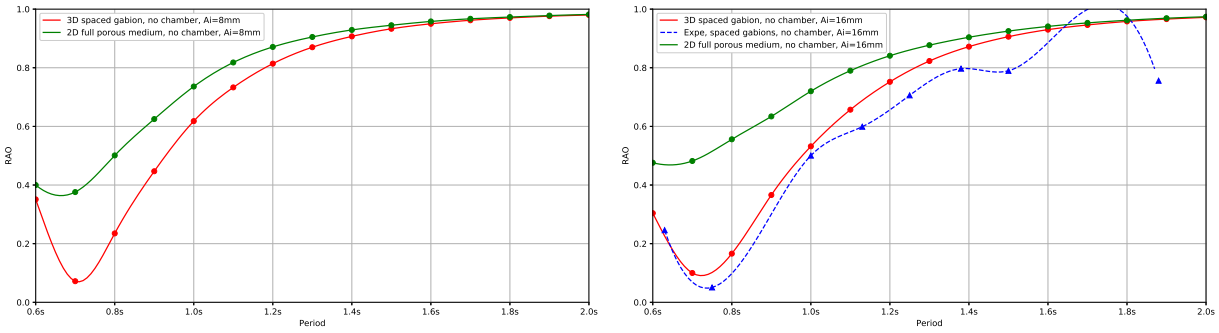


Figure 5.20: Reflections curves - $A_i = 8mm$ and $A_i = 16mm$ - Set3

The results show that spaced gabions in front of a solid wall is more advantageous than a simple porous medium because it brings a better damping for small periods. The waves can certainly expand in the slots and are subjected to the singular pressure loss on the way out.

### 5.3.4 Set-up 4 : The gabions' size is divided by 2

The fourth set-up is similar to set-up 1 but with the size of gabions divided by 2 (see in figure 5.21).

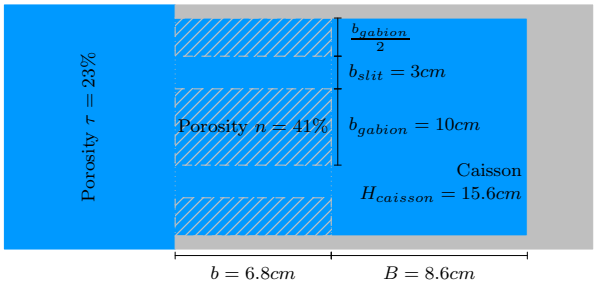


Figure 5.21: A thinner porous wall, $b = 6.8cm$

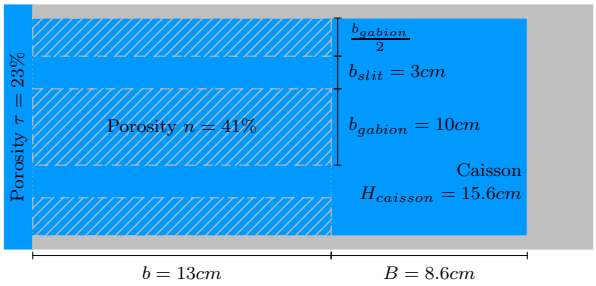


Figure 5.22: Large porous wall, $b = 13cm$

The experiment results of the reflection coefficients of the configuration $b = 6.8cm$ are shown in blue in figure 5.23 for $A_i = 16mm$. The computed results are in red in the same figure. For comparison, the results of the configuration $b = 13cm$ (set-up 1) are copied in translucent.

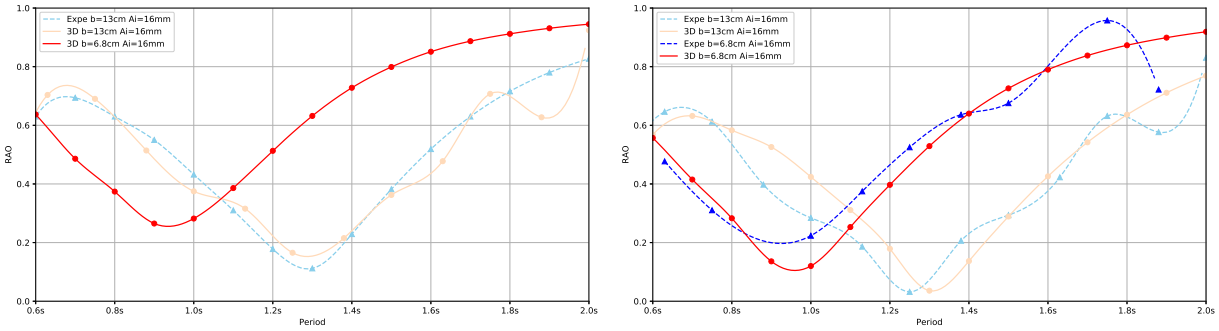


Figure 5.23: Reflections curves - $A_i = 8mm$ and $A_i = 16mm$ - Set-up 4 vs Set-up 1

The results of the numerical tests performed in introduction of this part are found again. The width of the porous plate affects the inertial term of the loss of pressure. The minimum reflection shifts toward lower periods with a smaller porous wall.

## 5.4 Practical applications

The experimental tests explored three innovations which could easily be built inside a harbour to bring down the agitation and for some of them improve the natural environment for young fishes. We proved that :

1. Spaced Gabions are more efficient for small periods compared to a simple porous medium in front of a solid wall.
2. Building a damping caisson with spaced gabions as a thick porous wall can provide a very good hydrodynamic performance. At peak efficiency the structure has a reflection rate of less than 20%.
3. Removing the floor of the damping chamber does not greatly change the hydrodynamic behaviour of a damping chamber but it may improve it.

A fourth direct application is to incorporate a porous medium inside the damping chamber. One advantage is to add weight to increase the stability of the device. Some numerical tendencies of this application are developed below.

### 5.4.1 Porous medium inside a damping chamber

We start with the *Jarlan* caisson configuration of Appendix B which has a large damping chamber $B = 7m$ (see figure 5.24). Two sets of configurations are tested :

1. The bottom of the damping chamber is raised using a porous medium (see figure 5.25).
2. The chamber's width is reduced through a porous medium at the background (see figure 5.29).

The porosity of the porous plate is set to $\tau = 40\%$. Slots are used as holes. The characteristics of the porous medium are $n = 40\%$ and $d_{n50} = 30cm$. In the case of the configuration 2, the porous plate is next to the porous medium. At this location, for the lower half of the porous plate, only half of the pressure drop created by the porous plate is implemented in order not to overestimate the global loss of pressure.

#### Porous medium at bottom

The figures 5.24, 5.25 and 5.26 present the geometrical characteristics of the first set of configurations 1, 2 and 3.

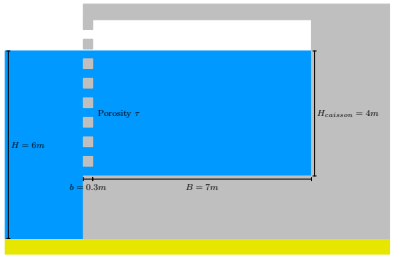


Figure 5.24: Configuration 1

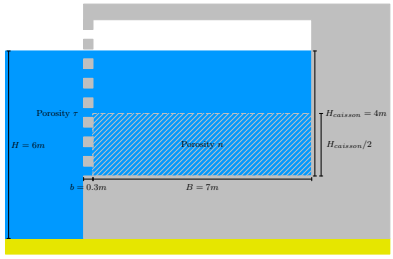


Figure 5.25: Configuration 2

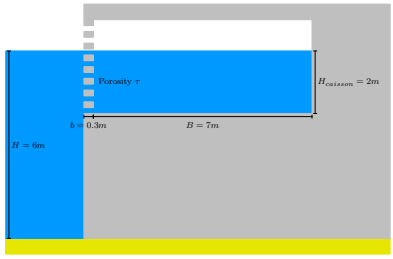


Figure 5.26: Configuration 3

Figure 5.27 displays the reflection coefficients. Results show that configuration 2 achieves a better performances than the configuration 3. However configuration 1 works better but only for small periods.

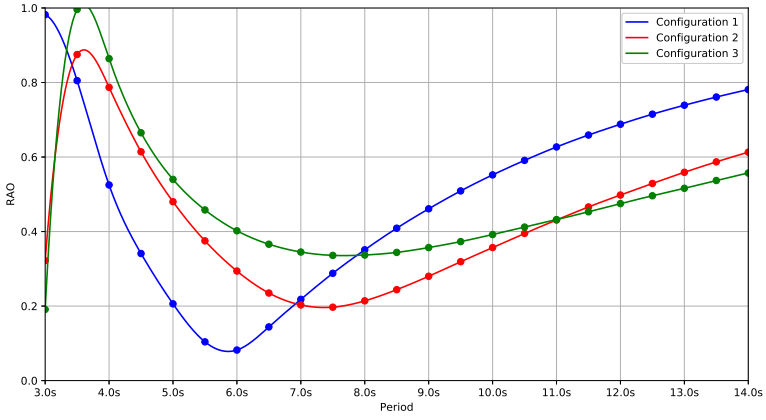


Figure 5.27: Reflection curves - Comparison of configurations 1, 2 and 3

**Porous medium at background**

The porous medium is now placed at the background of the damping chamber. The figures 5.29 and 5.30 correspond to configurations 4 and 5.

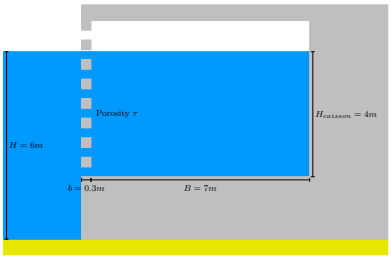


Figure 5.28: Configuration 1

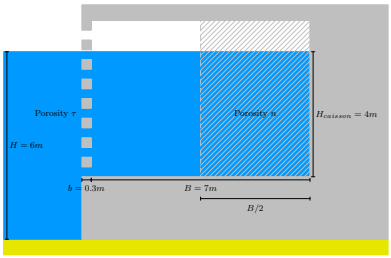


Figure 5.29: Configuration 4

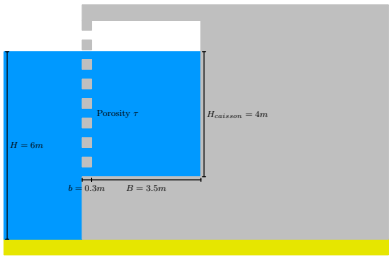


Figure 5.30: Configuration 5

A porous medium inside a damping chamber modulates the hydrodynamic behaviour. The reflection curve of configuration 4 (in red) is in-between the two classical configurations. But it seems that this configuration does not bring any advantages.

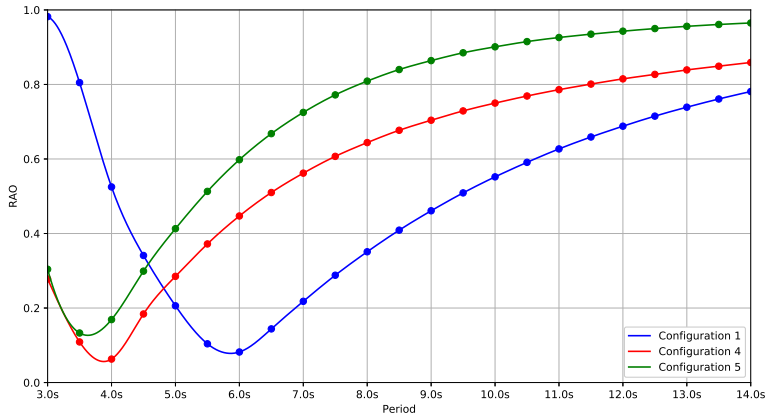


Figure 5.31: Reflection curves - Comparison of configurations 1, 4 and 5

# CONCLUSIONS AND PERSPECTIVES

**Conclusions**

Respect of the environment is a motivation to look for new kinds of breakwaters. The vertical porous breakwaters designed from a metal framework and filled with rocks greatly fit this obligation. This thesis aims to test innovative geometries of porous breakwaters through the investigation of porous media characteristics and the development of a new 3D diffraction code that implements porous media and porous walls.

This numeric tools, called *Diffra3D* and based on BEM, addresses the needs of engineering offices. It enables to obtain quick computations for testing different models of porous breakwaters, without a large computing capacity.

Its development allows us to :

- Provide a theoretical overview of modelling porous media flow.

  The porous medium is assumed homogeneous. The volumetric forces applied to the flow is expressed by the well-known extended Forchheimer equation. Three coefficients, two of resistance ($a$, $b$) and one of inertia $c$, need to be defined. They characterise the porous medium. $a$ corresponds to the linear part of the hydraulic gradient and $b$ to the quadratic part. Burcharth and Andersen (1995) [4] found the most adapted formulation to express the coefficients of Forchheimer. They depend on parameters such as porosity, size of the stones and empirical coefficients. The parameter of inertia $c$ is less studied. It depends on the porosity and on the inertia coefficient $C_M$.

- Investigate the characteristics of a porous medium through three experimental campaigns : sloshing testing on a hexapod and two classical reflection-transmission studies in a wave tank.

  Having a good dissipation rate is not enough to reproduce the correct hydrodynamic performance of a porous breakwater. We find that at low $R_e$ and $KC$ numbers, the inertial dissipation plays a major role.

  For this type of flow, a new selection of tortuosity parameters is suggested, $\alpha = 2950$ and $\beta = 0.3$. We found that the inertia coefficient $C_M$ of a porous medium has the same shape as a simple cylinder in oscillatory flow. It decreases at very small $KC$ and it reaches a constant value between 1.6 and 2.4 for higher $KC$ numbers. The evolution of $C_M$ may also depend on the nature of the flow and hence on the size of the stones and on the porosity.

  Nevertheless, no expression for $C_M$ has been found but a general trend has been drawn. More experimental data are needed to have a more precise formulation. Experimental data are missing. In the future, systematic testing on a cylinder network as a idealised porous medium could help to find an appropriate law for $C_M$.

  We also learn that the hydrodynamic performance of a porous breakwater is very sensitive to the porosity. Its estimation is a critical issue. Its must be finely controlled during the laying operator.

- Compare the code with experimental data.

  The code *Diffra3D* allows to simulate with good confidence porous media flow when the characteristics of the porous structure are well known.

  The selection of parameters $\alpha = 2950$ and $\beta = 0.3$ gives good results for low $R_e$ and $KC$ numbers. The inertia coefficient $C_M$ must then be well defined to model porous media flow when the regime is of inertial nature.

  The selection suggested by B. Jensen [25] $\alpha = 500$ and $\beta = 2$, with $C_M = 1.8$, also gives good results in cases where the flow is not of inertial nature.

Finally, innovative geometries of porous breakwaters have been tested, such as :

- Spaced gabions. They can be used to form porous plates. If built in front of a damping chamber, it results in breakwaters with hydrodynamic performance similar to Jarlan caissons. Additionally, the gabions offer an adequate environment for young fish.
- An damping chamber without a floor. The performance of a Jarlan caisson depends on the characteristics of its porous plate and on the wavelength inside compared to its dimensions. We learn that the wavelength inside the chamber does not depend on the water depth of the chamber. It only depends on the vertical size of the porous plate. A Jarlan caisson with no floor gives similar performance to a classical one.
- A mix of Jarlan caissons and porous media. The integration of a porous medium inside the damping chamber modulates the hydrodynamic behaviour. It can enable to smooth the operational window to wider frequencies.
- A simple vertical porous breakwater. These kinds of breakwaters could also be installed under pontoons inside harbours. It provides dissipation and an eco-friendly environment again.

**Perspectives**

In order to better control the different parameters of the porous medium, we suggest to perform tests with a cylinder network with various rugosities to mimic tortuosity. For this systematic study with no rugosity, a numerical study is privileged as the different characteristics of the idealised porous medium can be easily modified.

A VOF model will be used. The parametrisation of the model is the first step. The classical values of $C_M$ and $C_D$ of the literature for a simple cylinder in an oscillatory flow should be retrieved. The efforts on the cylinder are computed. From them, the inertia coefficient and drag coefficient are determined through the Equation of a Line Method (ELM) and through the Optimised Cubic Spline Method (OCSM). The kind of turbulence closure model must also be investigated.

Then, a cylinder network is of interest. This network is placed in a tank. For a oscillatory flow with no vertical velocities, the orientation of the cylinders may not have importance. They can be placed vertically or horizontally but must be perpendicular to the tank.

First, only oscillatory flows are performed. The range of $KC$ numbers to investigate are from 0 to 200. Values between 0 and 12 must be precisely defined to reproduce the observed phenomena. The dimensional parameters to vary are :

1. The diameter of the cylinders $d$ from 3cm to 8cm.
2. The porosity of the network $n$ from 35% to 50%.
3. The width of the network $b$ from 20cm to 40cm.
4. The water depth $h$ from 20cm to 60cm.

In a second part, waves could be performed to observe how orbital velocities modify the efforts. Is it still possible to easily separate inertia coefficient and drag coefficient ? In the case of orbital flow with a free surface, it is of interest to modify the orientation of the cylinders. The orientation may have an effect on the orbital velocities and on the free surface.

Nevertheless, to introduce rugosity in our model, physical tests are needed, as this kind of surface is difficult to model numerically.

# A SLOSHING

## A.1 SIZE DISTRIBUTIONS

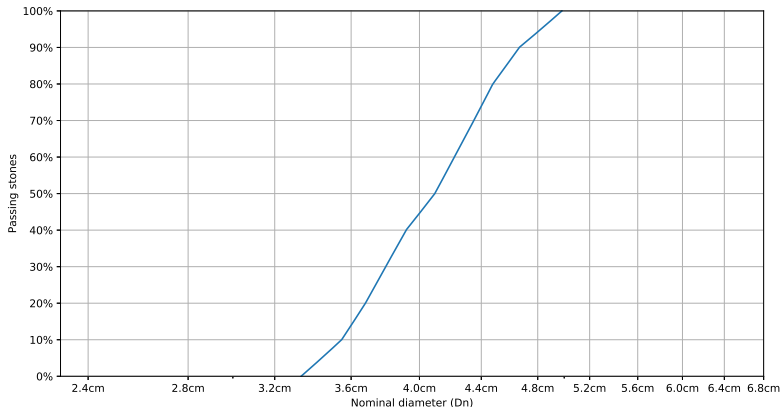


Figure A.1: Granulometry 1, Sloshing tests

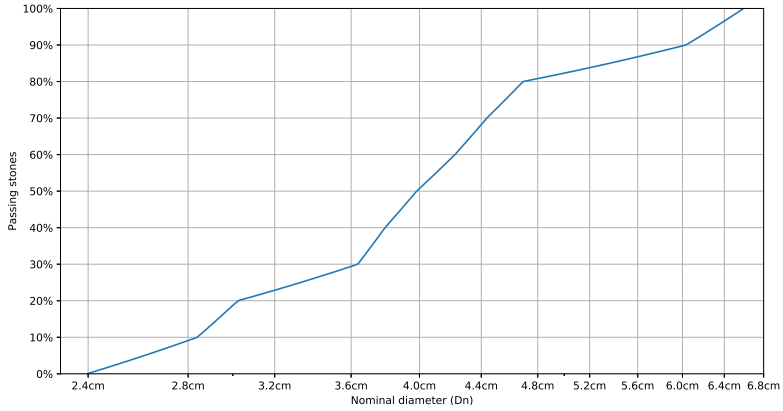


Figure A.2: Granulometry 2, Sloshing tests

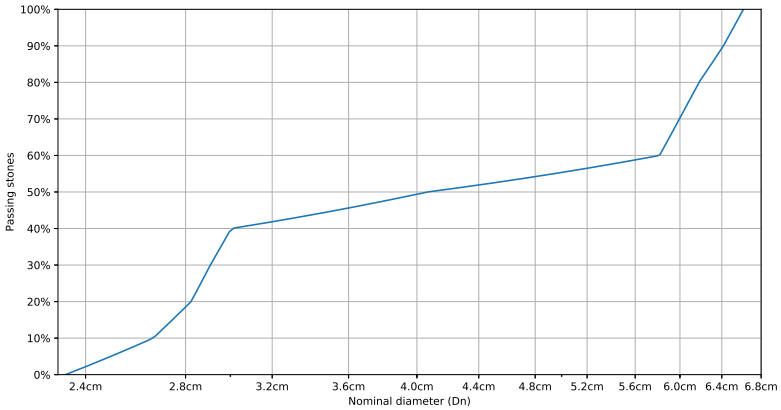


Figure A.3: Granulometry 3, Sloshing tests

# B SPACED GABIONS

## B.1 DESIGNING A DAMPING CAISSON

The aim of a damping caisson is to dissipate as much energy as possible by turbulence in its chamber as well as by induction of energy losses trough acceleration and deceleration of fluid by contraction/expansion creating water jets and the formation of vortices at the holes.

There actually are four designing parameters an engineer can play with in order to optimise the damping response of a *Jarlan* chamber :

1. The porosity $\tau$ of the porous plate.
2. The type of the holes of the porous plate, usually slit or circular openings. We saw in section 2.1.2 that the coefficient of flow restriction $k_c$ and the added inertial term in the pressure gradient equation depends on the type of hole. The size of the holes at fixed porosity, width for slits and diameter for circular openings, also play a role in the inertial term.
3. The width $b$ of the porous plate. This parameter, rarely discussed in the literature because it is generally fixed between 30 and 50cm by civil engineering, is investigated prior to presenting the experimental results of spaced gabions model.
4. The depth $H_{caisson}$ inside the chamber, which can be smaller than the depth just in front of the structure.
5. The size $B$ of the chamber.

The three first parameters play on the pressure loss that the porous plate creates bringing a phase difference between the wave outside and inside the structure.

The two last parameters previously mentioned play on the ratio $B/\lambda$ inside the chamber. The peak of operation of a damping caisson takes place when $0.10 \leq B/\lambda \leq 0.15$. The figure B.1 is a sketch of the damping caisson we start with as a reference for our sensitivity tests to design parameters. The parameter $k_c$ of flow restriction is taken to 0.8 for slits and 0.65 for circular holes.

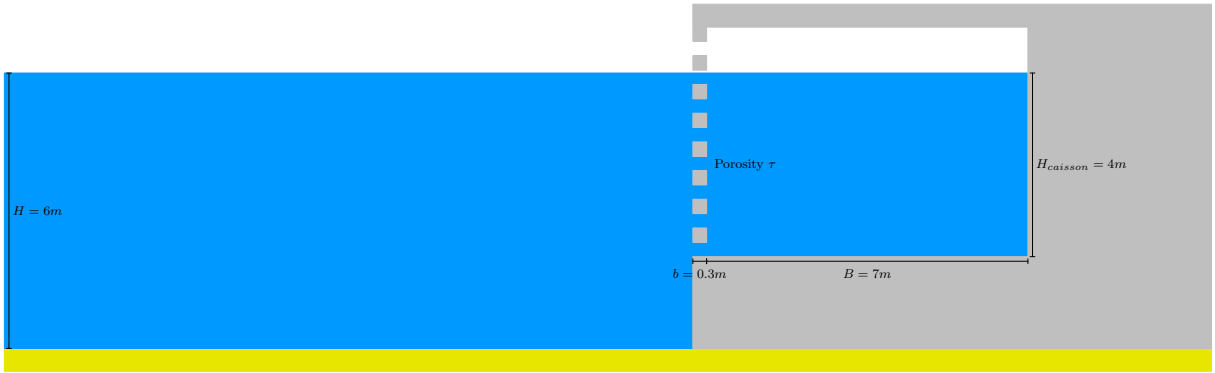


Figure B.1: Geometry of the caisson

### B.1.1 Influence of the wall porosity

In our case study, the influence of the wall porosity on the reflection coefficients is presented below on figure B.2. The holes are set to slits. There is a porosity value for which damping is better at the peak of operation. Here it's for $\tau = 40\%$ for $T = 5.5s$. However we notice that the red curve then rises faster than the green curve ($\tau = 30\%$) which finally present a better global damping over a larger range of periods.

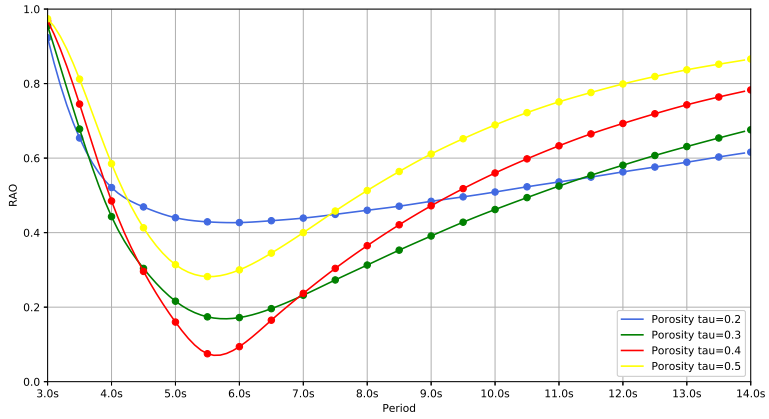


Figure B.2: Slit holes, Reflection curve

### B.1.2 Influence of hole's type

We arbitrarily set the porosity to $\tau = 40\%$ and we compare the influence of the form of the holes on reflection coefficients.

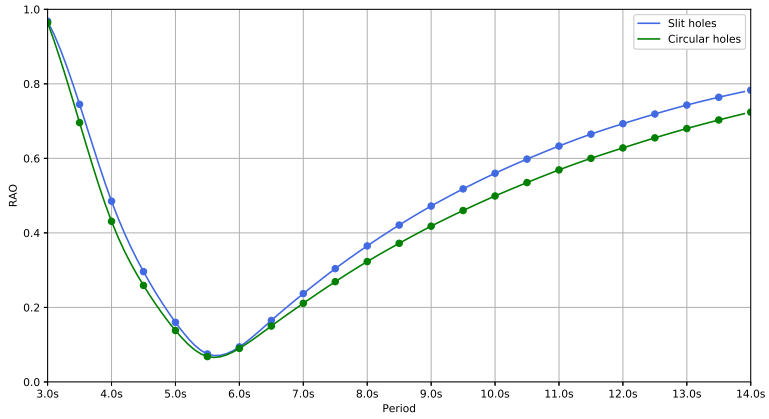


Figure B.3: Porosity $\tau = 0.4$, Reflection curve

### B.1.3 Influence of the chamber's depth

The greater the depth in the damping chamber, the longer the wavelength will be. The relation $B/\lambda$ becomes lower with the depth. That's why our curves of reflection coefficients shift towards higher periods when the depth of the chamber is reduced.

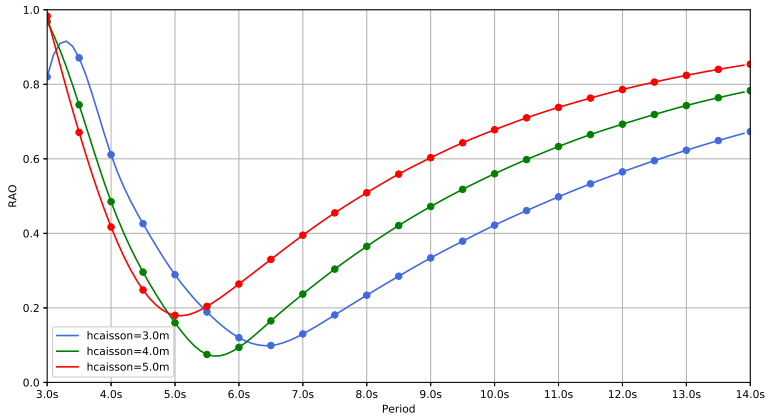


Figure B.4: Porosity $\tau = 0.4$, Slit holes, Reflection curve

### B.1.4 Influence of the chamber's size

This time we change the ratio $B/\lambda$ by varying $B$.

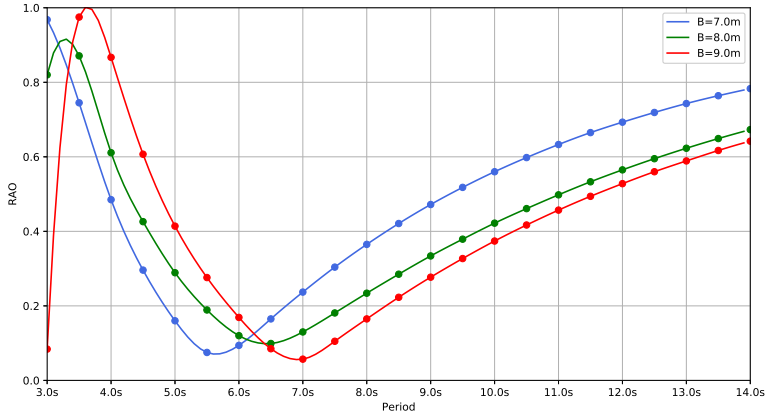


Figure B.5: Porosity $\tau = 0.4$, Slit holes, Reflection curve

## B.2 SIZE DISTRIBUTION

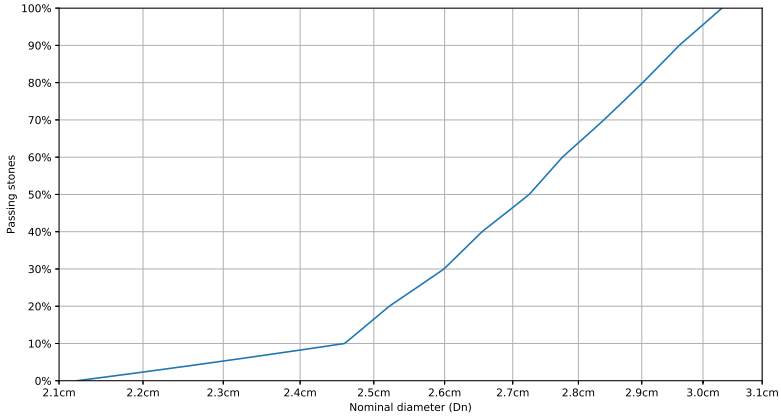


Figure B.6: Size distribution, Spaced gabions

# C VINTIMILLE

## C.1 SIZE DISTRIBUTION

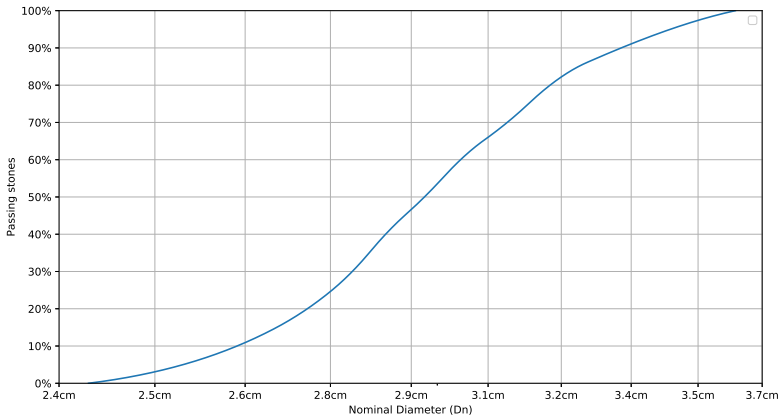


Figure C.1: Size distribution, Vintimille

# Bibliography


[1] G. Arnaud, V. Rey, J. Touboul, D. Sous, B. Molin, and F. Gouaud. Wave propagation through dense vertical cylinder arrays: Interference process and specific surface effects on damping. *Applied Ocean Research*, 65:229–237, Apr. 2017.

[2] S. Azhar, C. Dardab, J. Brossard, and M. Chagdali. Etude analytique de l'interaction houle-digue poreuse. pages 667–676. Paralia, 2008.

[3] J. Bougis. *Prise d'eau et rejet en mer*. Paralia edition, Jan. 2015.

[4] H. Burcharth and O. Andersen. On the one-dimensional steady and unsteady porous flow equations. *Coastal Engineering*, 24(3-4):233–257, Mar. 1995.

[5] H. F. Burcharth and C. Christensen. *On Stationary and Non-stationary Porous Flow in Coarse Granular Materials: European Community, MAST G6-S: Project 1, Wave Action on and in coastal structures*. Aalborg Universitetsforlag, 1991.

[6] P. C. Carman. Fluid flow through granular beds. *Transactions, Institution of Chemical Engineers, London*, (15):150–166, 1937.

[7] P. C. Carman. *Flow of gases through porous media*. London : Butterworths scientific publications, 1956.

[8] X. Chen, G. Yao, E. Herrero-Bervera, J. Cai, K. Zhou, C. Luo, P. Jiang, and J. Lu. A new model of pore structure typing based on fractal geometry. *Marine and Petroleum Geology*, 98:291–305, Dec. 2018.

[9] CIRIA, CUR, and CETMEF. *Guide Enrochement. L'utilisation des enrochements pour les ouvrages hydrauliques. Version française du Rock Manual*. CETMEF, Compiègne, 2009.

[10] F. Civan and D. Tiab. Steady and semi-steady state radial flow and partial water-drive oil and gas reservoirs using Darcy, Forchheimer, Brinkman, and capillary-orifice models. pages 381–386, Dallas, 1991.

[11] A. Costa. Permeability-porosity relationship: A reexamination of the Kozeny-Carman equation based on a fractal pore-space geometry assumption. *Geophysical Research Letters*, 33(2), 2006.

[12] R. A. Dalrymple, M. A. Losada, and P. A. Martin. Reflection and transmission from porous structures under oblique wave attack. *J. Fluid Mech*, 224:625–644, 1991.

[13] H. Darcy. *Les fontaines publiques de la ville de Dijon : Détermination des lois d'écoulement de l'eau à travers le sable*. 1856.

[14] M. Del Jesus, J. L. Lara, and I. J. Losada. Three-dimensional interaction of waves and porous coastal structures. Part I: Numerical model formulation. *Coastal Engineering*, 64:57–72, June 2012.

[15] G. Delhommeau. *Les problèmes de diffraction-radiation et de résistance des vagues*. PhD thesis, 1987.

[16] H. Den Adel. Re-analysis of permeability measurements using Forchheimers' equation. Technical Report CO-272550/56, 1987.

[17] F. Dentale. Simulation of Flow within Armour Blocks in a Breakwater. *Journal of Coastal Research*, 30(3):528, Jan. 2014.

[18] Y. Goda and T. Suzuki. Estimation of incident and reflected waves in random wave experiments. volume 15, pages 828 – 845, Honolulu, Hawai, 1976. ASCE.

[19] Z. Gu and H. Wang. Gravity waves over porous bottoms. *Coastal engineering*, 15(5-6):497–524, 1991.

[20] A. A. Hannoura and J. A. McCorquodale. Virtual Mass of Coarse Granular Media. *Journal of the Waterway Port Coastal and Ocean Division*, 104(2):191–200, 1978.

[21] S. M. Hassanizadeh and W. G. Gray. High velocity flow in porous media. *Transport in porous media*, 2(6):521–531, 1987.

[22] N. Henderson, J. C. Brêttas, and W. F. Sacco. A three-parameter Kozeny–Carman generalized equation for fractal porous media. *Chemical Engineering Science*, 65(15):4432–4442, Aug. 2010.

[23] P. Higuera, J. L. Lara, and I. J. Losada. Three-dimensional interaction of waves and porous coastal structures using OpenFOAM. Part I: Formulation and validation. *Coastal Engineering*, 83:243–258, Jan. 2014.

[24] P. Higuera, J. L. Lara, and I. J. Losada. Three-dimensional interaction of waves and porous coastal structures using OpenFOAM. Part II: Application. *Coastal Engineering*, 83:259–270, Jan. 2014.

[25] B. Jensen, B. M. Sumer, and E. D. Christensen. *Wave interaction with porous coastal structures*. PhD thesis, DTU, 2014.

[26] O. Juul Jensen and P. Klinting. Evaluation of scale effects in hydraulic models by analysis of laminar and turbulent flows. *Coastal Engineering*, 7(4):319–329, Nov. 1983.

[27] G. H. Keulegan. *Wave transmission through rock structures*. Feb. 1973.

[28] M. Koenders. Hydraulic criteria for filters. *Estuary Physics*, 1985.

[29] D. J. Korteweg and G. de Vries. On the change of form of long waves advancing in a rectangular canal, and on a new type of long stationary waves. *Philosophical Magazine*, 39(240):422–443, 1895.

[30] J. Kozeny. Ueber kapillare Leitung des Wassers im Boden. *Sitzungsber Akad. Wiss., Wien*, (136(2a)):271–306, 1927.

[31] Z. Kun-Can, W. Tong, L. Hai-Cheng, G. Zhi-Jun, and W. Wen-Fei. Fractal analysis of flow resistance in random porous media based on the staggered pore-throat model. *International Journal of Heat and Mass Transfer*, 115:225–231, Dec. 2017.

[32] D. Lajoie. *Modélisation de la houle en zone côtière : prévision de l'agitation à l'intérieur des ports et mise au point d'atténuateurs de houle dynamiques*. PhD thesis, Université d'Aix-Marseille II, Feb. 1996.

[33] D. Lajoie. Optimisation du fonctionnement des atténuateurs de houle de type dos de chameau à l'aide de perforations dans la structure. pages 749–760. Editions Paralia, 2008.

[34] D. Lajoie, J. Bougis, and J. Dolidon. Conception d'un atténuateur de houle de type caisson à double parois poreuses. 2014.

[35] F. D. E. Latief and U. Fauzi. Kozeny–Carman and empirical formula for the permeability of computer rock models. *International Journal of Rock Mechanics and Mining Sciences*, 50:117–123, Feb. 2012.

[36] C.-Y. Lin and C.-J. Huang. Decomposition of incident and reflected higher harmonic waves using four wave gauges. *Coastal Engineering*, 51(5-6):395–406, Aug. 2004.

[37] P. Lin and S. A. Karunarathna. Numerical Study of Solitary Wave Interaction with Porous Breakwaters. *Journal of Waterway, Port, Coastal, and Ocean Engineering*, 133(5):352–363, Sept. 2007.

[38] I. J. Losada, J. L. Lara, and M. del Jesus. Modeling the Interaction of Water Waves with Porous Coastal Structures. *Journal of Waterway, Port, Coastal, and Ocean Engineering*, 142(6):03116003, Nov. 2016.

[39] T. Lykke Andersen, M. R. Eldrup, and P. Frigaard. Estimation of incident and reflected components in highly nonlinear regular waves. *Coastal Engineering*, 119:51–64, Jan. 2017.

[40] O. S. Madsen and S. M. White. Reflection and transmission characteristics of porous rubble-mound breakwaters. Technical report, US Army Corps of Engineers, CERC, 1976.

[41] E. P. D. Mansard and E. R. Funke. The Measurement of Incident and Reflected Spectra Using a Least Square Method. 1980.

[42] B. Molin. *Hydrodynamique des structures offshore*. Technip edition, 2002.

[43] B. Molin and F. Remy. Etude expérimentale d'amortisseurs dynamiques de type TSD. Nov. 2014.

[44] B. Molin and F. Remy. Inertia effects in TLD sloshing with perforated screens, 2015.

[45] B. Molin, F. Remy, G. Arnaud, V. Rey, J. Touboul, and D. Sous. On the dispersion equation for linear waves traveling through or over dense arrays of vertical cylinders. *Applied Ocean Research*, 61:148–155, Dec. 2016.

[46] P. Y. POLUBARINOVA-KOCHINA. *Theory of Ground Water Movement*. PhD thesis, Princeton, 1962.

[47] S. Crowley and R. Porter. The effect of slatted screens on waves, Oct. 2011.

[48] R. Shih. Permeability characteristics of rubble material, new formulae. In *Proc. ICCE*, volume 2, pages 1499–1512, 1990.

[49] G. Smith. *Comparison of stationary and oscillatory flow through porous media*. PhD thesis, Queen's University, Kingston, Canada, 1991.

[50] C. K. Sollitt and R. H. Cross. Wave transmission through permeable breakwaters. *Coastal Engineering*, pages 1827–1846, 1973.

[51] K.-D. Suh, Y. W. Kim, and C.-H. Ji. Calculation of permeability parameter of perforated wall. *Coastal Engineering Proceedings*, 1(32), Feb. 2011.

[52] W. Sulisz. Wave reflection and transmission at permeable breakwaters of arbitrary cross-section. *Coastal Engineering*, 9(4):371–386, 1985.

[53] S. P. Tamrin, H. Parung, and A. Thaha. Experimental Study of Perforated Concrete Block Breakwater. *International Journal of Engineering & Technology IJET-IJENS*, 14(03):6–10, 2014.

[54] L. Tao, H. Song, and S. Chakrabarti. Wave interaction with a perforated circular breakwater of non-uniform porosity. *Journal of Engineering Mathematics*, 65(3):257–271, Nov. 2009.

[55] S.-W. Twu and C.-C. Liu. Interaction of non-breaking regular waves with a periodic array of artificial porous bars. *Coastal Engineering*, 51(3):223–236, May 2004.

[56] S.-W. Twu, C.-C. Liu, and C.-W. Twu. Wave damping characteristics of vertically stratified porous structures under oblique wave action. *Ocean Engineering*, 29(11):1295–1311, 2002.

[57] F. J. Valdes-Parada, J. A. Ochoa-Tapia, and J. Alvarez-Ramirez. Validity of the permeability Carman–Kozeny equation: A volume averaging approach. *Physica A: Statistical Mechanics and its Applications*, 388(6):789–798, Mar. 2009.

[58] M. R. A. Van Gent. Formulae to describe porous flow. Technical report, TUDelft, Feb. 1992.

[59] M. R. A. Van Gent. Stationary and oscillatory flow through coarse porous media. Technical report, TUDelft, June 1993.

[60] M. R. A. Van Gent. *Wave interaction with permeable coastal structures*. PhD thesis, Dec. 1995.

[61] R. Van't Veer and A. Pistidda. Forces on Bilge Keels in Regular and Irregular Oscillating Flow. June 2012.

[62] J. C. Ward. Turbulent Flow in Porous Media. *Journal of the Hydraulics Division*, 90(5):1–12, 1964.

[63] G. B. Whitham. *Linear and Nonlinear Waves*. California Institute of Technology, 1974.

[64] K. W. Wilson. *Scale Effect in Rubble-Mound Breakwater*. PhD thesis, Department of Civil Engineering, MIT, Cambridge, 1971.

[65] P. Xu and B. Yu. Developing a new form of permeability and Kozeny–Carman constant for homogeneous porous media by means of fractal geometry. *Advances in Water Resources*, 31(1):74–81, Jan. 2008.

[66] X. Yu and A. T. Chwang. Wave-induced oscillation in harbor with porous breakwaters. *Journal of waterway, port, coastal, and ocean engineering*, 120(2):125–144, 1994.

[67] Z. Zeng and R. Grigg. A Criterion for Non-Darcy Flow in Porous Media. *Transport in Porous Media*, 63(1):57–69, Apr. 2006.